

ABSTRACT

Title of dissertation: SUBMONOLAYER ADSORBATES:
THEORETICAL STUDIES OF
TRANSIENT MOBILITY
AND SYMMETRY-BREAKING

Josue Ricardo Morales Cifuentes
Doctor of Philosophy, 2019

Dissertation directed by: Professor Theodore L. Einstein
Department of Physics

Weakly bound submonolayer adsorbates provide important insight into fundamental descriptions of physics that would otherwise be masked, or even suppressed, by strong effects such as chemical binding. We focus on two surface effects: transient mobility at the microscopic scale, and symmetry-breaking at the atomic one.

We present a novel island nucleation and growth model that explicitly includes, at the microscopic scale, the behavior of transient (ballistic) monomers. At a deposition rate F , monomers are assumed to be in a hot precursor state before thermalizing. In the limiting regimes of fast (diffusive) and slow (ballistic) thermalization, we recover the expected scaling of the island density, N : $N \propto F^\alpha$. We construct effective growth exponents, α_{eff} , and activation energies to properly characterize the transitional regions between these limiting regimes. Through these constructs, we describe a rich and complex structure of metastable limiting regimes, asymptotic behavior and energetically driven transitions. Application to $N(F, T)$ of

recent organic-molecule deposition experiments yields excellent fits.

We have also studied, at the atomic scale, an effective potential mechanism that breaks the intrinsic two-fold sublattice (hexagonal) symmetry of (honeycomb) graphene using DFT calculations (VASP ver 5.3.3). We choose the specific system of CF_3Cl adsorbates on single layer graphene, to benefit from experimental results obtained locally. Using ab initio van der Waals density functionals, we discover a physisorbed phase with binding energies of about 280 meV. For low coverages, sublattice symmetry-breaking effects are responsible for gap openings of 4 meV; contrastingly, in large coverages, it is the formation of ordered overlayers that opens gaps nearly 5 times as large, of roughly 18 meV. We discover that in both cases, differentiation of graphene's two sublattices induces symmetry-breaking by means of adsorbate interactions that favor large ordered regions, coverage itself is insignificant. For CF_3Cl adsorbates on bilayer graphene, symmetry-breaking effects caused by the formation of graphene-like overlayers, and not sublattice differentiation, opened gaps of 25 meV, the largest in our study.

SUBMONOLAYER ADSORBATES: THEORETICAL STUDIES
OF TRANSIENT MOBILITY AND SYMMETRY BREAKING

by

Josue Ricardo Morales Cifuentes

Dissertation submitted to the Faculty of the Graduate School of the
University of Maryland, College Park in partial fulfillment
of the requirements for the degree of
Doctor of Philosophy
2019

Advisory Committee:

Professor Theodore L. Einstein, Chair/Advisor

Professor Janice E. Reutt-Robey, Dean's Representative

Professor John D. Weeks

Professor Ellen D. Williams

Professor Alberto Pimpinelli

© Copyright by
Josue Ricardo Morales Cifuentes
2019

Dedication

To my family

Acknowledgments

Scientific work is often summarized in terms of landmark results. Often overlooked are the cumulative efforts, the negative results, and the unpublished conversations that lead to the great insights. In a sense, the human experience behind scientific work is often one of these overlooked elements. Its absence is not malicious, as science exists (and should exist) beyond the individual, but is felt nonetheless. Thus, these acknowledgements are an attempt to give human context to this dissertation: for the road that started with my first day at *University of Maryland* to the publication of this manuscript was paved with many good things, but it was challenging nonetheless.

I am very grateful to my friend (and former roommate) Matthew Reed. The scent of browning onions, cured meats, and *hoppy* beer will always remind me of him. A common sight at the apartment was Matt recounting one of his many anecdotes about his beloved California, his latest gastronomic discovery, or his novel political theories that aimed to unravel some great mystery about the American experience, while Rufus, his loyal Vizsla, futilely tried to steal some food. I am most grateful for what those moments meant to me: as I struggled through so much during my

graduate career, they brought me comfort and happiness.

Those first years in graduate school, I looked forward to my Friday nights at *Plato's* the most. Our little group: Freja Nordsiek, Anne Handschy, Aaron Hagerstrom, Joel Dahlin, and myself, always had some subject to tackle and something to say. If asked, I could not cite a single conversation we had during all those years, but in the comfort of that leather booth, surrounded by the scent of drip coffee, and *Tzatziki* sauce, their company was enough to help me through the week. After having lived in Alabama for so many years, my friends were the first to make me feel like I belonged at Maryland.

It is difficult to find a proper way to thank my advisor Ted Einstein. All these years, all those meetings at his office, all those small conversations change a person: the cumulative effect of his mentoring will remain a critical part of my education as a scientist. However, it is the quality of his being that I am most grateful to have experienced. It is true that I am a better physicist having been mentored by Dr. Einstein, but I am certainly a better person for having met Ted.

After being away from my native Guatemala for such a long time, home became a transient concept. It was not until I met Amanda, my fiancée, that I felt any place could be home. Her fondness for the American countryside made me feel I was at the right place. Amanda's love, affection, support, humor, and kindness were such an important part of my graduate career, that I struggle to think of an aspect of my life that was not improved by her presence. She was next to me during my low points, and I am glad we now get to take our brightest steps together. Along with her family (Elizabeth, Gary, and so many more), I found myself surrounded with love.

I cannot overlook the emotional support provided by our little Dachshund pack: Bodie, Lenny and Kale often functioned as my sounding board (I talked to them) and peer review (I talked to myself); however, this is included for completeness as I doubt they will read this work.

A piece of my heart remains with my family back in Guatemala. I have been away from the company of my parents, my brother, and our Schnauzers for over a decade. I thank you for your confidence in me, your support and your love. My wish is that I have made you guys proud.

I thank the members of my advisory committee, Janice E. Reutt-Robey, John D. Weeks, Ellen D. Williams, and Alberto Pimpinelli, for their comments and insight in the completion of this manuscript. In particular, Janice's (and her former post-doc Yilin Wang) physical insight was one of the inspirations for our CF_3Cl adsorption work, and our close collaboration with Alberto led to our fruitful rate-equations model.

Finally, I should acknowledge the many organizations that provided their assistance and support. A big thanks to the Physics Department at University of Maryland for their financial and logistical assistance during my graduate career, and to the Mathematics Department for providing me with a teaching assistantship during my last year of graduate school. Thanks to the Texas Advanced Computing Center (TACC) at The University of Texas at Austin for providing crucial grid resources for the completion of this work. This project was supported in part by NSF Grants DMR 05-20471 and CHE 13-05892.

Table of Contents

Dedication	ii
Acknowledgments	iii
Table of Contents	vi
List of Tables	viii
List of Figures	x
List of Abbreviations	xvii
Chapters	1
1 Introduction	2
1.1 Submonolayer Adsorbates	2
1.2 Diffusion-Limited Aggregation (DLA) and Transient Effects	4
1.3 Graphene's Band Structure and Future Electronics	5
2 Microscopic Scale: Transient Mobility Effects	7
2.1 Introduction	7
2.2 Theoretical Development	10
2.3 Analytic Solution	16
2.4 Growth Exponents	20
2.5 Approximations to Analytic Solution	30
2.6 Activation Energy	37
2.7 Experimental Fit	49
2.8 Summary and Conclusion	62
3 Atomic Scale: Symmetry-Breaking	64
3.1 Introduction	64
3.2 Tight-Binding Considerations	71
3.3 Supercell Construction	74
3.4 DFT Considerations	82
3.5 Symmetry-Breaking Effects	85
3.6 Summary and Conclusion	115

4	Conclusion and Future Work	118
4.1	Transient Mobility Effects	118
4.2	CF ₃ Cl Overlayers and Symmetry-Breaking	120
	Appendices	122
A	Code for Hot-Monomer Analysis	123
A.1	Header Code	123
A.2	Fit Analysis	130
B	VASP Code	132
B.1	INCAR (Calculation Parameters)	132
B.2	POSCAR (Atom Locations)	134
B.3	KPOINTS (Grid Points)	135
	Bibliography	136

List of Tables

2.1	The 16 regimes for extremal values of z , \mathcal{R}_n , \mathcal{R}_B and \mathcal{R}_C , along with the associated rescaled effective exponents (cf. Figs. 2.2-2.3) and effective activation energies. D (H) indicates DLA (HMA): $z \ll (\gg)1$. The subscripts give the limiting value of the \mathcal{R} 's, with 1 denoting $\mathcal{R} = \infty$, i.e. $\text{index} = \exp(-1/\mathcal{R})$. For α_{eff} , \mathcal{R}_C is inconsequential, so that only the first 2 subscripts are needed, yielding just 8 regimes. Note that the reduced values of E_A^{eff} in the last column must be multiplied by the corresponding α_{eff}/i to get the actual E_A^{eff}	40
2.2	The 8 possible individual energy contributions to the activation energy E_A^{eff} for extremal values of z , \mathcal{R}_n , \mathcal{R}_B and \mathcal{R}_C . D (H) indicates DLA (HMA): $z \ll (\gg)1$. The subscripts give the limiting value of the \mathcal{R} 's, with 1 denoting $\mathcal{R} = \infty$, i.e. $\text{index} = \exp(-1/\mathcal{R})$. An asterisk (*) indicates an arbitrary value. Note that the reduced values of E_A^{eff} in the last column must be multiplied by the corresponding α_{eff}/i to get the actual E_A^{eff}	48
2.3	The converged fits for different values of i . The results for $i = 4$ are in bold, as they are the best fitting results that describe hot-monomers being superthermal.	51
2.4	The dynamic indexes for each of the four experimental runs, for $i = 4$ at fixed β . D (H) indicates DLA (HMA): $z \ll (\gg)1$; and the numbers represent the dynamic indexes for \mathcal{R}_n , \mathcal{R}_B and \mathcal{R}_C , respectively. . . .	56
3.1	The transformations required to convert an orientation in the first column into an orientation in the first row for CF_3Cl molecules in the <i>C phase</i> . For the transformations, positive numbers, e.g. 30° , refer to a clockwise rotation by an amount in degrees (and a negative number to a counter-clockwise rotation); while, ordered pairs, e.g. $(1, 0)$, refer to translations by the lattice vectors \vec{a}_1 , and \vec{a}_2 (as defined in Eqn. 3.1). If two transformations are present, then the left-to-right order indicates the order of application.	81

3.2	Gaps and energies (in meV) in the band structure of SLG graphene for <i>low coverage</i> (2×2) in the <i>C phase</i> . E_{gap} is the gap in the band structure at the Dirac point, V_{eff} is the magnitude of the effective potential inducing symmetry-breaking and V_{shear} the shearing potential due to stress on the graphene substrate. E_{pristine} represents the gap in <i>pristine</i> (frozen and without the CF_3Cl adsorbate) graphene due to deformations. $V_{\text{pp}\pi}$ represents the <i>effective nearest neighbor</i> interactions for the <i>folded</i> (2×2) supercell.	97
3.3	Gaps and energies (in meV) in the band structure of SLG graphene for <i>high coverage</i> ($\sqrt{3}\times\sqrt{3}$) in the <i>C phase</i> . E_{gap} is the gap in the band structure at the Dirac point, V_{eff} is the magnitude of the effective potential inducing symmetry-breaking and V_{shear} the shearing potential due to stress on the graphene substrate. E_{pristine} represents the gap in <i>pristine</i> (frozen and without the CF_3Cl adsorbate) graphene due to deformations. $V_{\text{pp}\pi}$ represents the <i>effective nearest neighbor</i> interactions for the <i>folded</i> ($\sqrt{3}\times\sqrt{3}$) supercell.	105
3.4	Gaps (in meV) in the band structure of BLG for <i>low coverage</i> (2×2) in the <i>C phase</i> . E_{gap} is the gap in the band structure at the Dirac point, and E_{pristine} represents the gap in <i>pristine</i> (frozen and without the CF_3Cl adsorbate) BLG due to deformations. The subscript in the orientations denotes the sublattice in the bottom SLG stack shared with the top SLG stack, as the CF_3Cl molecule is localized about S_3 in both cases.	114

List of Figures

2.1	An idealized illustration of the adsorption mechanisms in the hot-monomer model. Thermalized monomers (red) are deposited on a substrate (yellow) at a flux-deposition rate F ; and they can be immediately adsorbed into a cluster (purple cluster) with lifetime $\tau_{h \rightarrow N}$. Hot-monomers have a lifetime τ_h before they become classical thermalized monomers (red), which can in turn become adsorbed into a cluster with lifetime $\tau_{th \rightarrow N}$. The interplay between these lifetimes is a key component of the various limiting regimes of the model.	11
2.2	The effective exponent α_{eff} vs. $\hat{N}(F)$ for $i = 4$ with focus on the fast thermalization regime. The crossover region between the limiting DLA (D00) and HMA (H11) scaling is explored by varying R_n and R_B	25
2.3	The effective exponent α_{eff} vs. $\hat{N}(F)$ for $i = 4$ with focus on the slow thermalization regime. The crossover region between the limiting DLA (D00) and HMA (H11) scaling is explored by varying R_n and R_B	26
2.4	The effective exponent α_{eff} explored in the parameter space $(\mathcal{R}_n \times \mathcal{R}_B)$ in the fast thermalization regime $z = 10^{-6}$, $i = 4$. Note that as \mathcal{R}_n and \mathcal{R}_B tend to the limiting regimes ($\ll 1$ and $\gg 1$), the effective exponent matches the plateau values: $\alpha_{\text{D00}} = 2/3$, $\alpha_{\text{D01}} = 2$, $\alpha_{\text{D10}} = 4/5$, and $\alpha_{\text{D11}} = 4$	27
2.5	The effective exponent α_{eff} explored in the parameter space $(\mathcal{R}_n \times \mathcal{R}_B)$ in the slow thermalization regime $z = 10^{+6}$, $i = 4$. Note that as \mathcal{R}_n and \mathcal{R}_B tend to the limiting regimes ($\ll 1$ and $\gg 1$), the effective exponent matches the plateau values: $\alpha_{\text{H00}} = 8/17$, $\alpha_{\text{H01}} = 8/9$, $\alpha_{\text{H10}} = 8/15$, and $\alpha_{\text{H11}} = 8/7$	28
2.6	The percentage difference, $ \alpha_{\text{eff}} - \alpha_{\text{eff}}^{\text{asy}} /\alpha_{\text{eff}}$, between the growth exponent α_{eff} , and its asymptotic approximation $\alpha_{\text{eff}}^{\text{asy}}$ explored in the parameter space $(\mathcal{R}_n \times \mathcal{R}_B)$ for the fast thermalization regime (established by fixing $z = 10^{-6}$) and $i = 4$. Note the presence of a large error about $\mathcal{R}_B \sim 1$. General monotonic features are observed, as values in the parameter space are fixed to the D** regime ($z \ll 1$).	34

2.7	The percentage difference, $ \alpha_{\text{eff}} - \alpha_{\text{eff}}^{\text{asy}} /\alpha_{\text{eff}}$, between the growth exponent α_{eff} , and its asymptotic approximation $\alpha_{\text{eff}}^{\text{asy}}$ explored in the parameter space $(\mathcal{R}_n \times \mathcal{R}_B)$ for the slow thermalization regime (established by fixing $z = 10^{+6}$) and $i = 4$. Note the presence of a slight error about $\mathcal{R}_B \sim 1$. General monotonic features are observed, as values in the parameter space are fixed to the H** regime ($z \gg 1$).	35
2.8	The percentage difference, $ \alpha_{\text{eff}} - \alpha_{\text{eff}}^{\text{asy}} /\alpha_{\text{eff}}$, between the growth exponent α_{eff} , and its asymptotic approximation $\alpha_{\text{eff}}^{\text{asy}}$ explored in the parameter space $(\mathcal{R}_n \times \mathcal{R}_B)$ for the transitional thermalization regime (established by fixing $z = 10^0$) and $i = 4$. Note the increasing error with increasing \mathcal{R}_B and at $\mathcal{R}_B \sim 1$. Non-monotonic features are observed, particularly for $\mathcal{R}_B \sim 1$ and $\mathcal{R}_n \sim 1$, as values in this region of parameter space are transitional (not in a limiting regime).	36
2.9	E_A^{eff} vs. β for $i = 4$ and some values of R_n^0 and R_B^0 , R_x^0 meaning $R_x(\beta = 0)$. The fast (slow) thermalization regimes are left (right) of the crossover value $z = 1$ (note F and θ are chosen to satisfy $z(\beta_c = 20) = 1$). Energies are chosen so that $\mathcal{R}_C \ll 1$.	41
2.10	E_A^{eff} vs. β for $i = 4$ and some values of R_n^0 and R_B^0 , R_x^0 meaning $R_x(\beta = 0)$. The fast (slow) thermalization regimes are left (right) of the crossover value $z = 1$ (note F and θ are chosen to satisfy $z(\beta_c = 5) = 1$). Energies are chosen so that $\mathcal{R}_C \gg 1$.	42
2.11	E_A^{eff} vs. β for $i = 4$ and some values of R_n^0 and R_B^0 , R_x^0 meaning $R_x(\beta = 0)$. The fast (slow) thermalization regimes are left (right) of the crossover value $z = 1$ (note F and θ are chosen to satisfy $z(\beta_c = 5) = 1$). Energies are chosen so that $\mathcal{R}_C \ll 1$.	43
2.12	E_A^{eff} vs. β for $i = 4$ and some values of R_n^0 and R_B^0 , R_x^0 meaning $R_x(\beta = 0)$. The fast (slow) thermalization regimes are left (right) of the crossover value $z = 1$ (note F and θ are chosen to satisfy $z(\beta_c = 10) = 1$). Energies are chosen so that $\mathcal{R}_C \gg 1$.	44
2.13	The percentage difference, $ \alpha_{\text{eff}} - \alpha_{\text{eff}}^{\text{asy}} /\alpha_{\text{eff}}$, between the growth exponent α_{eff} , and its asymptotic approximation $\alpha_{\text{eff}}^{\text{asy}}$ in the parameter space for the experiment [57]. Note the experimental data lies on the $\mathcal{R}_n \sim \mathcal{R}_B$ diagonal, as anticipated by $\mathcal{R}_n = \frac{D}{\ell v} \mathcal{R}_B$ (see 2.23).	52
2.14	The effective exponent α_{eff} explored in the parameter space $(\mathcal{R}_n \times \mathcal{R}_B)$ in the fast thermalization regime $z = 10^{-6}$, $i = 4$ for the experiment [57]. Note the gradual change of the growth exponent throughout the sampled parameter space.	53
2.15	<i>Dynamic-index</i> , J_x as given in 2.42, values for \hat{z} (blue), \mathcal{R}_B (green), \mathcal{R}_C (red-concealed by horizontal axis), and \mathcal{R}_n (yellow-concealed by horizontal axis) vs. $\log_{10} F$ for $\beta = 77.36 \text{ ev}^{-1}$ and F in the sampled experimental range. As constructed, the index is constrained to the $[0, 1]$ interval. The dynamic index for \mathcal{R}_B is notable, as it is the only one transitioning for this temperature run from 0.4 at low F to 0.9 at high F . Since $\mathcal{R}_n, \mathcal{R}_C \ll 1$, they appear close to the horizontal axis.	57

2.16	<p><i>Dynamic-index, J_x as given in 2.42, values for \hat{z} (blue), \mathcal{R}_B (green), \mathcal{R}_C (red-concealed by horizontal axis), and \mathcal{R}_n (yellow-concealed by horizontal axis) against $\log_{10} F$ for $\beta = 58.02 \text{ eV}^{-1}$ and F in the sampled experimental range. As constructed, the index is constrained to the $[0, 1]$ interval. The dynamic index for \mathcal{R}_B is notable, as it is the only one transitioning for this temperature run from 0.3 at low F to 0.9 at high F. Since $\mathcal{R}_n, \mathcal{R}_C \ll 1$, they appear close to the horizontal axis.</i></p>	58
2.17	<p><i>Dynamic-index, J_x as given in 2.42, values for \hat{z} (blue), \mathcal{R}_B (green), \mathcal{R}_C (red), and \mathcal{R}_n (yellow-concealed by horizontal axis) against $\log_{10} F$ for $\beta = 38.68 \text{ eV}^{-1}$ and F in the sampled experimental range. As constructed, the index is constrained to the $[0, 1]$ interval. The dynamic indexes for \mathcal{R}_B and \mathcal{R}_C are notable: \mathcal{R}_B for being the only one transitioning for this temperature run (from 0.2 at low F to 1.0 at high F), and \mathcal{R}_C for being transitional (index is 0.3, and no evolution occurs as fixed β implies a fixed \mathcal{R}_C). Since $\mathcal{R}_n \ll 1$, it appears close to the horizontal axis.</i></p>	59
2.18	<p><i>Dynamic-index, J_x as given in 2.42, values for \hat{z} (blue), \mathcal{R}_B (green), \mathcal{R}_C (red), and \mathcal{R}_n (yellow-concealed by horizontal axis) against $\log_{10} F$ for $\beta = 29.01 \text{ eV}^{-1}$ and F in the sampled experimental range. As constructed, the index is constrained to the $[0, 1]$ interval. The dynamic indexes for \mathcal{R}_B and \mathcal{R}_C are notable: \mathcal{R}_B for being the only one transitioning for this temperature run (from 0.1 at low F to 1.0 at high F), and \mathcal{R}_C for completely transitioning into the state D^{**1}. Since $\mathcal{R}_n \ll 1$, it appears close to the horizontal axis.</i></p>	60
2.19	<p><i>Island density vs. deposition rate F in the aggregation regime for 6P on sputter-modified mica (001) [57] at $T = 150\text{K}$ (black, square dots), 200K (red, round dots), 300K (blue, star dots), and 400K (green, triangular dots), with best-fit parameters: $i = 4$, $\log_{10} \mathcal{R}_n^0 = -5.57$, $\log_{10} \mathcal{R}_B^0 = 5.08$, $\log_{10} v\tau_0 [\mu\text{m}] = 2.54$, and, in eV, $E_D = 0.0170$, $E_{ph} = 0.0171$, and $E_b = 0.333$. The final effective coverage θ_{eff} is given by $\log_{10} (\theta_{\text{eff}} \tau_0^i [\mu\text{m}^{-2} \text{s}^i]) = -25.4$.</i></p>	61

3.1	<p>Top) The electronic structure of graphene: note that the conduction band (BC as in <i>bande de conduction</i>) and the valence band (BV as in <i>bande de valence</i>) are separated at the K (Dirac point) and K' points in reciprocal space. The local structure at the Dirac point, i.e. the Dirac cone, is responsible for the semimetal nature of graphene as a single point separates the hole band (<i>vide d'électrons</i>) from the electron band (<i>pleine d'électrons</i>) [59]. Bottom) Schematic of single layer graphene (SLG) as a subset of a triangular lattice. Sublattices S_1 (red sites) and S_2 (blue sites) represent the two carbon atoms that constitute the smallest supercell of infinitely periodic graphene, while sublattice S_3 (black dot) marks the hollow sites (honeycomb) in graphene. Note that there are no C atoms in S_3, but the marker is included to stress the unoccupied site in the triangular lattice, useful when considering symmetry-breaking effects.</p>	65
3.2	<p>Top) Differentiation of graphene substrate's sublattices by application of a hexagonal boron nitride adsorbate (hBN). In this case, the C–N bond with one sublattice, and C–B bond with the other one create the required effective potential [60]. Bottom) Calculated band structure from DFT calculations on the graphene-hBN system. Note the gap at the K point of 53.0 meV [60].</p>	67
3.3	<p>Top) Supercell for TMA overlayers in SLG; note the graphene supercell is (7×7) with 2 TMA molecules per cell [62]. Bottom) Calculated band structure of SLG with TMA adsorbate. Note the gap at the K point of 15.3 meV [62].</p>	70
3.4	<p>Left) <i>Ball-and-stick</i> model for a single CF_3Cl molecule. The C atom (yellow) connects the tetrahedral base made up of 3 F atoms (purple) to a cusp consisting of 1 Cl atom (green). Molecule dimensions are representative and calculated using optB86b-vdW. Right) Experimental phases of CF_3Cl on BLG [63]: Right, Top) ordered <i>E Phase</i> with CF_3Cl non-perpendicular to graphene surface, Right, Middle) disordered <i>IC Phase</i> with CF_3Cl non-perpendicular to graphene surface, and Right, Bottom) ordered <i>C Phase</i> with CF_3Cl perpendicular to graphene surface.</p>	76
3.5	<p>Sample supercells of coverage (2×2), with orientation HS (C atom in hollow, with staggered F atoms). Shown are $3 \times 3 = 9$ instances of a (2×2) supercell, where a (2×2) supercell contains 1 CF_3Cl molecule.</p>	78
3.6	<p>Sample supercells of coverage $(\sqrt{3} \times \sqrt{3})$, with orientation HS (C atom in hollow, with staggered F atoms). Shown are $2 \times 2 = 4$ instances of a $(\sqrt{3} \times \sqrt{3})$ supercell, where a $(\sqrt{3} \times \sqrt{3})$ supercell contains 3 CF_3Cl molecules.</p>	79

3.7	All four possible orientations of CF_3Cl molecules in the C phase. The graphene sublattices S_1 and S_2 are stylized as line bonds (red and blue). In H^* orientations the CF_3Cl molecule sits on a honeycomb hollow, while in C^* orientations it sits on an occupied graphene sublattice. For the F atoms, the eclipsed orientations ($^*\text{E}$) refer to F atoms eclipsing an occupied sublattice, while the staggered orientations ($^*\text{S}$) do otherwise.	80
3.8	Adsorption energy for CF_3Cl adsorbates on graphene in units of energy per CF_3Cl molecule, as computed via DFT calculations using the optB86b-vdW1 implementation of van der Waals interactions. For every possible orientation, adsorption energy is plotted against coverage: notably, though adsorption energy changes depending on orientation, it remains insensitive to coverage.	87
3.9	Adsorption energy for CF_3Cl adsorbates on graphene in units of energy per CF_3Cl molecule, as computed via DFT calculations using the optB88-vdW1 implementation of van der Waals interactions. For every possible orientation, adsorption energy is plotted against coverage: notably, though adsorption energy changes depending on orientation, it remains insensitive to coverage.	88
3.10	Adsorption energy for CF_3Cl adsorbates on graphene in units of energy per CF_3Cl molecule, as computed via DFT calculations using the optPBE-vdW1 implementation of van der Waals interactions. For every possible orientation, adsorption energy is plotted against coverage: notably, though adsorption energy changes depending on orientation, it remains insensitive to coverage.	89
3.11	Adsorption energy for CF_3Cl adsorbates on graphene in units of energy per CF_3Cl molecule, as computed via DFT calculations using the rPW86-vdW2 implementation of van der Waals interactions. For every possible orientation, adsorption energy is plotted against coverage: notably, though adsorption energy changes depending on orientation, it remains insensitive to coverage.	90
3.12	Adsorption energy for CF_3Cl adsorbates on graphene in units of energy per CF_3Cl molecule vs. coverage, as computed via DFT calculations for the HE orientation. Note that the hierarchy in the estimation of adsorption energy for every potential is not unique to the HE orientation.	91
3.13	Adsorption energy for CF_3Cl adsorbates on graphene in units of energy per CF_3Cl molecule vs. coverage, as computed via DFT calculations for the HS orientation. Note that the hierarchy in the estimation of adsorption energy for every potential is not unique to the HS orientation.	92

3.14	Adsorption energy for CF_3Cl adsorbates on graphene in units of energy per CF_3Cl molecule vs. coverage, as computed via DFT calculations for the CE orientation. Note that the hierarchy in the estimation of adsorption energy for every potential is not unique to the CE orientation.	93
3.15	Adsorption energy for CF_3Cl adsorbates on graphene in units of energy per CF_3Cl molecule vs. coverage, as computed via DFT calculations for the CS orientation. Note that the hierarchy in the estimation of adsorption energy for every potential is not unique to the CS orientation.	94
3.16	Gaps (meV) in the band structure of SLG graphene for <i>low coverage</i> (2×2) at the <i>C phase</i> . Note that due to folding, the K point in (1×1) is mapped to K' in (2×2) . Gaps (when present) open the valence band (blue) from the conduction band (red) below the Fermi level (n-type). The band structure about K' is presented for all orientations: Top, Left) HS, Top, Right) HE, Bottom, Left) CS, and Bottom, Right) CE.	98
3.17	LDOS for HS orientation with LDOS localization about the CF_3Cl overlayer in the <i>C-phase</i> at low coverage (2×2) . Graphene sublattices are colored brown and cyan, respectively. Note the complete lack of symmetry-breaking effects in this orientation, as all sublattices are affected by the CF_3Cl molecules equally (emphasis in red).	99
3.18	LDOS for HE orientation with LDOS localization about the CF_3Cl overlayer in the <i>C-phase</i> at low coverage (2×2) . Graphene sublattices are colored brown and cyan, respectively. Note symmetry-breaking effects in this orientation, as one sublattice is largely unaffected by the CF_3Cl molecules (emphasis in red).	100
3.19	LDOS for CS orientation with LDOS localization about the CF_3Cl overlayer in the <i>C-phase</i> at low coverage (2×2) . Graphene sublattices are colored brown and cyan, respectively. Note weaker symmetry-breaking effects in this orientation, as one sublattice is <i>slightly</i> less affected by the CF_3Cl molecules (emphasis in red).	101
3.20	LDOS for CE orientation with LDOS localization about the CF_3Cl overlayer in the <i>C-phase</i> at low coverage (2×2) . Graphene sublattices are colored brown and cyan, respectively. Note symmetry-breaking effects in this orientation, as one sublattice is largely unaffected by the CF_3Cl molecules (emphasis in red).	102
3.21	Gaps (meV) in the band structure of SLG graphene for <i>high coverage</i> ($\sqrt{3}\times\sqrt{3}$) at the <i>C phase</i> . Note that due to folding, the K point in (1×1) is mapped to Γ in ($\sqrt{3}\times\sqrt{3}$) . Gaps (when present) open the valence band (blue) from the conduction band (red) above the Fermi level (p-type). The band structure about Γ is presented for all orientations: Top, Left) HS, Top, Right) HE, Bottom, Left) CS, and Bottom, Right) CE.	106

3.22	LDOS for HS orientation with LDOS localization about the CF ₃ Cl overlayer in the <i>C-phase</i> at high coverage ($\sqrt{3} \times \sqrt{3}$). Graphene sublattices are colored brown and cyan, respectively. Note symmetry-breaking effects in this orientation are due to the formation of a graphene-like <i>meta overlayer</i> (lattice constant $\sqrt{3}a$), with differentiated <i>meta sublattices</i> (emphasis in red).	107
3.23	LDOS for HE orientation with LDOS localization about the CF ₃ Cl overlayer in the <i>C-phase</i> at high coverage ($\sqrt{3} \times \sqrt{3}$). Graphene sublattices are colored brown and cyan, respectively. Note symmetry-breaking effects in this orientation are due to the formation of a graphene-like <i>meta overlayer</i> (lattice constant $\sqrt{3}a$), with mismatching lattice constant with respect to the underlying graphene substrate (emphasis in red).	108
3.24	LDOS for CS orientation with LDOS localization about the CF ₃ Cl overlayer in the <i>C-phase</i> at high coverage ($\sqrt{3} \times \sqrt{3}$). Graphene sublattices are colored brown and cyan, respectively. Note symmetry-breaking effects in this orientation are due to weak sublattice differentiation, as the formation of a triangular <i>meta overlayer</i> does not conflict with the underlying graphene substrate (emphasis in red).	109
3.25	LDOS for CE orientation with LDOS localization about the CF ₃ Cl overlayer in the <i>C-phase</i> at high coverage ($\sqrt{3} \times \sqrt{3}$). Graphene sublattices are colored brown and cyan, respectively. Note symmetry-breaking effects in this orientation are due to weak sublattice differentiation, as the formation of a triangular <i>meta overlayer</i> does not conflict with the underlying graphene substrate (emphasis in red).	110
3.26	Schematic of the two possible configurations for BLG. In the top stack, sublattices are identified as S_1 (blue sites) and S_2 (black sites). The bottom SLG stack can consist of S_1 and S_3 (red sites) sublattices (subscript ₁), or S_2 and S_3 sublattices (subscript ₂).	113

List of Abbreviations

BCF	Burton-Cabrera-Frank (Theory)
BLG	Bilayer graphene
DFT	Density Functional Theory
DLA	Diffusion-Limited Aggregation
HMA	Hot-Monomer Aggregation
SLG	Single layer graphene
VASP	Venna Ab-initio Simulation Package
TLG	Trilayer graphene
TMA	Trimesic Acid
vdW	van der Waals

Chapters

Chapter 1: Introduction

Submonolayer Adsorbates

Adsorbate-substrate interactions may be one of the most fundamental processes in chemistry and physics; the study of how the electronic, chemical, electromagnetic, mechanical (among others) properties of a substrate change when an adsorbate is bound is the foundation of entire fields of study. Thus, in this work we intend to focus on the subtler effects occurring from (or alongside) physisorption at two different physical regimes. For these subtle physisorbed adsorbates some considerations have to be raised: not only should there be weak binding between adsorbate and substrate, but the coverage should be low enough that adsorbate-adsorbate interactions are unimportant and, thus, negligible. We are focused on gap opening in graphene at the atomic scale, and superthermal transient effects in diffusion-limited aggregation (DLA) at the microscopic one, so these considerations will be applied in different ways. Therefore, we consider surface effects in the limiting regime of submonolayer coverage: when the adsorbate coverage is dense enough to appreciably modify the physics of the substrate, but sparse enough to avoid masking the weak effects we are interested in.

At the microscopic level, we examine the transport properties of superthermal

monomers alongside traditional diffusion-limited aggregation (DLA). By focusing on the submonolayer regime we can ignore step dynamics [1] and multi-layer effects [2], concentrating on the poorly understood equilibrium behavior of these superthermal monomers. At the atomic level, we examine adsorbate-induced band gaps in graphene, particularly due to sublattice symmetry-breaking. As strain-induced effects have been studied from first principles [3] and experimentally [4], we consider submonolayer coverage of weakly binding adsorbates to minimize the contribution large deformations may have on the graphene substrate.

Diffusion-Limited Aggregation (DLA) and Transient Effects

Diffusion-Limited Aggregation (DLA) was the term coined for a, now seminal, computer model that attempted to explain the fractional power-law density correlations of common aggregates [5]. DLA owes its success to three essential features: the formalism's simplicity, the small dependence on physical input, and the ability to produce approximately self-similar complex behavior (much like natural systems do); and yet, despite its simplicity and usefulness, no full solution is known [6].

The many applications include: adsorption and diffusion of monomers before catalysis [7], nucleation and growth of thin films [8], formation of nanostructures at surfaces via self-assembly [9], crystal growth [10–12], nucleation and aggregation in epitaxial growth [13], and formation of 2-dimensional (and 3-dimensional) islands [14], among others. Though the applications have been extensive, the effects of transient motions (i.e. superthermal) have been mostly neglected.

We have introduced a rate-equations model that tackles island formation mediated by the presence of the transient motions [15]. We discuss both the conditions in which the effects reduce to the usual DLA description of island growth and in which they preclude superthermal island growth. Furthermore, we intend to extend this rate-equations model and include an examination of its applicability to experimental results, providing insight into the physical description of the hot-monomer effects at equilibrium.

Graphene's Band Structure and Future Electronics

Silicon has been the driving force of computational advancements for the past sixty years. Though modern engineering, science and medicine have relied on the properties of the material, and its abundance, the steady increase in device density for silicon based devices seems to be reaching a cusp. This preoccupation with the limits of silicon devices is evident not only for specific applications, e.g. SiO₂ has been the cornerstone of DRAM (volatile, but fast random access memory) for microelectronic devices for decades [16], but for modern digital electronics in general [17].

Though the need for these new materials, and associated new physics, is pressing, the remaining lifetime for silicon in consumer grade electronics can be as long as 30 more years [18]. This has opened the field to a wide variety of exotic new physics trying to tackle this generational problem [19], though they all effectively attempt to recreate the tunability, scalability (and ultimately manufacturability) of silicon [20]. Ever since the seminal work on graphene demonstrated that nearly-monolayer films behaved in semimetal fashion [21], graphene has become a promising candidate to become silicon's heir. Notably, graphene's electrical properties are certainly tunable, yet scalability remains an issue. Though mechanical exfoliation [21] remains a popular technique for laboratory purposes, large-scale growth of graphene films [22] and epitaxial graphene growth [23] have become candidates for the construction of wafer-scale graphene that a manufacturing industry would require [24].

As graphene is a gapless semimetal, graphene devices are not suitable for logic

operations [24]; however, the band structure of graphene can be modified and tuned to allow for a gapped state that can be used in logical devices. Among others, gaps have been obtained by modifying the widths of graphene nanoribbons [25], controlled in bilayer graphene by adjusting the carrier concentration between graphene layers via chemical doping [26], and tuned in bilayer graphene through a combination of a field-effect transistor (FET) and infrared microspectroscopy without chemical doping [27]. More interestingly, a mechanism of opening gaps through symmetry-breaking adsorbates has been observed in epitaxially grown graphene [28] (though this is by no means a settled issue [29]). Thus, the present work aims to explore, theoretically, how adsorbates on graphene could open tunable gaps: a small but necessary brick in the long road to finding new physics for future electronics beyond silicon.

Chapter 2: Microscopic Scale: Transient Mobility Effects

Introduction

When describing adsorption, nucleation and growth of films (and nanostructures), transient effects are largely ignored. Specifically, the kinetic energy contributions of the adsorbates are assumed to be irrelevant to the description of growth dynamics when compared to, for example, diffusive effects. The idea of describing the lateral mobility of monomers before chemisorption is not new [30]. However, surface phonon modes are usually thought to dissipate said kinetic energy via collisions, and are thus removed from equilibrium descriptions. Despite the fact that transient effects before chemisorption have been named in the literature for decades [31–34], and that numerical studies suggest kinetic energy contributions could have effects comparable to diffusion [35], theoretical models accounting for transient effects are rare. In the context of island nucleation, hot-monomer adsorption has been considered [36], and studied via Monte Carlo simulations [37] and one-dimensional analytics [38]. Furthermore, it should be noted that the kinetics of island growth have been tackled extensively through other methods, such as capture zone distribution analysis [39] and attachment-limited aggregation [40, 41]. However, it was until the semi quantitative treatment of island growth [42] and our own rate-equations model

for hot-monomer mediated nucleation [15], that the connection between transient effects and island growth has been made explicit.

In previous work [15], we provided a novel rate-equations model that explicitly connected the non-thermal behavior of deposited monomers to island growth rate. The formalism presented an analytic model for island growth both in the regime of small flux-deposition rate F , where DLA behavior should dominate, to large F , where a hot-monomer dominated regime is discovered. Additionally, definite scaling regimes are discovered: some mediated by the critical nucleus size and others by the characteristic energies of the system. A description for describing an effective growth exponent and activation energies are discussed, as it becomes necessary to discuss how the system behaves in between these definite regimes.

We extend our previous model by rigorously bounding our analytic solution, and demonstrating that power-law behavior is necessary and not a consequence of the experimental parameter space. Furthermore, these theoretical bounds give rise to a natural asymptotic approximation for the model that is shown to be robust in navigating the experimental parameter space and finding reasonable approximations to the critical nucleus size of the islands. After revisiting the puzzling behavior of certain organic molecular adsorbate systems [42] that were previously discussed [15], we introduce energy-dependent indexing of these limiting scaling regimes in order to meaningfully discuss transitions. More importantly, we provide a physical interpretation of our analytic solution, and interpret dimensionless parameters employed to simplify our closed equation of state to the distribution of unstable islands, and the activation energy. Finally, we provide a prescription for simpler analysis of other ex-

perimental systems, and manage to estimate the speed of the hot-monomers, which is the capstone to an analytic model of island growth motivated by superthermal effects.

Theoretical Development

Assume that non-reacting molecules (or atoms), hereafter referred to as *monomers* are deposited on a thin surface with high kinetic energy, which we regard as a *hot state*. The deposition occurs at a constant flux-deposition rate F , and they initially propagate ballistically for a time τ_h after thermalizing and propagating diffusively (in a random-walk fashion) with diffusion coefficient D . Specifically, the initial superthermal state in which the monomers enter the system can be modeled by considering the ballistic dynamics to occur at a fixed, superthermal, speed v . The total monomer density n , in units of particles per unit area, can be obtained by adding the densities of the ballistic n_h and the thermalized monomers n_{th} .

Additionally, both the hot and thermalized monomers can become absorbed into stable, i.e. non-decaying, islands with lifetimes $\tau_{h \rightarrow N}$ and $\tau_{th \rightarrow N}$, respectively. With these considerations, the evolution of the total monomer density $n \equiv n_h + n_{th}$, and the density of stable islands, N , can be modeled as follows:

$$\dot{n}_h = F - \frac{n_h}{\tau_h} - \frac{n_h}{\tau_{h \rightarrow N}}; \quad \dot{n}_{th} = \frac{n_h}{\tau_h} - \frac{n_{th}}{\tau_{th \rightarrow N}} \quad (2.1)$$

$$\dot{N} = \sigma(T, v) K(T, v) n^{i+1} \quad (2.2)$$

where $K(T, v)$ is the kinetic coefficient (see Eq. (2.5) below), $\sigma(T, v)$ is the capture coefficient (which traditionally depends on i), and i is the critical nucleus size, i.e. the size of the largest unstable (decaying) island. These adsorption mechanisms are illustrated in Fig. 2.1.

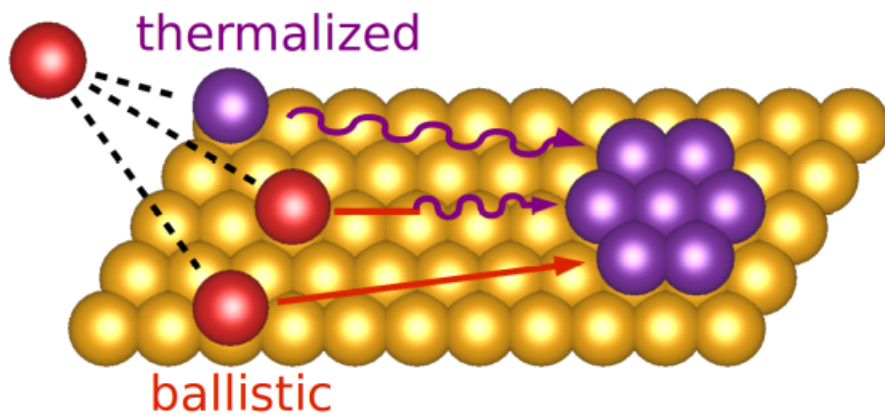


Figure 2.1: An idealized illustration of the adsorption mechanisms in the hot-monomer model. Thermalized monomers (red) are deposited on a substrate (yellow) at a flux-deposition rate F ; and they can be immediately adsorbed into a cluster (purple cluster) with lifetime $\tau_{h \rightarrow N}$. Hot-monomers have a lifetime τ_h before they become classical thermalized monomers (red), which can in turn become adsorbed into a cluster with lifetime $\tau_{th \rightarrow N}$. The interplay between these lifetimes is a key component of the various limiting regimes of the model.

It is important to note that deposition is the only mechanism increasing the density of hot-monomers n_h , while thermalization and island capture strictly decrease it; additionally, the thermalization process is the only mechanism considered to increase n_{th} . Naturally, the requirement that n only increases via deposition and only decreases by adsorption into stable islands can be checked from (2.1). It should be noted that in the regime of steady-state scaling behavior, the effects of monomer capture by other monomers or by unstable clusters ($s \leq i+1$) is largely ignored [8].

The lifetimes for the thermalized and ballistic monomers before adsorption into a sub-critical cluster can be obtained by relating them to an average time-of-flight for the monomers. Thus, by assuming that the mean travel distance is related to the mean separation between islands $\bar{\ell} = N^{-1/2}$, then:

$$\tau_{h \rightarrow N} = \frac{\bar{\ell}}{v} = \frac{1}{vN^{1/2}}; \quad \tau_{th \rightarrow N} = \frac{\bar{\ell}^2}{D} = \frac{1}{DN}, \quad (2.3)$$

We propose that the evolution of the density of clusters of size s (s -clusters), N_s , will be guided by the following rate equation:

$$\dot{N}_s = \sigma_{s-1} n N_{s-1} - \sigma_s n N_s + \frac{1}{\tau_{s+1}} N_{s+1} - \frac{1}{\tau_s} N_s \quad (2.4)$$

where τ_s and σ_s are the survival time before monomer detachment and the capture coefficient for a given s -cluster, respectively. This rate equation accounts for an increase in N_s by monomer detachment(capture) from $s+1(s-1)$ -clusters; evidently, a decrease in N_s is a direct consequence of s -clusters either capturing or

detaching a monomer. It should be noted that our rate equations do not consider detachment(capture) of more than one monomer at a time. At this stage some physical assumptions must be translated into initial conditions: $N_0 = 0$ and $\tau_1^{-1} = 0$, as monomer destruction is not considered (molecules decaying into smaller non-adsorbent or sublimating elements for instance); and $N_1 = n$ since monomers can be regarded as sub-critical 1-clusters. It follows that the so-called Walton relation [43] anticipated by (2.2) is recovered:

$$N_s = \left(\prod_{k=2}^s \sigma_{k-1} \tau_k \right) n^s \equiv K_s n^s \quad (2.5)$$

As an aside, the *classic* Walton relation could be written as $N_s = \exp(E_s^{\text{form}} \beta) n^s$, where E_s^{form} is the energetic contribution when forming the cluster. For our model, the temperature dependence for K_s is more complicated than an exponential form, but the idea of characteristic energies does remain (see Eqns. 2.9 - 2.10 on how β dependence is built into the kinetic coefficient). Furthermore, the *classic* Walton relation also connects the growth rate of stable islands \dot{N} , to the monomer density in power-law fashion: $\dot{N} \propto N_i \propto n^i$, where i is the critical nucleus size. Notably, we recover this classical result (2.7).

To solve our recovered Walton relation, we employ full mathematical induction: thus, check that Eqn. (2.5) holds for $s = 1$ (trivially satisfied for $N_1 = n$), and perform a single inductive step (where we exploit the steady-state assumption on

Eqn. 2.4):

$$\begin{aligned}
N_{s+1} &= \frac{\tau_{s+1} (1 + \sigma_s n \tau_s)}{\tau_s} N_s - \sigma_{s-1} n \tau_{s+1} N_{s-1} \\
&= \frac{\tau_{s+1} (1 + \sigma_s n \tau_s)}{\tau_s} \left(\prod_{k=2}^s \sigma_{k-1} \tau_k \right) n^s - \sigma_{s-1} n \tau_{s+1} \left(\prod_{k=2}^{s-1} \sigma_{k-1} \tau_k \right) n^{s-1} \\
&= \frac{\tau_{s+1}}{\tau_s} \left(\prod_{k=2}^s \sigma_{k-1} \tau_k \right) n^s + \sigma_s \tau_{s+1} \left(\prod_{k=2}^s \sigma_{k-1} \tau_k \right) n^{s+1} - \sigma_{s-1} \tau_{s+1} \left(\prod_{k=2}^{s-1} \sigma_{k-1} \tau_k \right) n^s \\
&= \frac{\tau_{s+1}}{\tau_s} \sigma_{s-1} \tau_s \left(\prod_{k=2}^{s-1} \sigma_{k-1} \tau_k \right) n^s + \left(\prod_{k=2}^{s+1} \sigma_{k-1} \tau_k \right) n^{s+1} - \sigma_{s-1} \tau_{s+1} \left(\prod_{k=2}^{s-1} \sigma_{k-1} \tau_k \right) n^s \\
&= \left(\prod_{k=2}^{s+1} \sigma_{k-1} \tau_k \right) n^{s+1} \tag{2.6}
\end{aligned}$$

Note that while the Walton relation provides the definition for K_s , the kinetic coefficient for subcritical clusters of size s , we are more concerned with the general kinetic coefficient $K(T, v)$. Correspondingly, its expression follows naturally by analyzing the stable island density as expressed in terms of super-critical clusters, $N \equiv \sum_{s \geq i+1} N_s$:

$$\begin{aligned}
\dot{N} &= \sum_{s \geq i+1} n (\sigma_{s-1} N_{s-1} - \sigma_s N_s) = \sigma_i n N_i \\
&= \sigma_i \left(\prod_{k=2}^i \sigma_{k-1} \tau_k \right) n^{i+1} \equiv \sigma(T, v) K(T, v) n^{i+1} \tag{2.7}
\end{aligned}$$

where (by definition of i) $\tau_s^{-1} = 0$ for $s > i$. A particularly comforting result is that both the kinetic and capture coefficients necessarily depend on the critical nucleus size: $K(T, v) = K_i$ and $\sigma(T, v) = \sigma_i$.

To obtain the expressions for $\sigma(T, v)$ and τ_s , it is necessary to consider how they behave under primarily diffusive or ballistic effects: quantitatively defining *fast*

and *slow* thermalization regimes. Said regimes are characterized by the dominant survival time in the system, viz. $\tau_h \ll \tau_{h \rightarrow N}$, and $\tau_h \gg \tau_{h \rightarrow N}$ for fast and slow thermalization, respectively. Equivalently, if we define the dimensionless parameter z :

$$z \equiv \tau_h / \tau_{h \rightarrow N} = v \tau_h N^{1/2}, \quad (2.8)$$

these limits become $z \ll 1$ and $z \gg 1$, respectively. Considering the existence of two well-defined limiting regimes, we express $\sigma(T, v)$ and τ_s^{-1} as linear combinations of the limiting regimes' contributions:

$$\tilde{\sigma}_s(T, v) = \frac{n_{th}}{n} \sigma_s^{th}(T) + \frac{n_h}{n} \sigma_s^B(v), \quad (2.9)$$

$$\frac{1}{\tilde{\tau}_s(T, v)} = \frac{1}{\tau_s^{th}(T)} + \frac{1}{\tau_s^B(v)}, \quad (2.10)$$

where subscripts *-th* and *-B* correspond to thermal and ballistic contributions, respectively. The capture coefficient is assumed to be a weighted average of the thermal and ballistic contributions, where the weight is the fraction of the monomers in a given state; in contrast, the decay rate of the sub-critical clusters is simply additive.

Analytic Solution

Now that we have a description for the dynamics in terms of the thermalization regimes, an exploration of each will provide an explicit dependence of the individual capture coefficients, and lifetimes. For fast thermalization, $\tau_h \ll \tau_{h \rightarrow N}$, there are negligibly few hot-monomers: $n \approx n_{\text{th}}$. Thermal effects overwhelm ballistic contributions, so $\sigma_s(T, v) \rightarrow \sigma_s^{\text{th}}(T)$ and $K(T, v) \rightarrow K^{\text{th}}(T)$, where *-th* refers to exclusively thermal contributions. Since the BCF formalism [44] applies,

$$\sigma_s^{\text{th}}(T) = D = D_0 e^{-\beta E_D}; \quad K^{\text{th}}(T) = \kappa_0 e^{\beta E_i} \quad (2.11)$$

where E_D is the diffusion energy, E_i is the cohesion energy of a cluster of size i , $\beta \equiv (k_B T)^{-1}$ is the inverse thermal energy, and D_0 and κ_0 are constants. It is simpler to work in terms of the coverage $\theta \equiv Ft$, so $\dot{N} = F dN/d\theta$. In the stationary regime, $\dot{n}_h = \dot{n}_{\text{th}} = 0$, (2.1) simplifies:

$$n_h = F\tau_h; \quad n_{\text{th}} = \frac{F}{DN}; \quad \frac{dN}{d\theta} = \kappa_0 \left(\frac{F}{D}\right)^i \frac{e^{\beta E_i}}{N^{i+1}}. \quad (2.12)$$

Furthermore, as $z \ll 1$, we find the familiar case of DLA. Integrating $dN/d\theta$ yields the DLA hallmarks [7–9, 45]:

$$\begin{aligned} N &= C^\alpha F^\alpha \exp\left[\beta \frac{iE_D + E_i}{i+2}\right] \\ C &= \frac{[(i+2)\kappa_0\theta]^{1/i}}{D_0}, \quad \alpha = i/(i+2) \end{aligned} \quad (2.13)$$

For slow thermalization, $z \gg 1$, we find a novel hot-monomer aggregation (HMA) regime: since our goal is to understand the scaling behavior of N_s rather than its distribution, we neglect the much-studied [8, 14, 46] dependence of σ_s on s . Thus, the pertinent effect on capture and decay is the superthermal speed v , which for dimensional reasons is regarded as $\sigma_s^B = \ell v$, where the coefficient ℓ is a characteristic microscopic length and B refers to this ballistic regime. Effectively, we are assuming that v is a proportionality constant for the capture coefficient in this regime. Since a hot-monomer colliding with a small cluster is likely to transfer energy to the latter and cause (thermally improbable) detachment of a previously attached monomer, we expect the lifetime should also be related to v . Adopting the simplest assumption that this athermal detachment rate is proportional to the monomer speed, we get the cluster decay rate $(\tau_s^B)^{-1} = v/\ell'$, where ℓ' is another microscopic length and v is once more a proportionality constant. The kinetic coefficient in the ballistic regime is then:

$$K_s^B = \left(\prod_{k=2}^s \sigma_{k-1}^B \tau_k^B \right) = (\ell \ell')^{s-1} \quad (2.14)$$

The noteworthy independence of K_s^B on v is robust, requiring only that σ_s^B and $(\tau_s^B)^{-1}$ have the same speed dependence; in the event that a non-linear function of v works as a proportionality constant, then the microscopic lengths can be dimensionally rescaled to accommodate that. Even if σ_s^B and $(\tau_s^B)^{-1}$ had different speed dependences, both would still be independent of T and F , so that the effective exponents and energies in Table 2.1 would not change [15]. For $n \approx n_h$, in steady-state,

and assuming $\ell = \ell'$ for simplicity:

$$n_h = \frac{F}{vN^{1/2}}; \quad n_{\text{th}} = \frac{F\tau_h^{-1}}{DvN^{3/2}}; \quad \frac{dN}{d\theta} = \frac{\ell K_i^B}{N^{\frac{i+1}{2}}} \left(\frac{F}{v}\right)^i, \quad (2.15)$$

which remarkably leads to the scaling form $N \propto F^\alpha$ with

$$N = C^\alpha F^\alpha, \text{ where } C = \frac{1}{v} \left[\frac{i+3}{2} (\ell K_i^B \theta) \right]^{1/i}, \text{ and} \\ \alpha = 2i/(i+3). \quad (2.16)$$

Interestingly, the same scaling exponent as in attachment-limited aggregation (ALA) [47–49] is obtained, which should be immediately surprising considering that ALA is highly dependent on thermally activated processes. Contrastingly, the novel HMA regime is effectively athermal, as demonstrated by the absence of temperature dependence on the coefficients of (2.15). The Walton relation in (2.4) can be generalized to accommodate the thermal and athermal contributions:

$$\dot{N}_s = \tilde{\sigma}_{s-1} n N_{s-1} - \tilde{\sigma}_s n N_s + \frac{1}{\tilde{\tau}_{s+1}} N_{s+1} - \frac{1}{\tilde{\tau}_s} N_s \quad (2.17)$$

which is justified by our discussion in (2.1) not assuming either thermal or athermal behavior. Thus, generalize (2.7) by substituting $\sigma_s \rightarrow \tilde{\sigma}_s$ and $\tau_s \rightarrow \tilde{\tau}_s$. Additionally, from our assumptions for the slow thermalization, along with distributional concerns, the s dependence of $\tilde{\sigma}_s$ and $\tilde{\tau}_s$ can be neglected. We are left with two undetermined lifetimes: τ_h for molecules before thermalization and τ_{th} for thermalized

monomers before adsorption into an island. Following the BCF model [44]:

$$\tau_s^{\text{th}} \equiv \tau_0 e^{\beta E_b}, \quad \tau_h \equiv \tau_0 e^{\beta E_{\text{ph}}}, \quad (2.18)$$

where τ_0 is a characteristic inverse phonon frequency, E_b is the barrier to detachment of a monomer from a cluster ($E_b > E_D$), and E_{ph} is a typical phonon energy. In the steady-state regime ($dt = 0$), the algebraic forms of n_h and n_{th} in (2.1) along with the survival time considerations in (2.3) allow us to solve (2.9) for the capture coefficient and monomer density:

$$n_h = \frac{F\tau_h}{1 + v\tau_h N^{1/2}} = ND\tau_h n_{\text{th}} \quad (2.19)$$

$$\tilde{\sigma} = \frac{n_h}{n\tau_h N} (1 + \ell v\tau_h N) = D \left(\frac{1 + \ell v\tau_h N}{1 + ND\tau_h} \right) \quad (2.20)$$

$$n = \left(\frac{F}{D} \right) \frac{1 + ND\tau_h}{N(1 + v\tau_h N^{1/2})} \quad (2.21)$$

By substituting (2.19-2.21) into (2.7) we obtain:

$$\frac{dN}{d\theta} = \frac{(\tau F)^i}{D\tau} \frac{(1 + ND\tau_h)(1 + \ell v\tau_h N)^i}{N^{i+1} (1 + v\tau_h N^{1/2})^{i+1}} \quad (2.22)$$

using the approximation $\ell \approx \ell'$ as before.

Growth Exponents

In the limits $z \ll 1$ and $z \gg 1$, the key characteristics of $dN/d\theta$ shown in (2.13) and (2.16), can be recovered to leading order in N : specifically, the dependence on F , N and the DLA and HMA/ALA scaling exponents. By inspecting (2.22), we note that this is a rational function of $N^{1/2}$ (evident after a change of variables from N), which guarantees an analytic solution via partial-fraction decomposition for arbitrary values of i . However, the result is both unenlightening (as no immediate results can be constructed) and unwieldy (as the actual value of i determines the functions in the solution). A more elegant approach is to study the dependence of N on six dimensionless parameters that can be formed from the physical quantities θ , F , D , τ_h , v , and $\tilde{\tau}$:

$$\begin{aligned} \hat{N} &\equiv N(v\tau_h)^2 = z^2; & \hat{F} &\equiv F\ell v\tau_h^2; & \hat{\theta} &\equiv \frac{\theta v}{D\ell}(v\tau_h)^4 \\ \mathcal{R}_C &\equiv \frac{\ell}{v\tau_0}e^{-\beta E_b}; & \mathcal{R}_n &\equiv ND\tau_h; & \mathcal{R}_B &\equiv \ell v\tau_h N \end{aligned} \quad (2.23)$$

Thus, (2.22) is solved implicitly:

$$\frac{\hat{\theta} \hat{F}^i}{(1 + \mathcal{R}_C)^{i-1}} = \int_0^{\hat{N}} f(\epsilon) d\epsilon, \quad f(\epsilon) \equiv \frac{\epsilon^{i+1} (1 + \epsilon^{1/2})^{i+1}}{(1 + R_n \epsilon)(1 + R_B \epsilon)^i}, \quad (2.24)$$

where we introduce $R_n \equiv \mathcal{R}_n/\hat{N}$ and $R_B \equiv \mathcal{R}_B/\hat{N}$ to easily identify prefactors of \hat{N} within numerical computations, and ϵ is an integration variable. In both the fast

and slow thermalization limits, one can unambiguously observe power-law behavior $N \propto F^\alpha$ and assign an exponent α . Thus, it is natural to define an *effective exponent* $\alpha_{\text{eff}}(F) \equiv d \ln N / d \ln F$ to account for scaling behavior in the transitional regime. The explicit form of α_{eff} follows directly from (2.24):

$$\alpha_{\text{eff}}(F) = \frac{i \int_0^{\hat{N}} f(\epsilon) d\epsilon}{\hat{N} f(\hat{N})} = i \langle 1 \rangle |_{\hat{N}} \quad (2.25)$$

where α_{eff} depends implicitly on F via \hat{N} . Note that we introduced a notational shorthand, $\langle \dots \rangle$:

$$\langle g \rangle |_{\hat{N}} \equiv [\hat{N} f(\hat{N})]^{-1} \int_0^{\hat{N}} f(\epsilon) g(\epsilon) d\epsilon. \quad (2.26)$$

where the \hat{N} indexation indicates that the arbitrary function g is indeed a function of \hat{N} . However, since we will only discuss functions of \hat{N} , said indexation is omitted from further notation.

The effective exponent, α_{eff} , has rich structure that can be accessed by varying \mathcal{R}_n , \mathcal{R}_B and z , as exemplified in Figs. (2.2-2.3) and tabulated in Table 2.1. Specifically, by exhausting the limits $\log_{10} z, \log_{10} \mathcal{R}_n, \log_{10} \mathcal{R}_B \rightarrow \pm\infty$, 8 separate plateaus (condensation regions) of α_{eff} are discovered. This motivates a physical interpretation of the dimensionless parameters: using the exact solution from (2.19) and our definition for the ballistic decay rate:

$$\mathcal{R}_C = \frac{\tau^B}{\tau^{\text{th}}}; \quad \mathcal{R}_n = \frac{n_h}{n_{\text{th}}}; \quad \mathcal{R}_B = \frac{\tau^B}{\tau_h} z^2 \quad (2.27)$$

These recast forms reveal that the coefficients act as channels indicating whether

or not different ballistic phenomena are in effect: the behavior of α_{eff} is chiefly modified by \mathcal{R}_n and \mathcal{R}_B , so a discussion of \mathcal{R}_C is left for later considerations of activation energy. An interpretation of these channels requires proper indexation of the regimes, so we identify states by the indexing D*** (H***), where D(H) indicates DLA (HMA), that is $z \ll (\gg)1$. The numbering relates the limits of \mathcal{R}_n , \mathcal{R}_B and \mathcal{R}_C , by a smooth mapping from $\mathcal{R} = [0, \infty)$ to $[0, 1)$ that depends on activation energy (see Eqn. 2.42). For the purposes of understanding the growth exponent, we only need to be concerned with the mapping's endpoints. It should be noted that a state with only two numerical indexes, e.g. D00, refers to D00*, i.e. any state regardless of \mathcal{R}_C behavior.

Notably, the effect of \mathcal{R}_n is quite straightforward: to act as the ratio between the density of hot-monomers to thermalized monomers, for which we consider it to be the *density channel*. Note that in Fig. (2.2) the effects on the effective exponent for the D00 \rightarrow D10 transition, are similar to the D01 \rightarrow D11 transition: in both an increase in the relative density of hot-monomers causes an increase of the ballistic effects in the fast thermalization region. However, this deformation of the growth exponent does not survive into the slow thermalization regime, as all modeled systems in Fig. (2.2) converge to the same limit in the slow thermalization regime. Analogously, Fig. (2.3) reveals a similar effect for the H10 \rightarrow H00 and H11 \rightarrow H01 transitions in the slow thermalization regime: a decrease in the relative density of hot-monomers impacts behavior in the slow thermalization regime that vanishes after the crossover into fast thermalization. The density channel, \mathcal{R}_n , welcomes a comfortably simple description: that an uncharacteristic change in the ratio of hot

to thermalized monomers will heighten ballistic effects in the fast thermalization regime, and diminish them in the slow thermalization one.

Unfortunately, \mathcal{R}_B defies such a clean interpretation to its analytic description (2.27). It is clear that the ratio of the ballistic component of the lifetime before adsorption into an island vs. the ballistic thermalization lifetime is of import; but the modulation by z (which sets thermalization regime) muddies this interpretation. Hence, \mathcal{R}_B does describe how important the ballistic effects are when compared to the dominant τ_h , but the effects are only observed in an uncharacteristic thermalization regime. Specifically, in the fast thermalization regime, not only do ballistic effects in island adsorption have to be large enough to offset the ballistic thermalization rate, but large enough to offset the general fast thermalization of the regime via z (similarly small enough in the slow thermalization regime to offset large z). This makes \mathcal{R}_B effects truly anomalous, challenging both the natural description of rates for a regime and the behavior of the regime itself: furthermore, why we regard \mathcal{R}_B as the *anomalous ballistics channel*. Note that in Fig. (2.2) the effects on the effective exponent for the D00 \rightarrow D01 transition are similar to the D10 \rightarrow D11 transition: dramatic in both scale (size of the growth exponent) and overall behavior (shape of the plateau). This is not unique to fast thermalization, as a similar effect is seen in the slow thermalization regime in Fig. (2.3) for the H01 \rightarrow H00 and H11 \rightarrow H10 transitions, where the smooth limiting plateau into α_{H11} is transformed into a sharp inflection at high z . Despite any effects presented by \mathcal{R}_n or \mathcal{R}_B , α_{eff} always converges to its limiting DLA (HMA) values for small (large) enough \hat{N} —or equivalently, for small (large) F or z : this is much more obvious when exploring the

full parameter space of α_{eff} Figs. (2.4 - 2.5). The crossover behavior can lock α_{eff} into plateaus of rational values, over which the island density exhibits well-defined power-law behavior (cf. various examples in Figs. 2.2-2.3). With Taylor expansions of (2.25) in \hat{N} or \hat{N}^{-1} , such values are found analytically and given in Table 2.1.

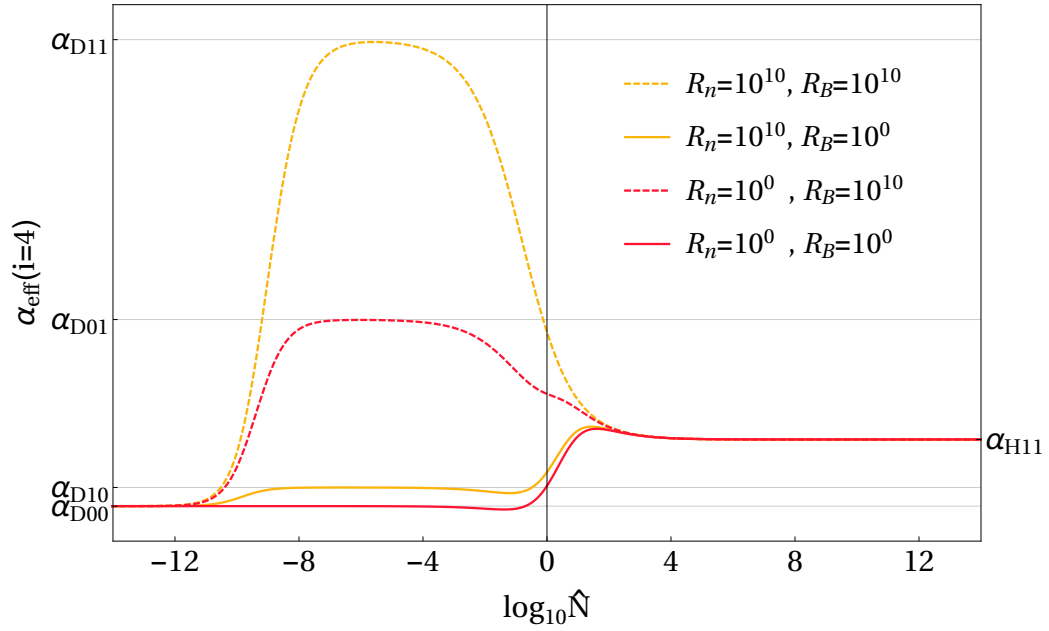


Figure 2.2: The effective exponent α_{eff} vs. $\hat{N}(F)$ for $i = 4$ with focus on the fast thermalization regime. The crossover region between the limiting DLA (D00) and HMA (H11) scaling is explored by varying R_n and R_B .

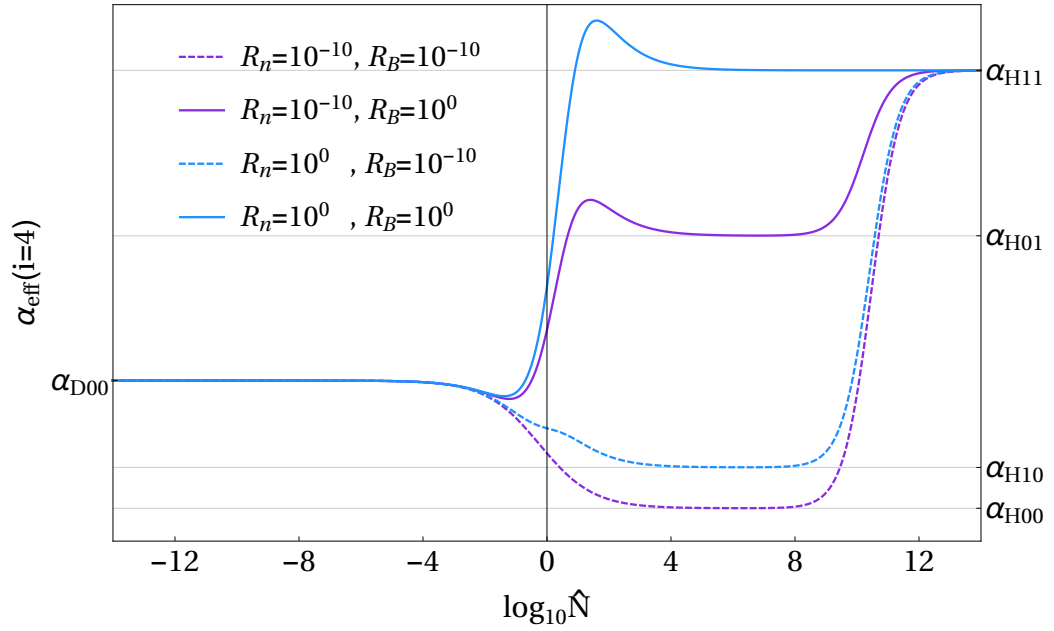


Figure 2.3: The effective exponent α_{eff} vs. $\hat{N}(F)$ for $i = 4$ with focus on the slow thermalization regime. The crossover region between the limiting DLA (D00) and HMA (H11) scaling is explored by varying R_n and R_B .

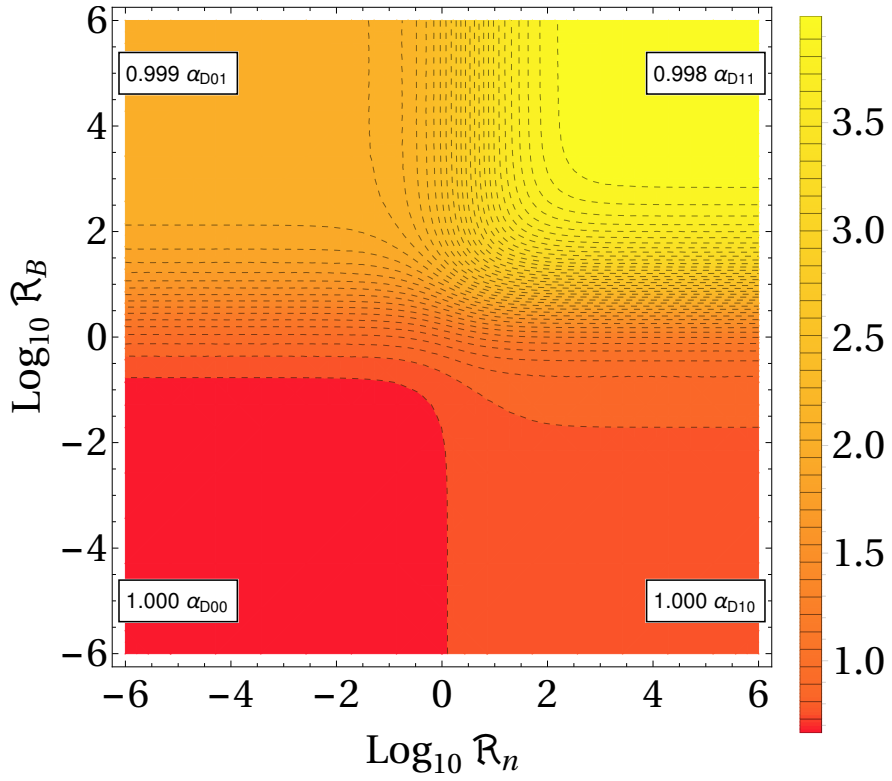


Figure 2.4: The effective exponent α_{eff} explored in the parameter space $(\mathcal{R}_n \times \mathcal{R}_B)$ in the fast thermalization regime $z = 10^{-6}$, $i = 4$. Note that as \mathcal{R}_n and \mathcal{R}_B tend to the limiting regimes ($\ll 1$ and $\gg 1$), the effective exponent matches the plateau values: $\alpha_{D00} = 2/3$, $\alpha_{D01} = 2$, $\alpha_{D10} = 4/5$, and $\alpha_{D11} = 4$.

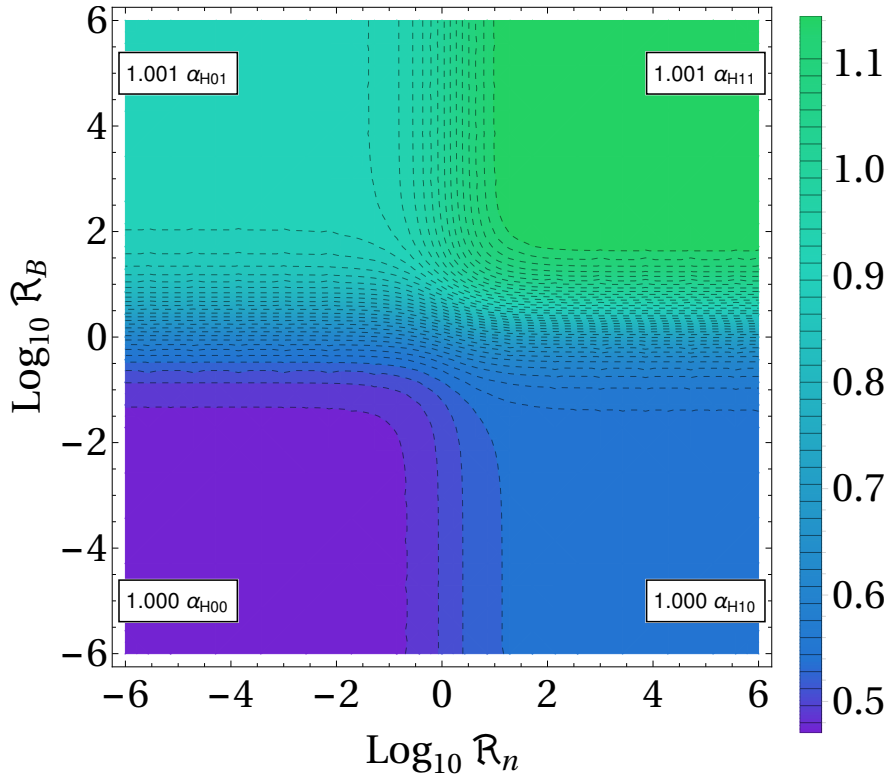


Figure 2.5: The effective exponent α_{eff} explored in the parameter space $(\mathcal{R}_n \times \mathcal{R}_B)$ in the slow thermalization regime $z = 10^{+6}$, $i = 4$. Note that as \mathcal{R}_n and \mathcal{R}_B tend to the limiting regimes ($\ll 1$ and $\gg 1$), the effective exponent matches the plateau values: $\alpha_{\text{H}00} = 8/17$, $\alpha_{\text{H}01} = 8/9$, $\alpha_{\text{H}10} = 8/15$, and $\alpha_{\text{H}11} = 8/7$.

Especially interesting, and relevant to experiments discussed below, is the behavior of the growth exponent at the plateaus. Consider Fig. 2.2, which has $i = 4$: in the interval $-8 \geq \log_{10} z \geq -4$, and $\log_{10} R_n = 10$, $\log_{10} R_B = 0$ (solid yellow line), a cursory analysis of the growth exponent would lead to the conclusion that the system is in a well-behaved DLA state. Since the growth exponent shows $\alpha_{D10} = 4/5$, one would naturally infer from a DLA analysis that $i = 8$ ($8/10 = 4/5$). In fact, $i = 4$ as $\alpha_{D10} = i/(i + 1)$. For a more exotic state such as D01 (dotted red line), DLA analysis would lead to seemingly impossible results: $\alpha_{D01} = i/2 = 2$, which implies (incorrectly) a DLA exponent of $i = -4$. Without our ballistic considerations, these plateaus would, at best, refer to DLA behavior with grossly different growth exponents, and, at worst, to un-physical DLA regimes. It is important to mention though, that this DLA interpretation is unavoidable if experimental data for a system is limited to a small region in phase space, as in regions close to the plateaus, the power-law regimes will make a DLA interpretation (albeit with a wrong i), mathematically reasonable.

Approximations to Analytic Solution

We note that both the full analytic solution (2.24), and the effective activation energy (2.25) have a close connection with the kernel. Rewriting the effective exponent to highlight the importance of the kernel:

$$\begin{aligned}\alpha_{\text{eff}}(F) &= \frac{i \int_0^{\hat{N}} f(\epsilon) d\epsilon}{\hat{N} f(\hat{N})} = \frac{i}{\hat{N}} \left[\frac{\frac{\partial}{\partial \hat{N}} \int_0^{\hat{N}} f(\epsilon) d\epsilon}{\int_0^{\hat{N}} f(\epsilon) d\epsilon} \right]^{-1} \\ &= \frac{i}{\hat{N}} \left[\frac{\partial}{\partial \hat{N}} \ln \int_0^{\hat{N}} f(\epsilon) d\epsilon \right]^{-1}\end{aligned}\quad (2.28)$$

shows that the functional behavior of $f(\epsilon)$ has direct repercussions on the shape of the activation energy, and thus, on the location of the limiting regimes. Consider an arbitrary power-law relationship $\psi = a\epsilon^b$; then, the modified logarithmic derivative:

$$\frac{\partial \ln \psi}{\partial \ln \epsilon} = \frac{\partial (\ln a + b \ln \epsilon)}{\partial \ln \epsilon} = b \quad (2.29)$$

describes the power-law exponent b . Therefore, f_L , the modified logarithmic derivative of the kernel, would adequately describe the kernel's power-law structure (even at transitional regimes):

$$\begin{aligned}f_L &= \frac{\partial \ln f(\hat{N})}{\partial \ln \hat{N}} = \frac{\partial \ln f}{\partial f} \cdot \frac{\partial f}{\partial \hat{N}} \cdot \frac{\partial \hat{N}}{\partial \ln \hat{N}} = \frac{\hat{N}}{f} \frac{\partial f}{\partial \hat{N}} \\ &= (i+1) \left[1 + \frac{z}{2+2z} \right] - \frac{\mathcal{R}_n}{1+\mathcal{R}_n} - \frac{i\mathcal{R}_B}{1+\mathcal{R}_B}\end{aligned}\quad (2.30)$$

To globally maximize (minimize) f_L , we require solving for all possible extrema. Note that finding local extrema requires solving an 8-th degree polynomial in z due to the term $(1+z)^2(1+\mathcal{R}_n)^2(1+\mathcal{R}_B)^2$ in the denominator of f'_L . Fortunately, since all terms (2.30) exhibit monotonic growth, it is sufficient to consider the behavior at the endpoints of the parameter space $(z, \mathcal{R}_n, \mathcal{R}_B)$. Thus, f_L is bounded, as it exhibits global minima and maxima at $(0, \infty, \infty)$ and $(\infty, 0, 0)$, respectively:

$$0 \leq f_L \leq \frac{3}{2}(i+1). \quad (2.31)$$

We can then make the formal argument for $f(\epsilon)$ behaving in power-like fashion, with its behavior as a kernel dominated by the largest values of ϵ in the integration regime. Therefore, to approximate the growth exponent in (2.25) it is valid to expand the kernel about the values closest to the upper integration limit:

$$\begin{aligned} \alpha_{\text{eff}} &\approx \frac{i}{\hat{N}} \left[\frac{\partial}{\partial \hat{N}} \ln \int_0^{\hat{N}} f(\hat{N}) d\epsilon \right]^{-1} = \frac{i}{\hat{N}} \left[\frac{\partial}{\partial \hat{N}} \ln \hat{N} f(\hat{N}) \right]^{-1} \\ &= \frac{i}{\hat{N}} \left[\frac{\hat{N} f(\hat{N})}{f(\hat{N}) + \hat{N} \frac{\partial}{\partial \hat{N}} f(\hat{N})} \right] = \frac{i}{1 + \frac{\hat{N}}{f(\hat{N})} \frac{\partial f(\hat{N})}{\partial \hat{N}}} \\ &= \frac{i}{1 + f_L} \end{aligned} \quad (2.32)$$

This approximation results in a natural definition for an *asymptotic approximation* to the effective exponent, and leads to a simplified equation of state:

$$\alpha_{\text{eff}}^{\text{asy}}(F) = \frac{i}{1 + \frac{\hat{N}}{f(\hat{N})} \frac{\partial f(\hat{N})}{\partial \hat{N}}}, \quad \hat{F}^i = \hat{N} f(\hat{N})$$

$$2i/(3i + 5) \leq \alpha_{\text{eff}}^{\text{asy}} \leq i \quad (2.33)$$

with $\alpha_{\text{eff}}^{\text{asy}}$ strictly bound by the behavior of the logarithmic derivative. Note that the bounding values correspond to the smallest and largest plateaus found in Table (2.1) by exploring parameter space. Since both the channel-decay information and the initial coverage dependence have been eliminated, this approximation does lose important β behavior. Furthermore, consider the plateaus in the effective growth exponent as described by the approximation:

$$\begin{aligned} 0 &= \frac{\partial \alpha_{\text{eff}}}{\partial \hat{N}} = -\frac{i}{\hat{N}^2} \frac{\int_0^{\hat{N}} f(\epsilon) d\epsilon}{f(\hat{N})} + \frac{i}{\hat{N}} - \frac{i}{\hat{N}} \frac{\int_0^{\hat{N}} f(\epsilon) d\epsilon}{f(\hat{N})^2} \frac{\partial f}{\partial \hat{N}} \\ &= -\frac{\alpha_{\text{eff}}}{\hat{N}} + \frac{i}{\hat{N}} - \frac{\alpha_{\text{eff}}}{f} \frac{\partial f}{\partial \hat{N}} \rightarrow \alpha_{\text{eff}} = \alpha_{\text{eff}}^{\text{asy}} \quad \text{at plateaus.} \end{aligned} \quad (2.34)$$

so not only is the asymptotic approximation bound by the same extrema as the full solution, but it reproduces the plateaus from the exact solution. More than a mathematical artifact, these plateaus are important regions in parameter space, as they describe the metastable regimes for the system. Thus, at the expense of losing exactness when dealing with Arrhenius data at transition regimes, we gain computational efficiency without losing information about the critical nucleus size. Though unsuitable for a complete understanding of the island growth, when analyzing unknown systems, this is an acceptable trade off in order to obtain a first estimate for the general critical nucleus size governing the system.

The effectiveness of the approximate solution $\alpha_{\text{eff}}^{\text{asy}}$ at modeling the full system can be explored by analyzing its fractional difference with the full solution. Con-

sistent with $\alpha_{\text{eff}}^{\text{asy}}$ sensitivity to the behavior of f_L , the asymptotic approximation is most effective at the extrema, $\log_{10} \mathcal{R}_n, \log_{10} \mathcal{R}_B, \log_{10} z \rightarrow \pm\infty$ (see Figs. 2.6 - 2.7); contrastingly, for $z = 10^0$, the asymptotic approximation is overall less effective in determining definite regimes (see Fig. 2.8) (the concern being not the magnitude of the error, but how non-monotonic the domains are). For $i = 4$, the asymptotic approximation is then reliable to within 10% for the slow thermalization and transitional regimes, and up to 18% for the fast thermalization regime: the highest discrepancy comes from the transitional values of the anomalous channel, \mathcal{R}_B , for all three cases. Ultimately, the asymptotic approximation is a useful initial guess to fit experimental data to our model. Considering the large parameter space we are dealing with, an educated guess for the likely region of parameter space that is being sampled by experiment is crucial before embarking on a full modeling of the system.

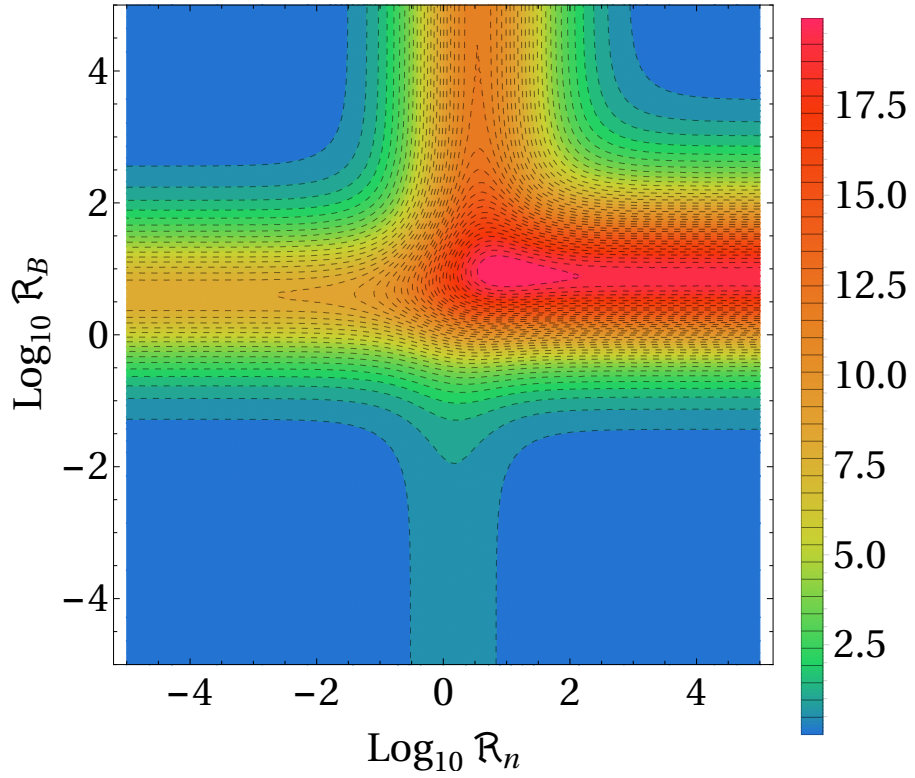


Figure 2.6: The percentage difference, $|\alpha_{\text{eff}} - \alpha_{\text{eff}}^{\text{asy}}|/\alpha_{\text{eff}}$, between the growth exponent α_{eff} , and its asymptotic approximation $\alpha_{\text{eff}}^{\text{asy}}$ explored in the parameter space $(\mathcal{R}_n \times \mathcal{R}_B)$ for the fast thermalization regime (established by fixing $z = 10^{-6}$) and $i = 4$. Note the presence of a large error about $\mathcal{R}_B \sim 1$. General monotonic features are observed, as values in the parameter space are fixed to the D** regime ($z \ll 1$).

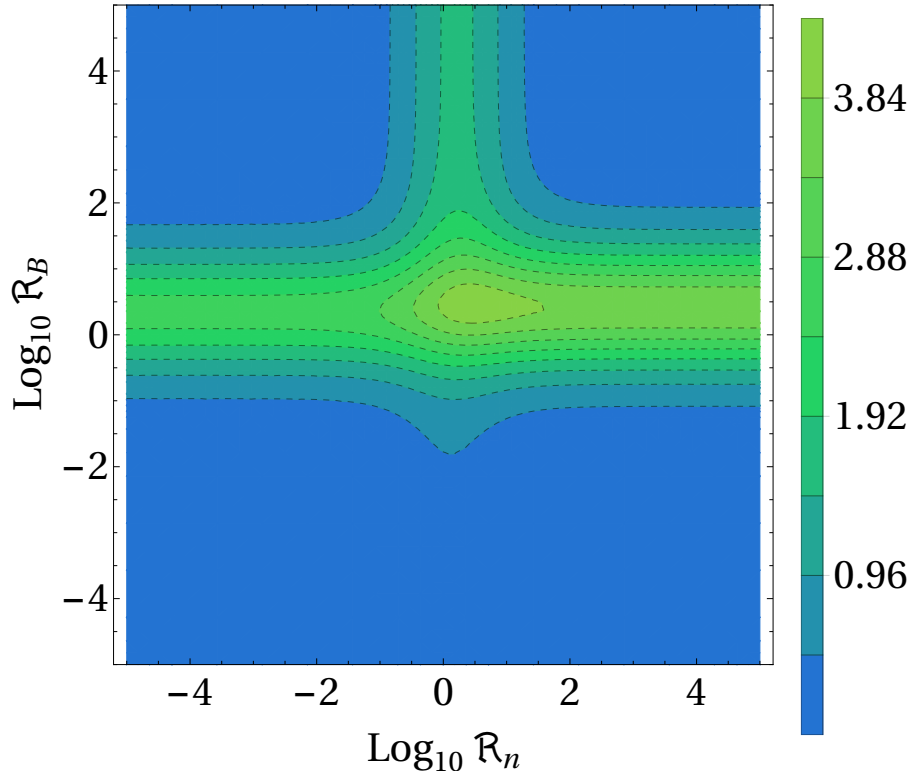


Figure 2.7: The percentage difference, $|\alpha_{\text{eff}} - \alpha_{\text{eff}}^{\text{asy}}|/\alpha_{\text{eff}}$, between the growth exponent α_{eff} , and its asymptotic approximation $\alpha_{\text{eff}}^{\text{asy}}$ explored in the parameter space $(\mathcal{R}_n \times \mathcal{R}_B)$ for the slow thermalization regime (established by fixing $z = 10^{+6}$) and $i = 4$. Note the presence of a slight error about $\mathcal{R}_B \sim 1$. General monotonic features are observed, as values in the parameter space are fixed to the H^{**} regime ($z \gg 1$).

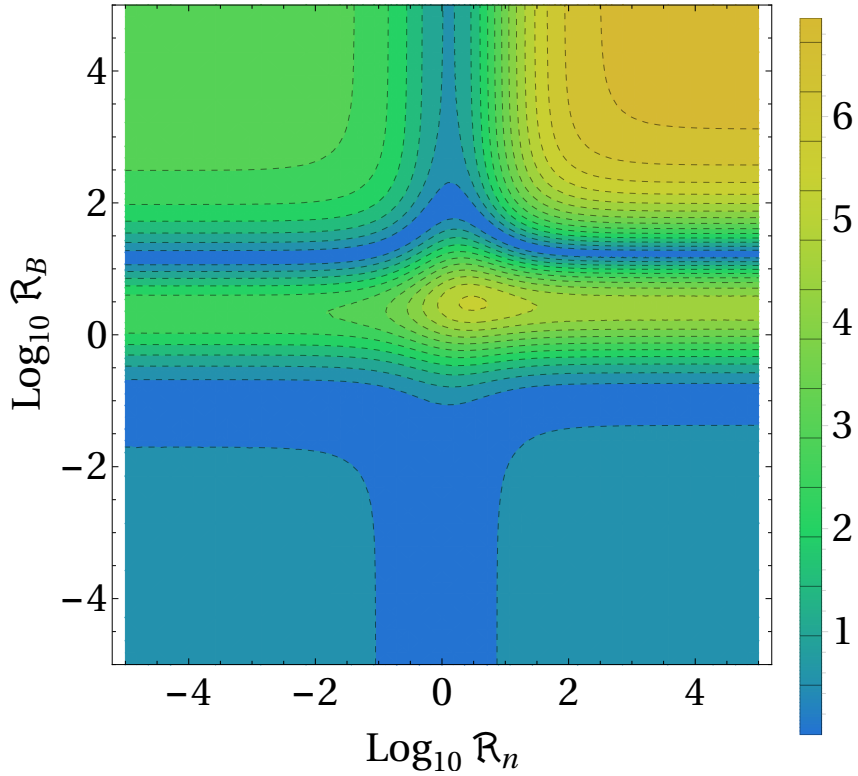


Figure 2.8: The percentage difference, $|\alpha_{\text{eff}} - \alpha_{\text{eff}}^{\text{asy}}|/\alpha_{\text{eff}}$, between the growth exponent α_{eff} , and its asymptotic approximation $\alpha_{\text{eff}}^{\text{asy}}$ explored in the parameter space $(\mathcal{R}_n \times \mathcal{R}_B)$ for the transitional thermalization regime (established by fixing $z = 10^0$) and $i = 4$. Note the increasing error with increasing \mathcal{R}_B and at $\mathcal{R}_B \sim 1$. Non-monotonic features are observed, particularly for $\mathcal{R}_B \sim 1$ and $\mathcal{R}_n \sim 1$, as values in this region of parameter space are transitional (not in a limiting regime).

Activation Energy

In simple cases of surface growth, the density of stable islands is expected to change with temperature as $N \propto \exp(\beta E_A)$, where E_A is a well-defined *activation energy*. For general cases, we seek an *effective activation energy*, $E_A^{\text{eff}} \equiv d \ln N / d\beta$, in order to meaningfully talk about energy scaling in the transitional regions (where the temperature dependence is not simple). Making a change of variables from dN to $d\hat{N}$ gives:

$$\begin{aligned} E_A^{\text{eff}} &\equiv \frac{d \ln N}{d\beta} = \frac{1}{N} \frac{dN}{d\beta} = \frac{1}{N (v\tau_0)^2} \frac{d(\hat{N} e^{-2\beta E_{ph}})}{d\beta} \\ &= \frac{e^{-2\beta E_{ph}}}{N (v\tau_0)^2} \left(\frac{d\hat{N}}{d\beta} - 2E_{ph} \hat{N} \right) = \frac{1}{\hat{N}} \frac{d\hat{N}}{d\beta} - 2E_{ph} \end{aligned} \quad (2.35)$$

Thus, showing that the *effective activation energy* can be recast in terms of the dimensionless variable \hat{N} , with a minor modification in terms of the phonon energy.

By differentiating both sides of (2.24) by β :

$$\begin{aligned} \frac{d}{d\beta} \left[\int_0^{\hat{N}} f(\epsilon) d\epsilon \right] &= f(\hat{N}) \frac{d\hat{N}}{d\beta} + \int_0^{\hat{N}} \partial_\beta f(\epsilon) d\epsilon, \text{ with} \\ \int_0^{\hat{N}} \partial_\beta f(\epsilon) d\epsilon &= \int_0^{\hat{N}} f(\epsilon) \left[\frac{(E_D + E_{ph})\mathcal{R}_n}{1 + \mathcal{R}_n} + i \frac{E_{ph}\mathcal{R}_B}{1 + \mathcal{R}_B} \right] d\epsilon. \end{aligned} \quad (2.36)$$

and,

$$\begin{aligned} &\frac{d}{d\beta} \left[\frac{\hat{\theta} \hat{F}^i}{(1 + \mathcal{R}_C)^{i-1}} \right] \\ &= \left[(4 + 2i)E_{ph} + E_D + (i - 1) \frac{E_b \mathcal{R}_C}{1 + \mathcal{R}_C} \right] \int_0^{\hat{N}} f(\epsilon) d\epsilon \end{aligned} \quad (2.37)$$

we find the β dependence implicit, through kernel derivatives. By equating (2.36) and (2.37) we find:

$$\begin{aligned} \frac{1}{\hat{N}} \frac{d\hat{N}}{d\beta} &= E_b(i-1) \frac{\mathcal{R}_C}{1+\mathcal{R}_C} \langle 1 \rangle + iE_{ph} \left\langle \frac{\mathcal{R}_B}{1+\mathcal{R}_B} \right\rangle \\ &+ \left\langle \frac{2iE_{ph}}{1+\mathcal{R}_B} \right\rangle + \left\langle \frac{E_D}{1+\mathcal{R}_n} \right\rangle - \left\langle \frac{E_{ph}\mathcal{R}_n}{1+\mathcal{R}_n} \right\rangle + \langle 4E_{ph} \rangle \end{aligned} \quad (2.38)$$

Since the term $-2E_{ph}$ can be rewritten as:

$$\begin{aligned} -2E_{ph} &= -2E_{ph} \frac{1}{\hat{N}f(\hat{N})} \int_0^{\hat{N}} \frac{\partial}{\partial \epsilon} [\epsilon f(\epsilon)] d\epsilon \\ &= -E_{ph}(i+1) \left\langle \frac{z}{1+z} \right\rangle - 2iE_{ph} \left\langle \frac{1}{1+\mathcal{R}_B} \right\rangle \\ &+ 2E_{ph} \left\langle \frac{\mathcal{R}_n}{1+\mathcal{R}_n} \right\rangle - 4E_{ph} \langle 1 \rangle \end{aligned} \quad (2.39)$$

The combined results of (2.38), (2.39), and (2.35) give an explicit form for the activation energy:

$$\begin{aligned} E_A^{\text{eff}} &= E_b(i-1) \left\langle \frac{\mathcal{R}_C}{1+\mathcal{R}_C} \right\rangle - E_{ph}(i+1) \left\langle \frac{z}{1+z} \right\rangle \\ &+ iE_{ph} \left\langle \frac{\mathcal{R}_B}{1+\mathcal{R}_B} \right\rangle + \left\langle \frac{E_D}{1+\mathcal{R}_n} + \frac{E_{ph}\mathcal{R}_n}{1+\mathcal{R}_n} \right\rangle \end{aligned} \quad (2.40)$$

Here the bracket notation from (2.26) is employed, while z , \mathcal{R}_C , \mathcal{R}_B , and \mathcal{R}_n remain functions of \hat{N} (important to note that \mathcal{R}_C is a constant in terms of the operator, but is depicted as shown in (2.40) for symmetry). Two constraints follow naturally from these results: first, the condition that $z(\beta \rightarrow 0) \rightarrow 0$ (no stable islands at

infinite temperature), imposes a fixed value for $\hat{\theta}\hat{F}^i$:

$$\hat{\theta}\hat{F}^i\Big|_{\beta=0} = (1 + \mathcal{R}_C)^{i-1} \int_0^{\hat{N}} f(\epsilon) d\epsilon\Big|_{\beta=0} \quad (2.41)$$

It should be pointed out that since our model deals with equilibrium states, the *initial* density of stable islands is described in terms of β -space, and not temporally: this explains why the initial conditions are linked to the deposition rate F and the final coverage at equilibrium. Second, in the limit $\beta \rightarrow \infty$, (2.24) implies $\hat{N} \rightarrow \infty$ if $E_D > E_{ph}$, as \mathcal{R}_n would vanish in the kernel. Physically, at zero temperature the density of stable islands should be *large*, but undeniably finite: hence, $E_{ph} \geq E_D$ is necessary. With these considerations, there are $2^4 = 16$ energetic regimes realizable by varying z , \mathcal{R}_n , \mathcal{R}_B and \mathcal{R}_C . Notice that we can identify pairs of effective energies E_A^{eff} to growth exponents, and illustrate their primary dependence on the original energies by a clever division by $\langle 1 \rangle$: the regimes are presented in Table 2.1, with representative plots in Figs. (2.9) - (2.12).

Label	\mathcal{R}_n	\mathcal{R}_B	\mathcal{R}_C	$\alpha_{\text{eff}} = i\langle 1 \rangle$	$E_A^{\text{eff}}/\langle 1 \rangle = E_A^{\text{eff}}i/\alpha_{\text{eff}}$
D ₀₀₀	$\ll 1$	$\ll 1$	$\ll 1$	$i/(i+2)$	E_D
D ₀₀₁	$\ll 1$	$\ll 1$	$\gg 1$	"	$E_D + (i-1)E_b$
D ₀₁₀	$\ll 1$	$\gg 1$	$\ll 1$	$i/2$	$E_D + iE_{ph}$
D ₀₁₁	$\ll 1$	$\gg 1$	$\gg 1$	"	$E_D + iE_{ph} + (i-1)E_b$
D ₁₀₀	$\gg 1$	$\ll 1$	$\ll 1$	$i/(i+1)$	E_{ph}
D ₁₀₁	$\gg 1$	$\ll 1$	$\gg 1$	"	$E_{ph} + (i-1)E_b$
D ₁₁₀	$\gg 1$	$\gg 1$	$\ll 1$	i	$(1+i)E_{ph}$
D ₁₁₁	$\gg 1$	$\gg 1$	$\gg 1$	"	$(1+i)E_{ph} + (i-1)E_b$
H ₀₀₀	$\ll 1$	$\ll 1$	$\ll 1$	$2i/(3i+5)$	$E_D - (i+1)E_{ph}$
H ₀₀₁	$\ll 1$	$\ll 1$	$\gg 1$	"	$E_D - (i+1)E_{ph} + (i-1)E_b$
H ₀₁₀	$\ll 1$	$\gg 1$	$\ll 1$	$2i/(i+5)$	$E_D - E_{ph}$
H ₀₁₁	$\ll 1$	$\gg 1$	$\gg 1$	"	$E_D - E_{ph} + (i-1)E_b$
H ₁₀₀	$\gg 1$	$\ll 1$	$\ll 1$	$2i/(3i+3)$	$-iE_{ph}$
H ₁₀₁	$\gg 1$	$\ll 1$	$\gg 1$	"	$-iE_{ph} + (i-1)E_b$
H ₁₁₀	$\gg 1$	$\gg 1$	$\ll 1$	$2i/(i+3)$	0
H ₁₁₁	$\gg 1$	$\gg 1$	$\gg 1$	"	$(i-1)E_b$

Table 2.1: The 16 regimes for extremal values of z , \mathcal{R}_n , \mathcal{R}_B and \mathcal{R}_C , along with the associated rescaled effective exponents (cf. Figs. 2.2-2.3) and effective activation energies. D (H) indicates DLA (HMA): $z \ll (\gg)1$. The subscripts give the limiting value of the \mathcal{R} 's, with 1 denoting $\mathcal{R} = \infty$, i.e. $\text{index} = \exp(-1/\mathcal{R})$. For α_{eff} , \mathcal{R}_C is inconsequential, so that only the first 2 subscripts are needed, yielding just 8 regimes. Note that the reduced values of E_A^{eff} in the last column must be multiplied by the corresponding α_{eff}/i to get the actual E_A^{eff} .

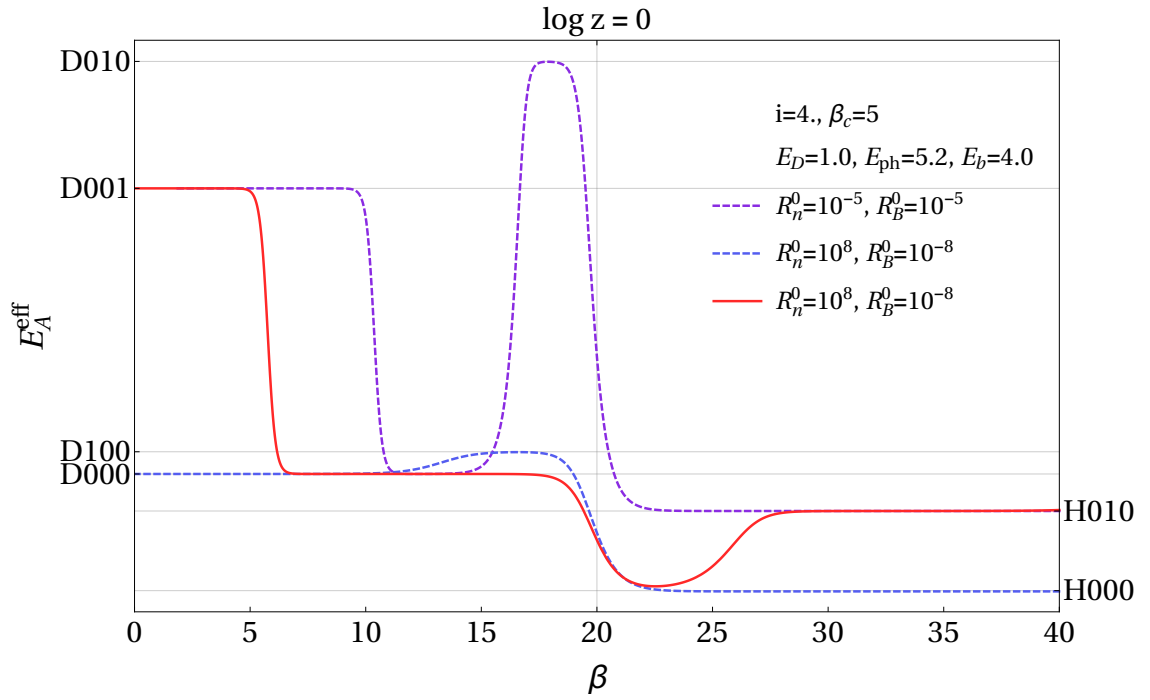


Figure 2.9: E_A^{eff} vs. β for $i=4$ and some values of R_n^0 and R_B^0 , R_x^0 meaning $R_x(\beta=0)$. The fast (slow) thermalization regimes are left (right) of the crossover value $z=1$ (note F and θ are chosen to satisfy $z(\beta_c=20)=1$). Energies are chosen so that $\mathcal{R}_C \ll 1$.

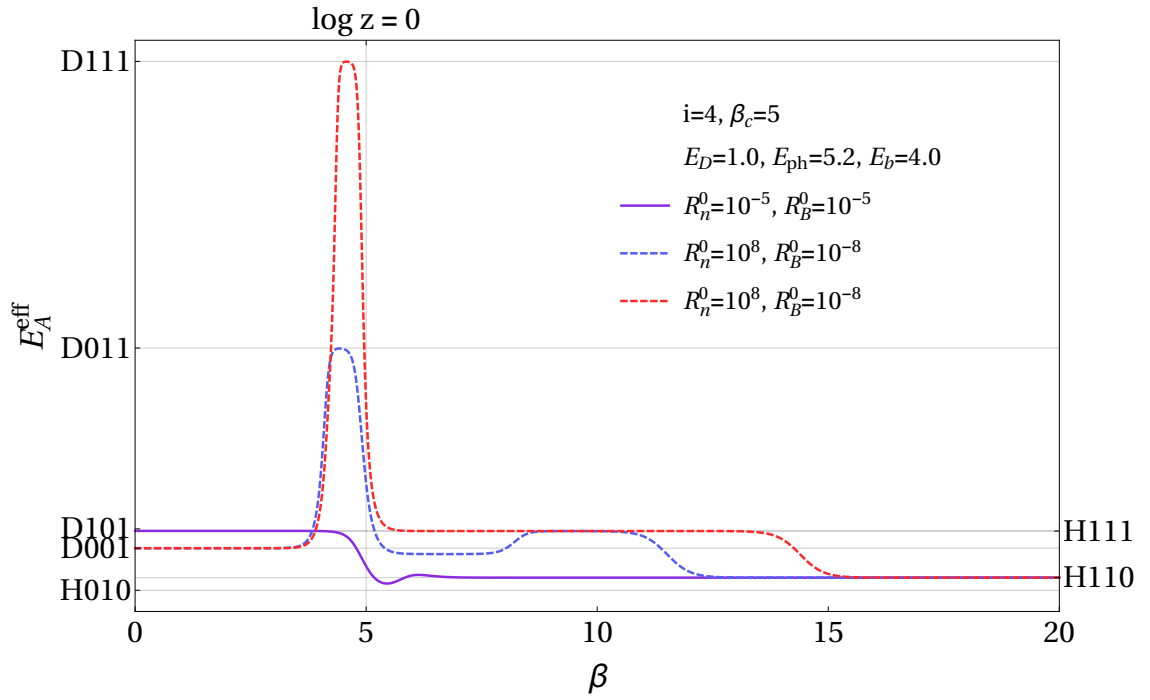


Figure 2.10: E_A^{eff} vs. β for $i = 4$ and some values of R_n^0 and R_B^0 , R_x^0 meaning $R_x(\beta = 0)$. The fast (slow) thermalization regimes are left (right) of the crossover value $z = 1$ (note F and θ are chosen to satisfy $z(\beta_c = 5) = 1$). Energies are chosen so that $\mathcal{R}_C \gg 1$.

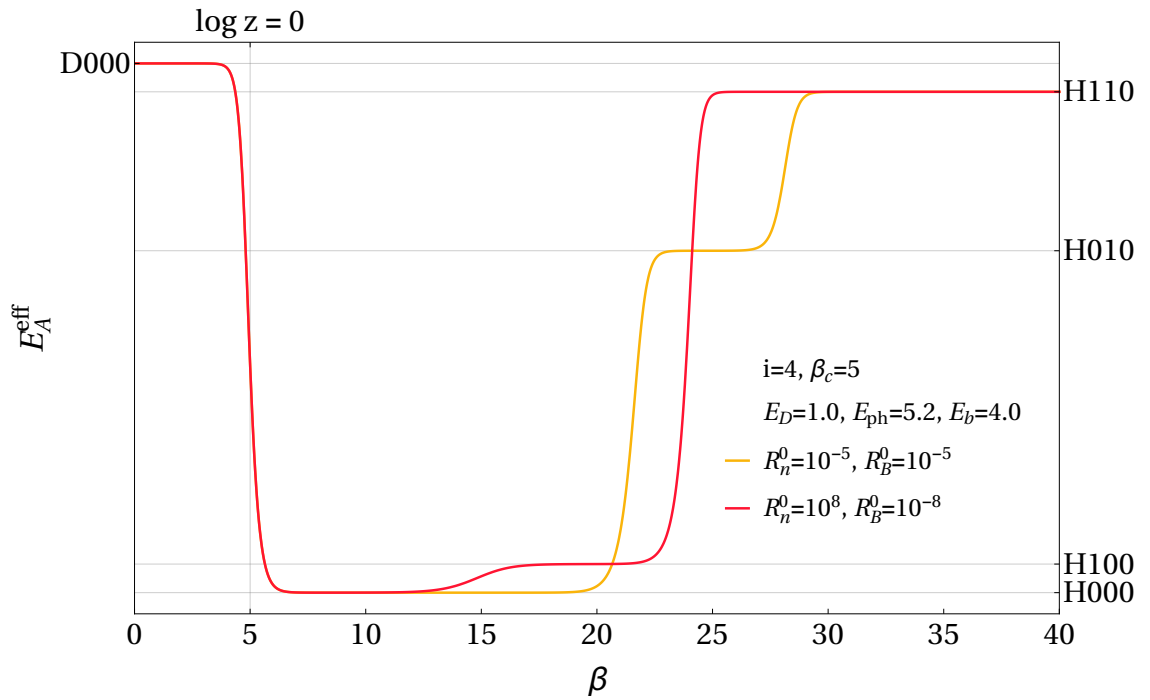


Figure 2.11: E_A^{eff} vs. β for $i = 4$ and some values of R_n^0 and R_B^0 , R_x^0 meaning $R_x(\beta = 0)$. The fast (slow) thermalization regimes are left (right) of the crossover value $z = 1$ (note F and θ are chosen to satisfy $z(\beta_c = 5) = 1$). Energies are chosen so that $\mathcal{R}_C \ll 1$.

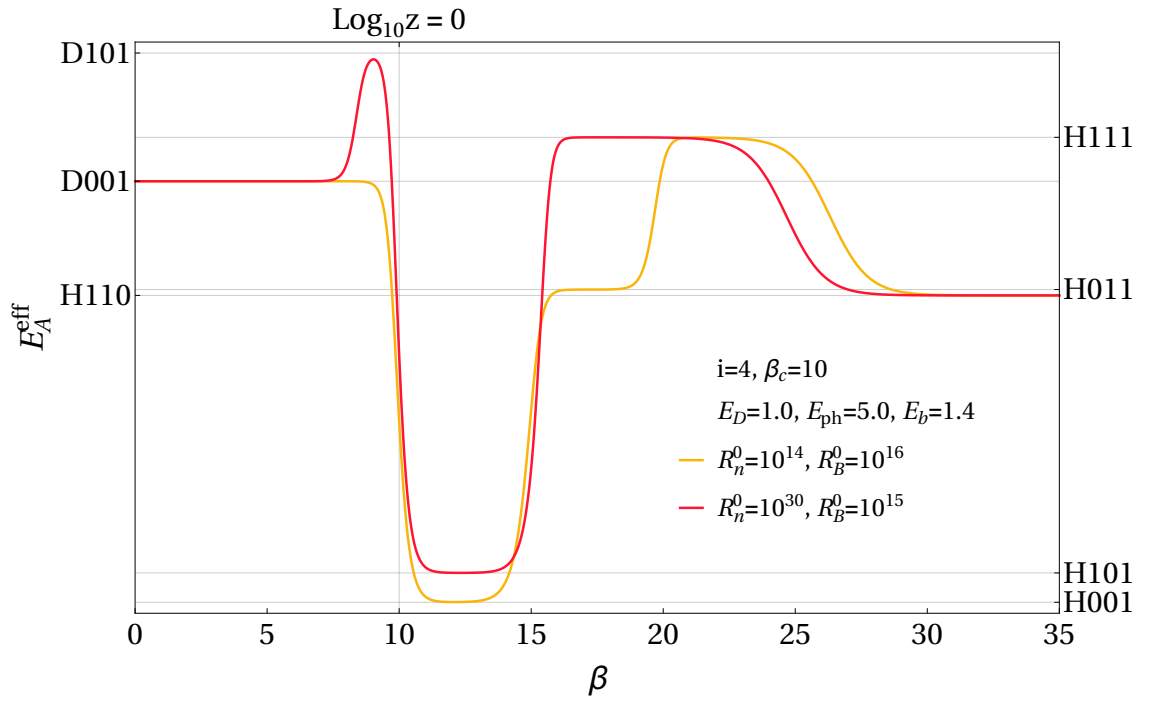


Figure 2.12: E_A^{eff} vs. β for $i = 4$ and some values of R_n^0 and R_B^0 , R_x^0 meaning $R_x(\beta = 0)$. The fast (slow) thermalization regimes are left (right) of the crossover value $z = 1$ (note F and θ are chosen to satisfy $z(\beta_c = 10) = 1$). Energies are chosen so that $\mathcal{R}_C \gg 1$.

Additional insight into the activation energy can be gained by interpreting the effect of the limiting \mathcal{R} values on the rescaled form $E_A^{\text{eff}}/\langle 1 \rangle$. Consider the distribution, f_s , of the unstable clusters $N_{s \leq i}$. Since $f_s \propto N_s$, $N_s = K_s n^s$ implies $f_s \propto (\tilde{\sigma} \tilde{\tau} n)^s$.

For the *thermalization parameter* the distribution becomes $f_s \propto n^s \propto z^{-s}$. This indicates that the energy contribution is related to the behavior of hot-monomers in the dynamics, namely the energy E_{ph} . In the slow thermalization regime, $z \gg 1$ ($\beta \rightarrow \infty$), with $N \rightarrow 0$; we expect a negative energetic contribution (decreasing stable islands) with monomers dominating the unstable clusters ($f_1 \rightarrow 1$). The dominating mechanism is then monomers attaching to the most common stable island, N_{i+1} , which suggests a contribution by the E_{ph} with a pre-factor $i + 1$. In contrast, the fast thermalization regime, $z \ll 1$ ($\beta \rightarrow 0$) has ($f_i \rightarrow 1$), which suggests no monomer effects and no energetic contribution. The second term on the right hand side of (2.40) reflects these effects.

In the case of the *anomalous ballistics channel*, the distribution becomes $f_s \propto \tilde{\sigma}^s \propto \mathcal{R}_B^s$. This indicates that the energy contribution is related to the capture dynamics of hot-monomers, again, the energy E_{ph} . For $\mathcal{R}_B \gg 1$ ($\beta \rightarrow \infty$), with $N \rightarrow \infty$; we expect a positive energetic contribution (increasing stable islands) with the largest unstable clusters dominating the dynamics ($f_i \rightarrow 1$). The main mechanism is then, monomers attaching to the largest unstable island, N_i , which suggests a contribution by E_{ph} with a prefactor i . In contrast, for $\mathcal{R}_B \ll 1$ ($\beta \rightarrow 0$), with $f_1 \rightarrow 1$, which suggests no real unstable islands (other than monomers) so no net energetic contribution is expected. The third term on the right hand side of

(2.40) reflects these effects. Note that this explains the behavior of the *anomalous ballistics channel*: when either $z, \mathcal{R}_B \gg 1$ or $z, \mathcal{R}_B \ll 1$, the energetic contributions approximately cancel each other. In the regimes where they act in opposite ways: $z, \mathcal{R}_B^{-1} \gg 1$ or $z, \mathcal{R}_B^{-1} \ll 1$, we see a dramatic change in the activation energy of $|iE_{ph}|$, explaining the aforementioned anomalies.

For the *density channel*, the distribution depends on the limit of \mathcal{R}_n itself. Given $\mathcal{R}_n \gg 1$ ($\beta \rightarrow \infty$), $f_s \propto \exp(s\beta E_{ph})$ with $N \rightarrow \infty$. As $f_i \rightarrow 1$, we expect a positive energetic contribution related to the largest unstable islands, N_i , capturing monomers to become stable and scaled by the energy E_{ph} . Contrastingly, for $\mathcal{R}_n \ll 1$ ($\beta \rightarrow 0$), $f_s \propto \exp(s\beta E_D)$ with $N \rightarrow 0$. Since $f_i \rightarrow 1$ is also reproduced, we expect a similar positive energetic contribution, but scaled by E_D instead. The fourth term on the right hand side of (2.40) reflects these effects, which notably do not depend on i . We attribute this independence from the critical nucleus size as the reason \mathcal{R}_n is such a well-behaved parameter.

Finally, we consider $\mathcal{R}_C = \tau^B/\tau^{\text{th}}$, the ratio of the ballistic component of the monomer lifetime, to the thermalization lifetime for hot-monomers. In short, this sets a timescale for the different lifetimes in the system, suggesting \mathcal{R}_C should be identified as the *timescale channel*. The distribution of sub-critical clusters is given by $f_s \propto \tilde{\tau}^s = (1 + \mathcal{R}_C)^{-s}$. Given $\mathcal{R}_C \gg 1$ ($\beta \rightarrow 0$) with $N \rightarrow 0$, then $f_1 \rightarrow 1$. Thus, we expect a positive energetic contribution related to the net effect of unstable islands $N_{s \leq i}$ decaying into monomers, i.e., the energy E_b with prefactor $(i - 1)$ as linearly modeled islands have $(i - 1)$ bonds. Contrastingly, for $\mathcal{R}_C \ll 1$ ($\beta \rightarrow \infty$), $f_s \propto 1$ with $N \rightarrow \infty$. As no subcritical clusters dominate, there is no net energetic

contribution given that unstable islands are as likely to absorb or detach a monomer. The first term on the right hand side of (2.40) reflects these effects.

A tabulation of these results is given in Table (2.2). Moreover, for the regimes in Table (2.1), it should be noted that $z \gg 1$ (slow thermalization regime) allows values of E_A^{eff} to be negative: notably when $E_{ph} > E_B$. The observation of $E_A^{\text{eff}} < 0$ in similar surface experiments [50–52] was attributed to a Langmuir-Hinshelwood mechanism [53, 54]. Here the key phenomenon is the onset of long-distance ($\gg \ell'$) ballistic motion with decreasing T that competes with diffusive aggregation to reduce N over a range of T [15].

Label	\mathcal{R}	Limit	f_s	Dominant sub-critical cluster ($f_x \rightarrow 1$)	$E_A^{\text{eff}}/\langle 1 \rangle = E_A^{\text{eff}}i/\alpha_{\text{eff}}$ contribution
(* 0 * *)	\mathcal{R}_n	$\ll 1$	$\exp(\beta E_{ph}s)$	f_i	$+E_D$
(* 1 * *)	\mathcal{R}_n	$\gg 1$	$\exp(\beta E_Ds)$	f_i	$+E_{ph}$
(* * 0 *)	\mathcal{R}_B	$\ll 1$	\mathcal{R}_B^s	f_1	0
(* * 1 *)	\mathcal{R}_B	$\gg 1$		f_i	$+iE_{ph}$
(* * * 0)	\mathcal{R}_C	$\ll 1$	$(1 + \mathcal{R}_C)^{-s}$	None	0
(* * * 1)	\mathcal{R}_C	$\gg 1$		f_1	$+(i - 1)E_b$
(D * * *)	z	$\ll 1$	z^{-s}	f_i	0
(H * * *)	z	$\gg 1$		f_1	$-(i + 1)E_{ph}$

Table 2.2: The 8 possible individual energy contributions to the activation energy E_A^{eff} for extremal values of z , \mathcal{R}_n , \mathcal{R}_B and \mathcal{R}_C . D (H) indicates DLA (HMA): $z \ll (\gg)1$. The subscripts give the limiting value of the \mathcal{R} 's, with 1 denoting $\mathcal{R} = \infty$, i.e. $\text{index} = \exp(-1/\mathcal{R})$. An asterisk (*) indicates an arbitrary value. Note that the reduced values of E_A^{eff} in the last column must be multiplied by the corresponding α_{eff}/i to get the actual E_A^{eff} .

Experimental Fit

Consider the growth experiment for hexaphenyl (6P) deposited on sputter-modified mica (001), in which the behavior of island density was mapped against flux-deposition rate at different temperatures $T = 150, 200, 300,$ and 400K [55–57]. Although our model is arguably closed, the high dimensionality of the space along with the integral dependence make fitting to experiment a highly difficult proposition. In previous work [15], we attempted a fit that was descriptive, but had difficulties presenting a quantitative value for v . Using the following formalism, we attempt to provide a fit that accounts for v and leans heavily on the asymptotic approximation for *sensible* initial conditions:

1. In this treatment, the critical nucleus size i is an integer, so consider fixed values of i : for a given value of i fit the experimental data to the asymptotic approximation (2.33) to obtain a broad description of the parameter space.
2. Augment the asymptotic solution with a temperature dependent prefactor, see the left side of (2.24), to create a hybrid solution in order to obtain values for energies.
3. Fit to the full solution (2.24), and obtain values for i and v .
4. Discard all solutions that do not exhibit superthermal speeds: the one with the largest correlation is the most representative fit.

The fitted results (see Table 2.3) can be arranged with respect to correlation

parameter ($0 \geq r^2 \geq 1$), expected thermal speed, and superthermal monomer speed v .

Using this rigorous formalism, we are able to distinguish different values for the energies (in eV) $E_D = 0.0170$, $E_{ph} = 0.0171$, and $E_b = 0.333$, which obey $E_D < E_{ph}$, E_b . In addition, we estimate the critical nucleus size $i = 4 \pm 1$, which is consistent with $i = 5 \pm 2$ and $i = 7 \pm 2$ estimated experimentally [57]. Finally, we find sensible values for the speed of hot-monomers $\log_{10} v (\mu\text{m/s}) = 8.5$, the undetermined lifetime prefactor $\log_{10} \tau_0(\text{s}) = -11.05$, and the characteristic length $\log_{10} \ell(\mu\text{m}) = 2.61$.

A valid concern is whether the asymptotic approximation creates a false fit, so an analysis of the error when compared with the full solution is desirable. We plot the parameter space of $\mathcal{R}_n \times \mathcal{R}_B$ (cf. Fig. 2.14) and recover a straight-line dependence (as $\mathcal{R}_n \sim \mathcal{R}_B$), but most importantly, we estimate an error of 2 – 18% for the transitional region of \mathcal{R}_B (which is not unexpected). Hence, the approximation gives sensible initial values to the full solution. More dramatically, the growth exponent evolves monotonically in the experimental space (cf. Fig. 2.13), and it is clear that the experiment describes a transitional regime. The effective growth exponent changes on each temperature run, but for any fixed β it is purely transitional as metastable states would be represented as sharp elevation changes in (cf. Fig. 2.13)

i	r^2	Range $\log_{10} v_{\text{rms}}$ ($\mu\text{m/s}$)	$\log_{10} v$ ($\mu\text{m/s}$)	Superthermal?
1	0.824	[8.0, 8.2]	5.1	No
2	0.981	[8.0, 8.2]	6.4	No
3	0.979	[8.0, 8.2]	6.6	No
4	0.979	[8.0, 8.2]	8.5	Yes
5	0.941	[8.0, 8.2]	5.4	No
6	0.945	[8.0, 8.2]	5.9	No

Table 2.3: The converged fits for different values of i . The results for $i = 4$ are in bold, as they are the best fitting results that describe hot-monomers being superthermal.

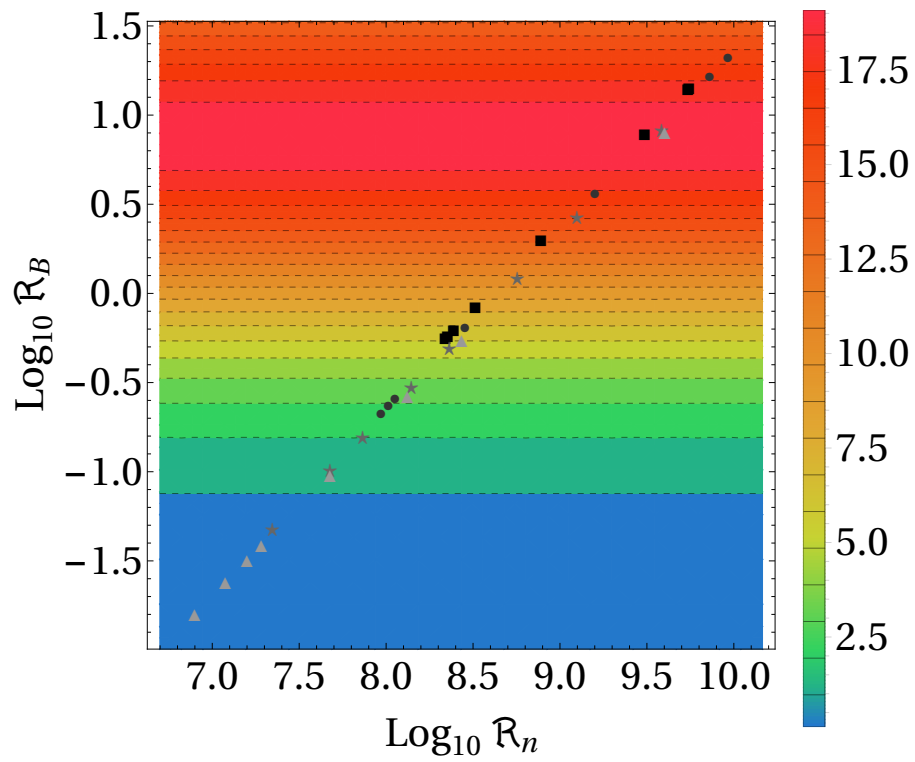


Figure 2.13: The percentage difference, $|\alpha_{\text{eff}} - \alpha_{\text{eff}}^{\text{asy}}|/\alpha_{\text{eff}}$, between the growth exponent α_{eff} , and its asymptotic approximation $\alpha_{\text{eff}}^{\text{asy}}$ in the parameter space for the experiment [57]. Note the experimental data lies on the $\mathcal{R}_n \sim \mathcal{R}_B$ diagonal, as anticipated by $\mathcal{R}_n = \frac{D}{\ell v} \mathcal{R}_B$ (see 2.23).

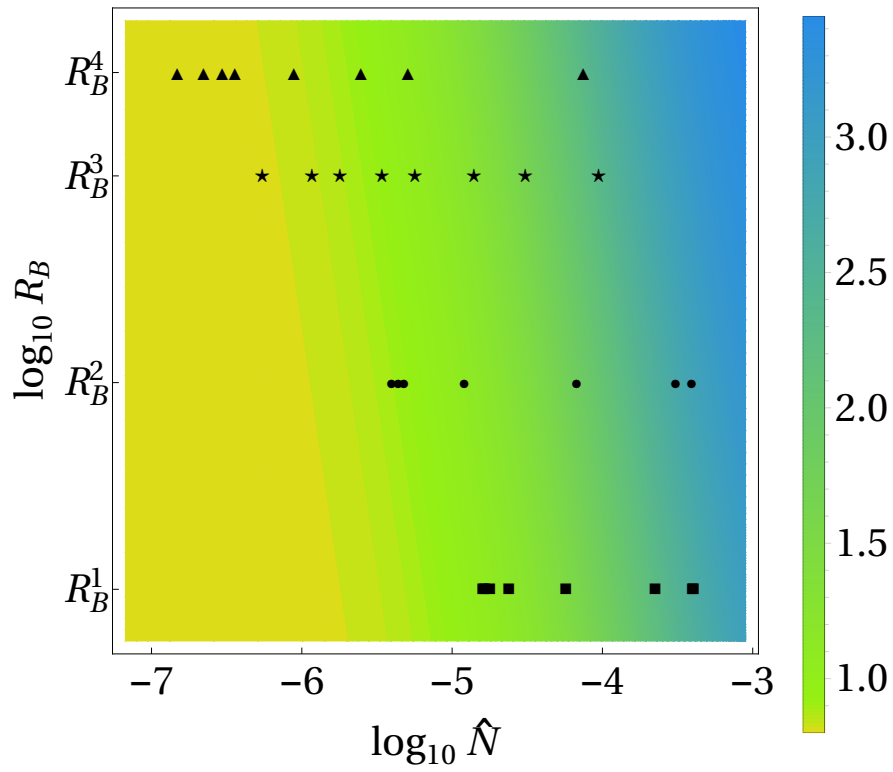


Figure 2.14: The effective exponent α_{eff} explored in the parameter space $(\mathcal{R}_n \times \mathcal{R}_B)$ in the fast thermalization regime $z = 10^{-6}$, $i = 4$ for the experiment [57]. Note the gradual change of the growth exponent throughout the sampled parameter space.

The notation devised in Table 2.1 to describe states is unambiguous for the limits $\mathcal{R}^\pm \rightarrow 0$. In a technical sense, there are infinitely many monotonic parametrizations of the real interval $[0, 1]$ to the open interval $[0, \infty)$, so we need a physically compelling extension to this notation in order to accommodate transitional states. Note that the general structure of the effective activation energy (2.40) relies on terms of the form $\left\langle \frac{R_x}{1+R_x} \right\rangle$, which present the limits: $\lim_{R_x \rightarrow 0} \left\langle \frac{R_x}{1+R_x} \right\rangle \rightarrow 0$, and $\lim_{R_x \rightarrow \infty} \left\langle \frac{R_x}{1+R_x} \right\rangle \rightarrow \langle 1 \rangle$. Hence, it is natural to define a *dynamic-index*:

$$J_x \equiv \left\langle \frac{R_x}{1+R_x} \right\rangle \cdot \frac{1}{\langle 1 \rangle} \quad (2.42)$$

More than a mere notational complication, this insight allows us to understand that the effective activation energy is not only proportional to the effective exponent (via $\langle 1 \rangle$), but that the impact of the theoretical energies establish a well-defined way to discuss transitional states in our model. When investigating the behavior of the indexes in the domain sampled by experiment (see Figs. 2.15-2.18), one can now identify states (see Table 2.4). Using the dynamic indexes we can explain the experimental evolution in the experiment [57]. First, all temperature runs exist in the fast thermalization regime, with $\mathcal{R}_n \ll 1$. Indeed, the *density channel* implies the system consists of mostly thermalized monomers. In the case of \mathcal{R}_C , the fixed β for each run necessarily fixes \mathcal{R}_C , so \mathcal{R}_C is a constant for each run. For $\beta = 77.4, 58.0 \text{ eV}^{-1}$, $\mathcal{R}_C \ll 1$, so the *timescale channel* introduces no energetic effects since the ballistic component of the decay lifetime for the monomers is relatively short lived. For $\beta = 38.7 \text{ eV}^{-1}$, \mathcal{R}_C shows a dynamic index of 0.3, which we describe

as transitional. Furthermore, for $\beta = 29.0\text{eV}^{-1}$, $\mathcal{R}_C \gg 1$ with a full transition into D0*1. In this instance, the *timescale channel* implies the ballistic component of the decay lifetime has moved from being a long timescale to being the dominant timescale.

True to its name, the *anomalous ballistic channel* presents dynamic changes for each run. In general we expect a transition from dynamic index 0.2 to dynamic index 0.9. Hence, for each β we can see the following transition: from \mathcal{R}_B effects being masked by $z \ll 1$, to \mathcal{R}_B effects overwhelming z and introducing energetic anomalies. Ultimately, the ballistic component of the lifetime eventually overwhelms the thermalization lifetime of the hot-monomers; and one can interpret the transitions as activating the \mathcal{R}_B channel. In all four instances, the most notable effect is the transition from $\mathcal{R}_B \ll 1$ to $\mathcal{R}_B \gg 1$, and thus, the addition of an iE_{ph} energetic term to the rescaled activation energy which is the source of the transitional scaling in the growth exponent. Previously, this transitional scaling was understood to lead to two critical nucleus size regimes in the experiment [57].

Inverse Temperature (β) (eV ⁻¹)	Low F State	High F State
77.4	D(0 0.4 0)	D(0 0.9 0)
58.0	D(0 0.3 0)	D(0 0.9 0)
38.7	D(0 0.2 0.3)	D(0 1 0.3)
29.0	D(0 0.1 0.9)	D(0 1 0.9)

Table 2.4: The dynamic indexes for each of the four experimental runs, for $i = 4$ at fixed β . D (H) indicates DLA (HMA): $z \ll (\gg)1$; and the numbers represent the dynamic indexes for \mathcal{R}_n , \mathcal{R}_B and \mathcal{R}_C , respectively.

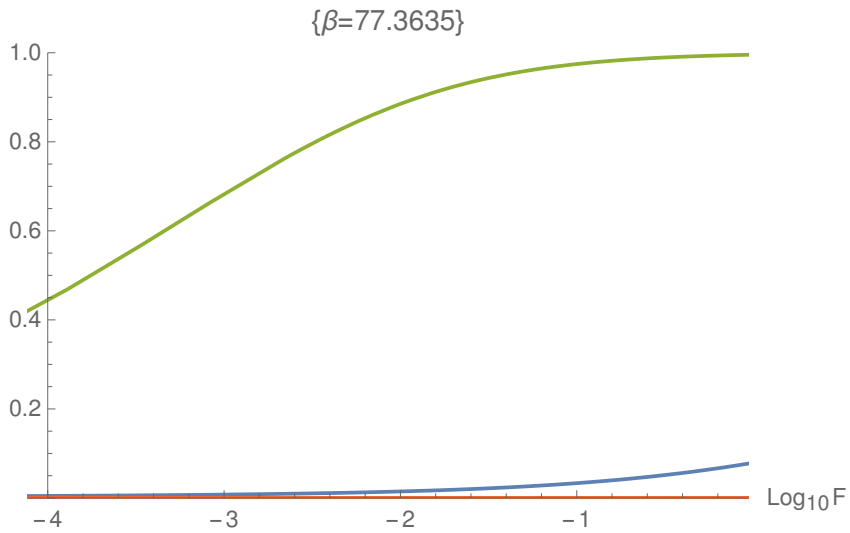


Figure 2.15: *Dynamic-index*, J_x as given in 2.42, values for \hat{z} (blue), \mathcal{R}_B (green), \mathcal{R}_C (red-concealed by horizontal axis), and \mathcal{R}_n (yellow-concealed by horizontal axis) vs. $\log_{10} F$ for $\beta = 77.36 \text{ eV}^{-1}$ and F in the sampled experimental range. As constructed, the index is constrained to the $[0, 1]$ interval. The dynamic index for \mathcal{R}_B is notable, as it is the only one transitioning for this temperature run from 0.4 at low F to 0.9 at high F . Since $\mathcal{R}_n, \mathcal{R}_C \ll 1$, they appear close to the horizontal axis.

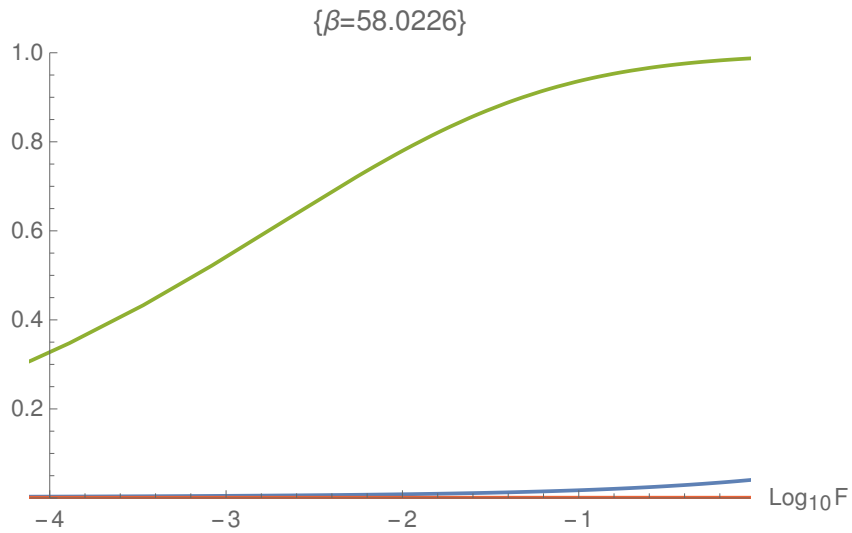


Figure 2.16: *Dynamic-index, J_x as given in 2.42, values for \hat{z} (blue), \mathcal{R}_B (green), \mathcal{R}_C (red-concealed by horizontal axis), and \mathcal{R}_n (yellow-concealed by horizontal axis) against $\log_{10} F$ for $\beta = 58.02 \text{ ev}^{-1}$ and F in the sampled experimental range. As constructed, the index is constrained to the $[0, 1]$ interval. The dynamic index for \mathcal{R}_B is notable, as it is the only one transitioning for this temperature run from 0.3 at low F to 0.9 at high F . Since $\mathcal{R}_n, \mathcal{R}_C \ll 1$, they appear close to the horizontal axis.*

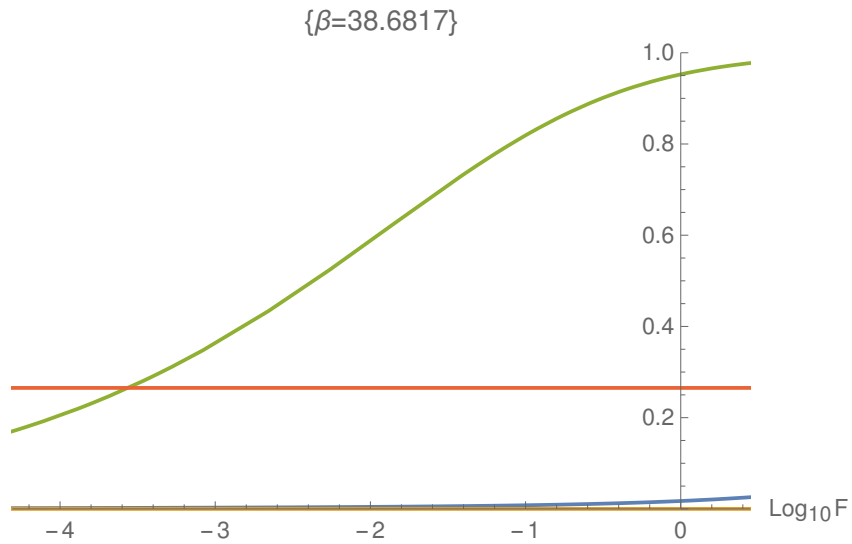


Figure 2.17: *Dynamic-index*, J_x as given in 2.42, values for \hat{z} (blue), \mathcal{R}_B (green), \mathcal{R}_C (red), and \mathcal{R}_n (yellow-*concealed by horizontal axis*) against $\log_{10} F$ for $\beta = 38.68 \text{ eV}^{-1}$ and F in the sampled experimental range. As constructed, the index is constrained to the $[0, 1]$ interval. The dynamic indexes for \mathcal{R}_B and \mathcal{R}_C are notable: \mathcal{R}_B for being the only one transitioning for this temperature run (from 0.2 at low F to 1.0 at high F), and \mathcal{R}_C for being transitional (index is 0.3, and no evolution occurs as fixed β implies a fixed \mathcal{R}_C). Since $\mathcal{R}_n \ll 1$, it appears close to the horizontal axis.

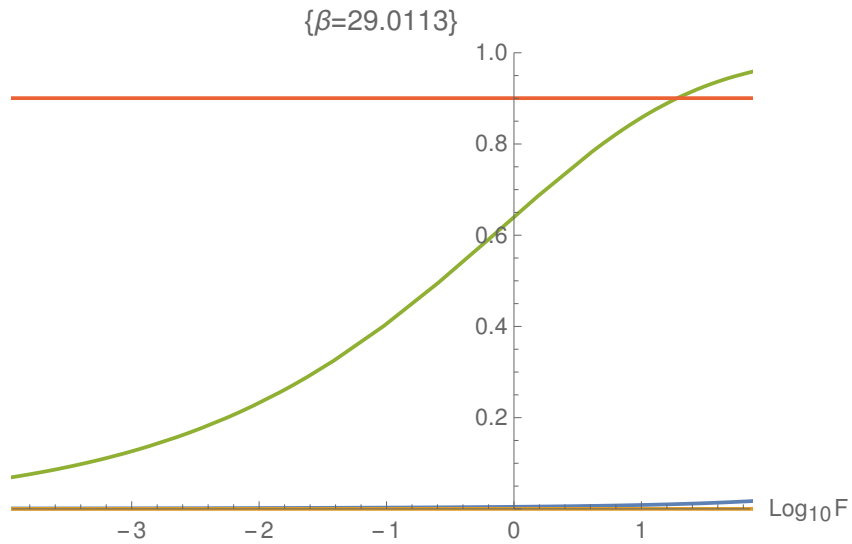


Figure 2.18: *Dynamic-index, J_x* as given in 2.42, values for \hat{z} (blue), \mathcal{R}_B (green), \mathcal{R}_C (red), and \mathcal{R}_n (yellow-*concealed by horizontal axis*) against $\log_{10} F$ for $\beta = 29.01 \text{ eV}^{-1}$ and F in the sampled experimental range. As constructed, the index is constrained to the $[0, 1]$ interval. The dynamic indexes for \mathcal{R}_B and \mathcal{R}_C are notable: \mathcal{R}_B for being the only one transitioning for this temperature run (from 0.1 at low F to 1.0 at high F), and \mathcal{R}_C for completely transitioning into the state D^{**1} . Since $\mathcal{R}_n \ll 1$, it appears close to the horizontal axis.

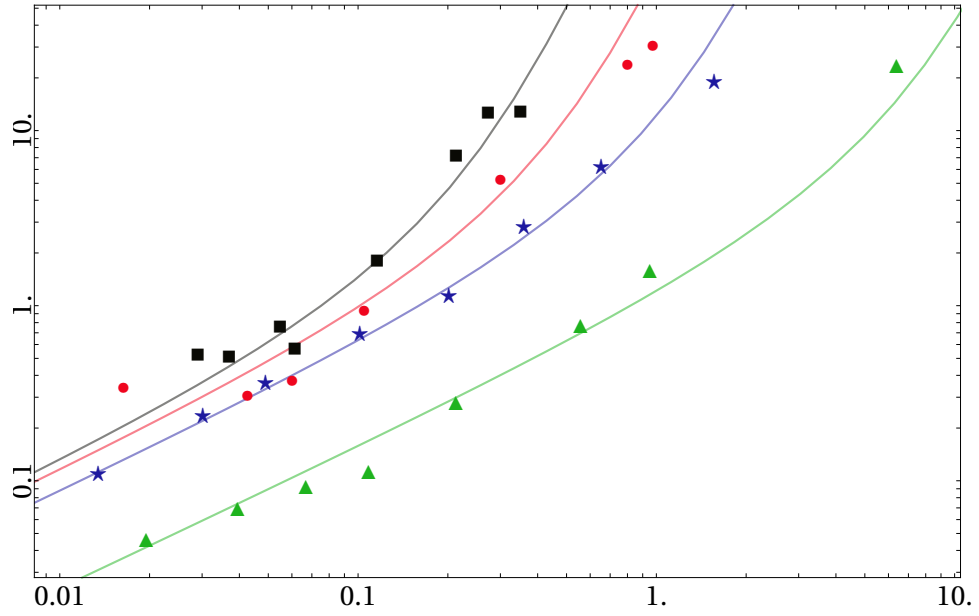


Figure 2.19: Island density vs. deposition rate F in the aggregation regime for 6P on sputter-modified mica (001) [57] at $T = 150\text{K}$ (*black*, square dots), 200K (*red*, round dots), 300K (*blue*, star dots), and 400K (*green*, triangular dots), with best-fit parameters: $i = 4$, $\log_{10} \mathcal{R}_n^0 = -5.57$, $\log_{10} \mathcal{R}_B^0 = 5.08$, $\log_{10} v\tau_0 [\mu\text{m}] = 2.54$, and, in eV, $E_D = 0.0170$, $E_{ph} = 0.0171$, and $E_b = 0.333$. The final effective coverage θ_{eff} is given by $\log_{10} (\theta_{\text{eff}}\tau_0^i [\mu\text{m}^{-2}\text{s}^i]) = -25.4$.

Summary and Conclusion

Our work has shown that non-thermal (high-energy) adsorption states have dramatic effects on monomer aggregation and island nucleation. A full solution for the model is constructed, along with a quantitative description of the effective growth exponent that can model transition regions. Additionally, a description of the effective activation energy is obtained, which leads to the discovery of 16 well-defined limiting regimes for the activation energy and 8 for the growth exponent. More importantly, we identify four dimensionless parameters that capture the limiting regions giving rise to said regimes, and we are able to imbue the parameters with physical interpretations. Importantly, an interpretation of the distribution of sub-critical islands leads to a physical description of the activation energy for the system.

Additionally, we provide an approximate treatment for the solution that can be more easily used to fit experimental systems. The approximation is robust enough to capture the general behavior of the growth exponent, and we can theoretically provide limits for the maximum errors due to the approximation. Also, we introduced a well-defined way to discuss transitional regions in the form of a dynamic-index: this allowed us to meaningfully discuss and label transitional regimes in a general sense. Specifically for [57], the dynamic-index formalism highlighted the effect monomer decay from unstable islands had on the system. That is, how the ballistic component of said decay could be the source of the non-monotonic (read anomalous) behavior in the growth exponent.

Finally, we fit our model to experimental data and managed to describe a truly superthermal system. Our description of states in terms of the activation energy allowed us to describe the different transitions occurring in the system, and test the robustness of the asymptotic approximation in a real setting.

Chapter 3: Atomic Scale: Symmetry-Breaking

Introduction

Since the publication of the seminal work on graphene [21], the material has been an experimental and theoretical workhorse for both physicists and chemists. Of the many remarkable features of the material, the presence of Dirac cones in the electronic band structure is particularly relevant to electronic and transport properties. Theoretical descriptions of graphene, most notably tight-binding approximations, have been a staple of electronic analysis for decades [58]. These descriptions have demonstrated that the delicate nature of the Dirac cones can easily be perturbed to give rise to gaps in the band structure of graphene. In an engineering sense, it is this electromagnetic structure that makes graphene such an attractive candidate for the construction of devices, due to the presence of a *gapped*, i.e. zero current, state.

Specifically, graphene can be described as having a *honeycomb* structure, i.e., a hexagonal Bravais lattice with a 2-atom basis. Equivalently, one can consider graphene as occupying two of the three possible distinct sites in a triangular lattice (see Fig. 3.1).

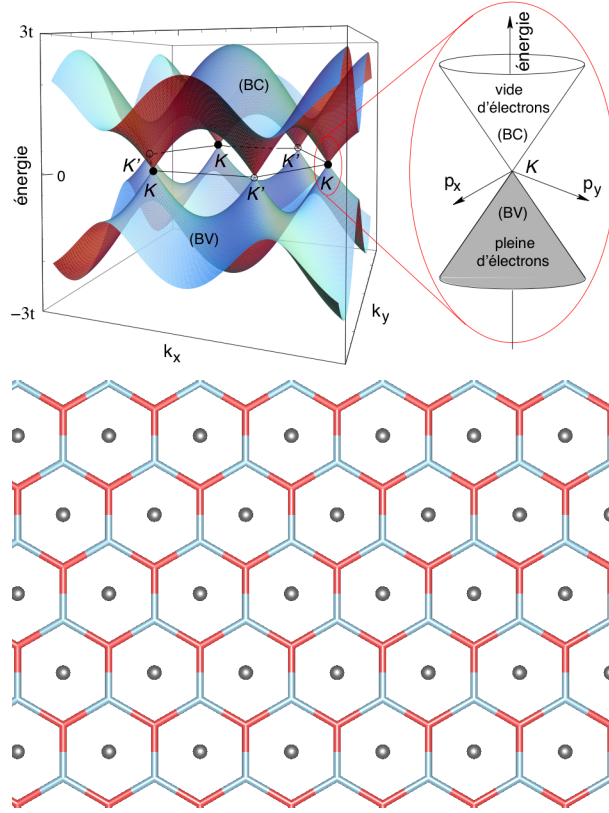


Figure 3.1: **Top)** The electronic structure of graphene: note that the conduction band (BC as in *bande de conduction*) and the valence band (BV as in *bande de valence*) are separated at the K (Dirac point) and K' points in reciprocal space. The local structure at the Dirac point, i.e. the Dirac cone, is responsible for the semimetal nature of graphene as a single point separates the hole band (*vide d'électrons*) from the electron band (*pleine d'électrons*) [59]. **Bottom)** Schematic of single layer graphene (SLG) as a subset of a triangular lattice. Sublattices S_1 (red sites) and S_2 (blue sites) represent the two carbon atoms that constitute the smallest supercell of infinitely periodic graphene, while sublattice S_3 (black dot) marks the hollow sites (honeycomb) in graphene. Note that there are no C atoms in S_3 , but the marker is included to stress the unoccupied site in the triangular lattice, useful when considering symmetry-breaking effects.

Since there is no mechanism differentiating between the two sublattices, there is an intrinsic sublattice symmetry for the system (graphene remains invariant under non-trivial translations and rotations, i.e. the D_6 point group in Schoenflies notation). By differentiating one of the sublattices and breaking the symmetry, it is possible to obtain the coveted gaps in the band structure. This approach has proven effective for adsorbates on graphene, namely a pseudo-commensurate hexagonal boron nitride (h-BN) adsorbate on SLG (single layer graphene) [60]. In the h-BN system, the graphene substrate's sublattices are differentiated by the application of a C–N bond with one sublattice, and C–B bond with the other one, opening a gap of 53meV (see Fig. 3.2). While the results are impressive [60], and have been confirmed experimentally [61], there are concerns regarding the lattice mismatch of 2% in h-BN: since we expect small changes to the band structure, the possibility of shearing effects being mistaken for symmetry-breaking ones motivates finding an adsorbate that is commensurate with graphene.

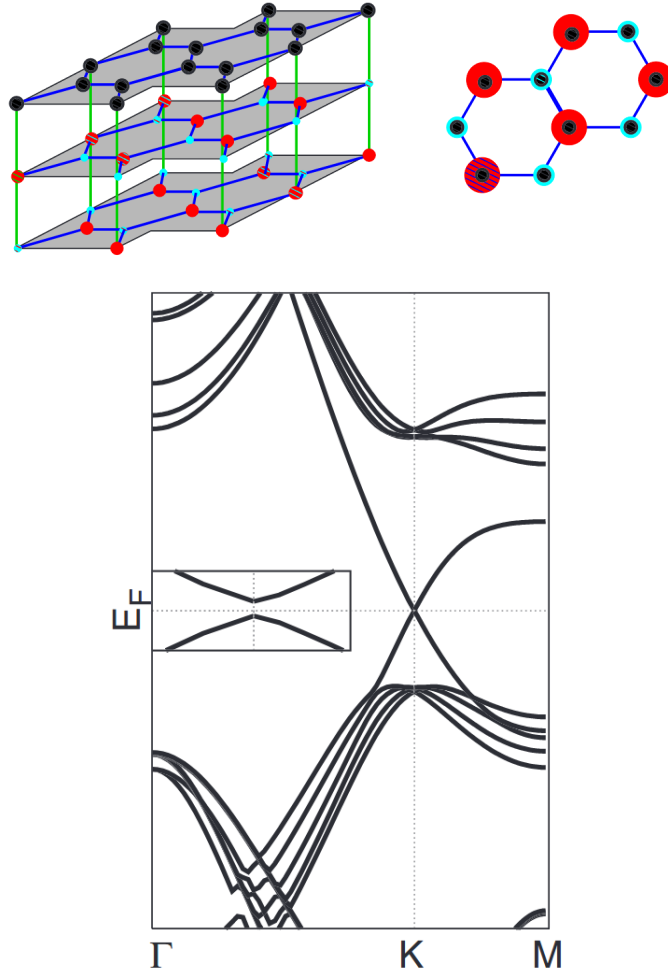


Figure 3.2: **Top)** Differentiation of graphene substrate's sublattices by application of a hexagonal boron nitride adsorbate (hBN). In this case, the C–N bond with one sublattice, and C–B bond with the other one create the required effective potential [60]. **Bottom)** Calculated band structure from DFT calculations on the graphene-hBN system. Note the gap at the K point of 53.0 meV [60].

One of our earlier attempts was the study of trimesic acid (TMA) overlayers on SLG [62]. Trimesic acid, atomic formula $C_6H_3(CO_2H)_3$, is a massive molecule (by physics standards with an atomic weight of $210.14\mathbf{u}$ for a single TMA molecule compared with the atomic weight for the smallest graphene supercell of $24.02\mathbf{u}$) consisting of a benzene ring with three attached carboxyl groups. Promising features of TMA include the molecule being commensurate with graphene because of the presence of a central benzene ring, and having the capability to induce an effective potential through the action of a carboxyl group. Furthermore, TMA has a tendency to arrange in overlayers, notably a honeycomb-like overlayer commensurate with a (7×7) graphene supercell. In this particular case, there were two unique configurations for the TMA honeycomb overlayer, one in which the carboxyl groups affect both graphene sublattices equally (non-symmetry-breaking), and another in which the groups affect them differently (symmetry-breaking). Using VASP 5.3.3, with ab initio van der Waals density functionals (vdW-DF), we computed through DFT calculations that the symmetry-breaking overlayer opened a gap of 15.3 meV , contrary to the non-symmetry-breaking overlayer that preserved the Dirac point (see Fig. 3.3).

Though initial results were promising, we ran into several complications that made the system less auspicious for study. First, despite the overlayers being commensurate with graphene, supercell size led to prohibitive computational issues: the smallest supercell containing 2 TMA molecules consisted of 140 separate atoms and a large 12\AA vacuum. Of even greater concern were the supercells for TMA on BLG (bilayer graphene) and TLG (trilayer graphene), with atom counts of 238 and 336

atoms, respectively. Furthermore, as supercell sizes increased from 4645 \AA^3 in SLG, to 5420 \AA^3 in BLG, and 6194 \AA^3 in TLG, the computational cost incurred by the non-local van der Waals functionals became prohibitive; that is even before making considerations for even larger supercells in order to account for changes in coverage.

In response, and inspired by local experimental results [63], we explore CF_3Cl overlayers on SLG and BLG graphene via DFT calculations. As supercell sizes are commensurate and more manageable than those in TMA, we are able to explore the effects of orientation, and coverage on the electronic structure of graphene. Ultimately, we observe gaps in the band structure, and attribute the modifications in the electronic properties of graphene to symmetry-breaking effects by eliminating the possibility of shearing effects being responsible for them.

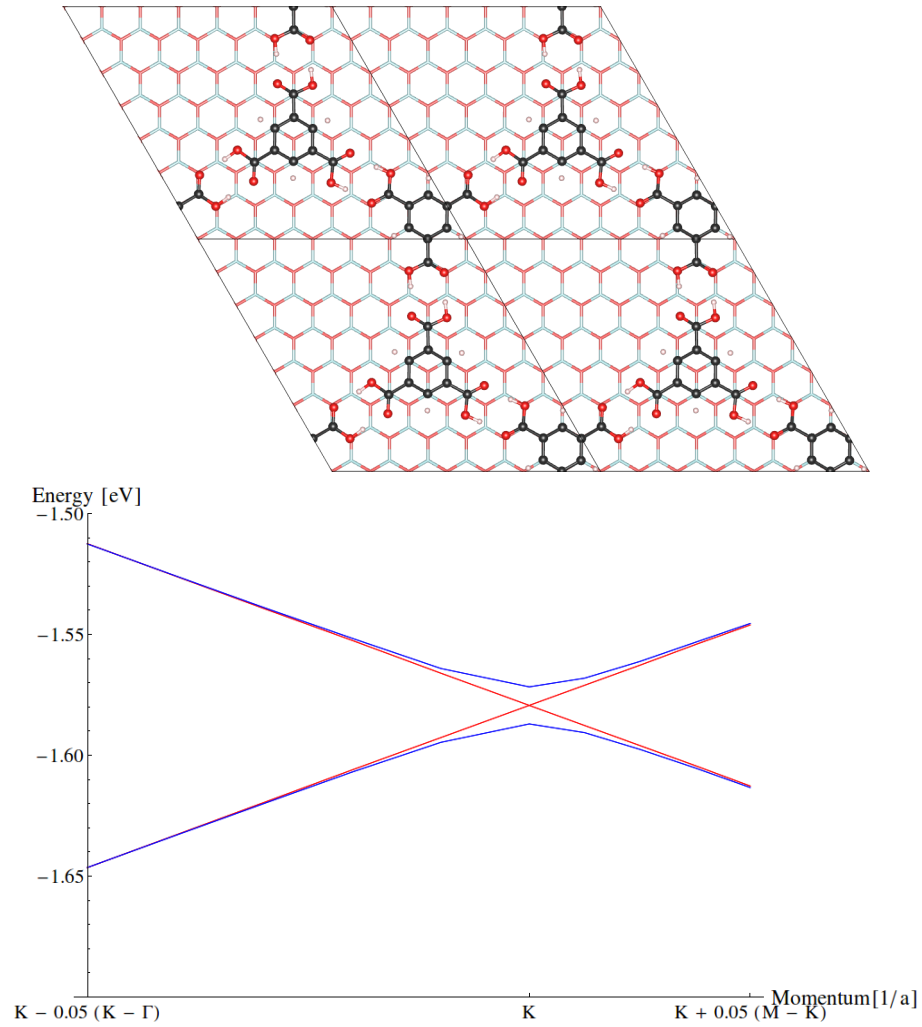


Figure 3.3: **Top)** Supercell for TMA overlayers in SLG; note the graphene supercell is (7×7) with 2 TMA molecules per cell [62]. **Bottom)** Calculated band structure of SLG with TMA adsorbate. Note the gap at the K point of 15.3 meV [62].

Tight-Binding Considerations

Tight-binding considerations for SLG are not a recent development [58], but they remain relevant despite their deceptive simplicity due to their flexibility and adaptability to extension. Since simple shearing deformations parallel to a periodic SLG sheet can induce gap openings [64], we model the effects of these deformations on the band structure along with those of the effective potential using tight-binding calculations. Since the presence of CF_3Cl molecules is liable to induce both parallel and perpendicular components of shearing to the graphene substrate, previous tight-binding results [64] need to be extended in order to account for deformation along the SLG plane and its normal. First, consider the fundamental lattice vectors:

$$\vec{a}_1 = a \left(\cos \frac{\pi}{6} \hat{x} + \sin \frac{\pi}{6} \hat{y} \right) \quad \vec{a}_2 = a \left(\cos \frac{\pi}{6} \hat{x} - \sin \frac{\pi}{6} \hat{y} \right) \quad \vec{a}_3 = -L \hat{z} \quad (3.1)$$

where a refers to the C–C bond length for an undisturbed SLG lattice, $L > a$ is a distance large enough to minimize adsorbate-adsorbate interactions across the void, and $(\hat{x}, \hat{y}, \hat{z})$ are the standard Cartesian unit vectors. Second, consider the symmetric shearing tensor:

$$\vec{x}^S = \begin{pmatrix} 1 & \epsilon_{12} & \epsilon_{13} \\ \epsilon_{12} & 1 & \epsilon_{23} \\ \epsilon_{13} & \epsilon_{23} & 1 \end{pmatrix} \vec{x} \quad (3.2)$$

where \vec{x}^S is the *sheared* position vector obtained by applying the symmetric deformation on the original position vector \vec{x} , and ϵ_{**} are dimensionless shearing coefficients. Additionally, consider symmetry-breaking through the addition of two effective potentials on the sublattices in the form of energies δ_1 and δ_2 . Therefore, the tight-binding Hamiltonian for the system is given by:

$$H(\vec{k}) = \begin{pmatrix} \delta_1 & V_{\text{pp}\pi} f(\vec{k}) \\ V_{\text{pp}\pi} f(\vec{k})^* & \delta_2 \end{pmatrix} \quad \text{with,} \quad (3.3)$$

$$f(\vec{k}) = \sum_{n=1}^3 \exp(i\vec{a}_n^S \cdot \vec{k}) \quad (3.4)$$

Note that $f(\vec{k})$ encodes the pp π *nearest neighbor* interactions, with the shearing effects present in the rescaling of the lattice vectors, while $V_{\text{pp}\pi}$ is found through fitting (see section 3.5). Having defined the lattice vectors for the system (3.1), the reciprocal lattice (k -space lattice) lattice is given by:

$$\vec{k}_1 = 2\pi \frac{\vec{a}_2 \times \vec{a}_3}{\vec{a}_1 \cdot (\vec{a}_2 \times \vec{a}_3)} = \frac{2\pi}{a} \left(\frac{1}{\sqrt{3}} \hat{x} + \hat{y} \right) \quad (3.5)$$

$$\vec{k}_2 = 2\pi \frac{\vec{a}_3 \times \vec{a}_1}{\vec{a}_2 \cdot (\vec{a}_3 \times \vec{a}_1)} = \frac{2\pi}{a} \left(\frac{1}{\sqrt{3}} \hat{x} - \hat{y} \right) \quad (3.6)$$

$$\vec{k}_3 = 2\pi \frac{\vec{a}_1 \times \vec{a}_2}{\vec{a}_3 \cdot (\vec{a}_1 \times \vec{a}_2)} = -\frac{2\pi}{L} \hat{z} \quad (3.7)$$

In SLG any gap should open at the K point (Dirac point), $K = \frac{1}{3}\vec{k}_1 - \frac{1}{3}\vec{k}_2$, thus, for small substrate deformations:

$$f(K) = \lim_{\vec{k} \rightarrow K} f(\vec{k}) = -\frac{2\pi i}{\sqrt{3}} \left(\epsilon_{12} + \frac{2L}{\sqrt{3}a} \epsilon_{23} \right) + \mathcal{O}(\epsilon_{12}^2) + \mathcal{O}(\epsilon_{23}^2) \quad (3.8)$$

to first order in ϵ_{**} . Having obtained a linear dependence for the *nearest neighbor* interactions, consider the tight-binding Hamiltonian at the Dirac point:

$$H(K) = \begin{pmatrix} \delta_1 & -V_{\text{pp}\pi} \frac{2\pi i}{\sqrt{3}} \left(\epsilon_{12} + \frac{2L}{\sqrt{3}a} \epsilon_{23} \right) \\ V_{\text{pp}\pi} \frac{2\pi i}{\sqrt{3}} \left(\epsilon_{12} + \frac{2L}{\sqrt{3}a} \epsilon_{23} \right) & \delta_2 \end{pmatrix} \quad \text{with, (3.9)}$$

$$E_{\text{gap}} = \sqrt{V_{\text{eff}}^2 + V_{\text{shear}}^2} \quad (3.10)$$

$$V_{\text{eff}} = |\delta_1 - \delta_2| \quad (3.11)$$

$$V_{\text{shear}} = \frac{4\pi}{\sqrt{3}} |V_{\text{pp}\pi}| \left| \epsilon_{12} + \frac{2L}{\sqrt{3}a} \epsilon_{23} \right| \quad (3.12)$$

where E_{gap} is the gap in the band structure at the Dirac point, V_{eff} and V_{shear} are the energy contributions to the gap by symmetry-breaking and shearing, respectively. After obtaining $V_{\text{pp}\pi}$ from the band structure, and ϵ_{**} from direct calculations of the graphene substrate's deformation, we can isolate the net effect of symmetry-breaking on gap opening.

A final consideration should be given to SLG tight-binding calculations for supercells larger than (1×1) . In such cases, as the lattice vectors increase in size, the reciprocal vectors are compressed by the same factor. This causes a *folding in* of the band structure. Equivalently, tight-binding calculations on (2×2) cells (discussed below) would imply solving a 8×8 tight-binding Hamiltonian, whereas $(\sqrt{3} \times \sqrt{3})$ would imply solving a 18×18 tight-binding Hamiltonian. For weakly bound systems, and small dispersions, we approximate the band structure of these extended supercells through the obtained SLG results as a way to quantify the effective potential for differently sized systems.

Supercell Construction

In order to perform DFT calculations, proper supercells must be constructed. Our decision to use CF_3Cl as the adsorbate on graphene comes after methodical deliberation. First, the molecule is tetrahedral with 3 F atoms forming a triangular *base*, 1 Cl atom at the *cusp* and a C atom at its center (see Fig. 3.4). Experimentally [63], the small size of CF_3Cl adsorbates in BLG along with the presence of various phases that modify the electronic structure of graphene, make CF_3Cl a promising candidate for symmetry-breaking effects. Specifically, three phases exhibit interesting physical properties, namely, the *E phase*, the *IC phase* and the *C phase*.

The *E phase* presents electrical ordering of the molecules, and can be described by a supercell of 4 CF_3Cl molecules. However, in this phase the $\text{C}-\text{Cl}$ bond in CF_3Cl presents parallel and perpendicular components to the normal of the graphene substrate, causing potentially large deformation effects in graphene. Moreover, even if the deformations are found to be small, the basic supercell would be $(8\times 2)_2$, where $(1\times 1)_2$ refers to the smallest supercell that can generate a periodic BLG lattice. Thus, for the study of weak symmetry-breaking effects, the *E phase* is both computationally expensive and potentially too intrusive on the substrate.

The *IC phase* has similar orientation problems as the *E phase*, with the additional complication that CF_3Cl molecules are randomly oriented. While a supercell commensurate with (1×1) cannot be constructed for the *IC phase*, and DFT calculations have been performed on disordered systems [65], the usual prescription is to

account for disorder using large supercells, discouraging modeling the *IC phase* under our considerations. Experimentally, changes in the transport properties of BLG are largely attributed to surface potentials variations from the film and dielectric screening from the adsorbate in the case of the *E phase* and *IC phase*, respectively, and not to gap opening. Hence, disregarding these phases as candidates for our symmetry-breaking studies seems sensible.

Finally, the *C phase* presents several convenient characteristics. First, the C–Cl bond is parallel to the normal of the graphene substrate; second, the size of the F₃ tetrahedron projected onto the graphene surface is commensurate with a single graphene honeycomb. Third, experimentally, it is only in the case of the *C phase* that the opening of a band gap has been suggested as a dominant effect. Thus, we study variations on coverage and orientation of CF₃Cl molecules in the *C phase*, but begin our discussion working on SLG rather than BLG.

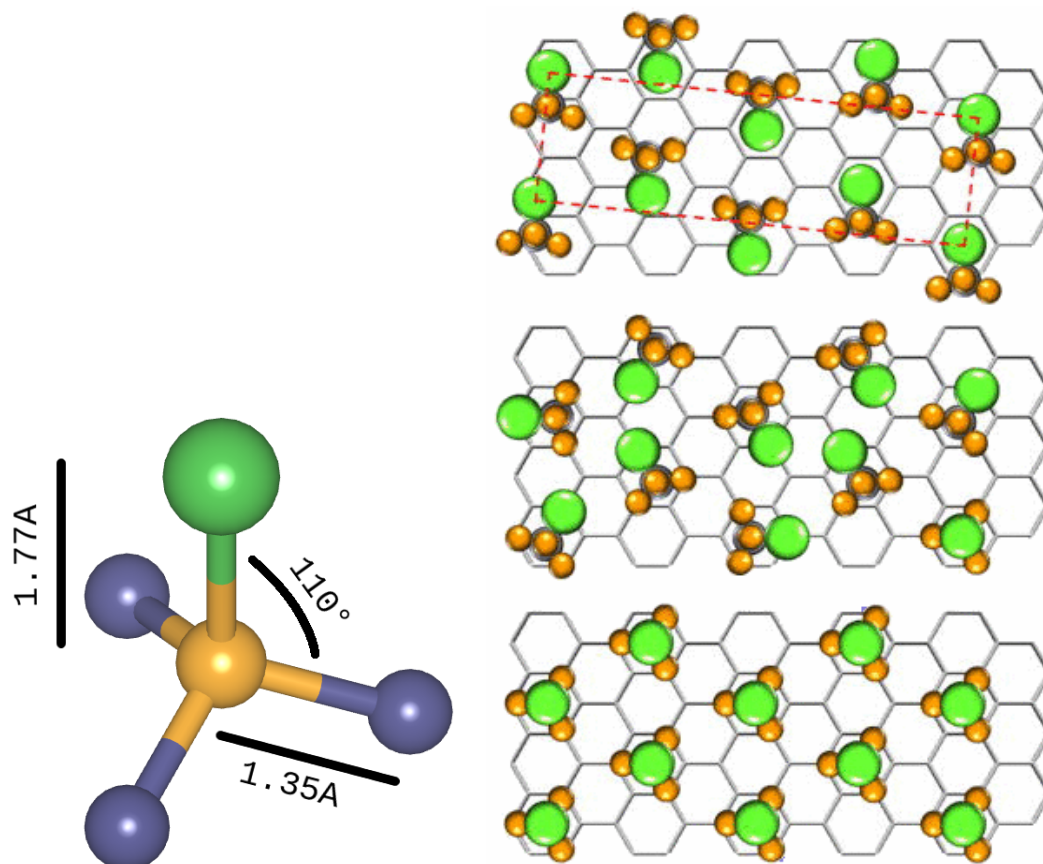


Figure 3.4: **Left)** *Ball-and-stick* model for a single CF₃Cl molecule. The C atom (yellow) connects the tetrahedral base made up of 3 F atoms (purple) to a cusp consisting of 1 Cl atom (green). Molecule dimensions are representative and calculated using optB86b-vdW. **Right)** Experimental phases of CF₃Cl on BLG [63]: **Right, Top)** ordered *E Phase* with CF₃Cl non-perpendicular to graphene surface, **Right, Middle)** disordered *IC Phase* with CF₃Cl non-perpendicular to graphene surface, and **Right, Bottom)** ordered *C Phase* with CF₃Cl perpendicular to graphene surface.

We can explore supercells as small as (2×2) (containing 1 CF_3Cl molecule) and $(\sqrt{3}\times\sqrt{3})$ (containing 3 CF_3Cl molecules), where (1×1) denotes the simplest supercell that can generate a periodic SLG lattice. Note that (2×2) corresponds to a known submonolayer arrangement for the *C phase*, and $(\sqrt{3}\times\sqrt{3})$ is a natural extension of this supercell to a larger coverage. Exploration of higher coverage supercells indicates that $(\sqrt{3}\times\sqrt{3})$ is the maximal coverage for molecules in the *C phase*, as no DFT calculations with CF_3Cl molecules for coverages higher than $(\sqrt{3}\times\sqrt{3})$ were found to converge either in maximal atomic forces per atom, nor total cell pressure. Hence, $(\sqrt{3}\times\sqrt{3})$ and (2×2) represent 1.00ML and 0.75ML coverage, respectively (see Figs. 3.5 and 3.6 for an illustration of the coverage).

While the coverage is experimentally accessible, the orientation of the molecules is not; hence, a complete accounting of all orientations is necessary for an understanding of any symmetry-breaking effects. Recall that graphene consists of two occupied sublattices (S_1 and S_2), and a hollow site (S_3). Thus, consider all possible orientations of CF_3Cl molecules on the *C phase*, where we take the approach of identification through nomenclature. First, when the C-atom is located above an occupied site (S_1 or S_2), we denote the orientation as C^* , whereas the C-atom located above the unoccupied site (hollow S_3) would be denoted by H^* . Second, rotations about the C-Cl bond leave two possible orientations: when the F atoms eclipse occupied sites (S_1 or S_2), the orientation is referred as $^*\text{E}$; and when the F atoms are otherwise staggered, the orientation is referred as $^*\text{S}$. All possible orientations are illustrated in Fig. 3.7, with the connecting transformations presented in Table 3.1.

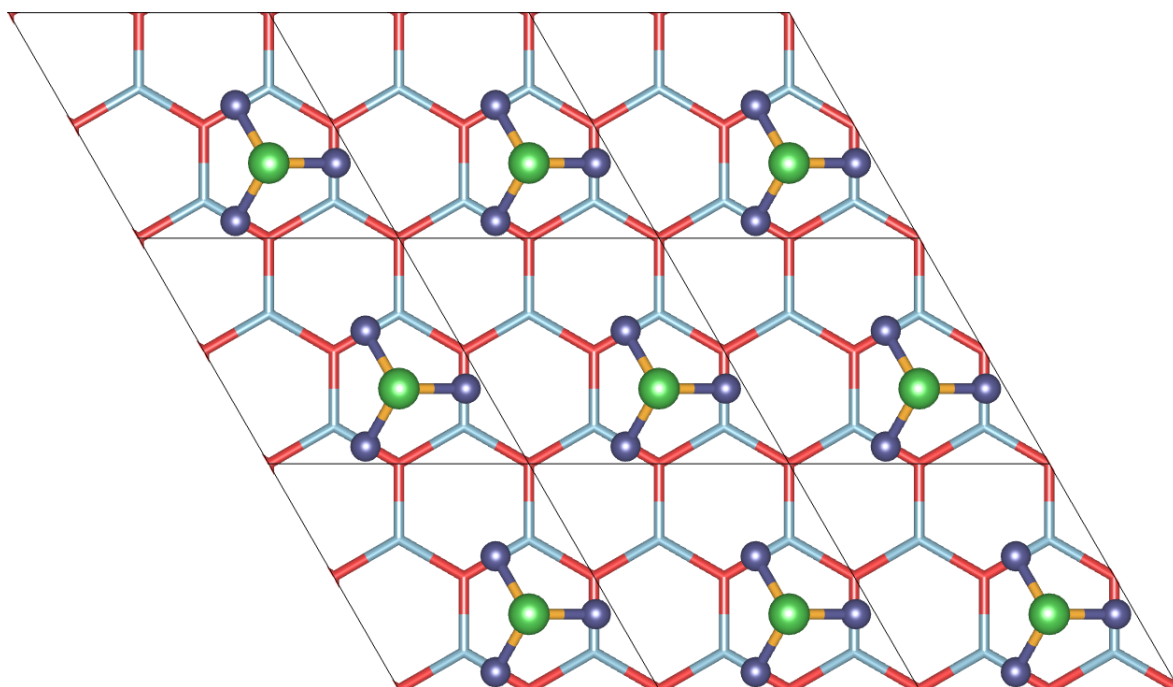


Figure 3.5: Sample supercells of coverage (2×2) , with orientation HS (C atom in hollow, with staggered F atoms). Shown are $3 \times 3 = 9$ instances of a (2×2) supercell, where a (2×2) supercell contains 1 CF_3Cl molecule.

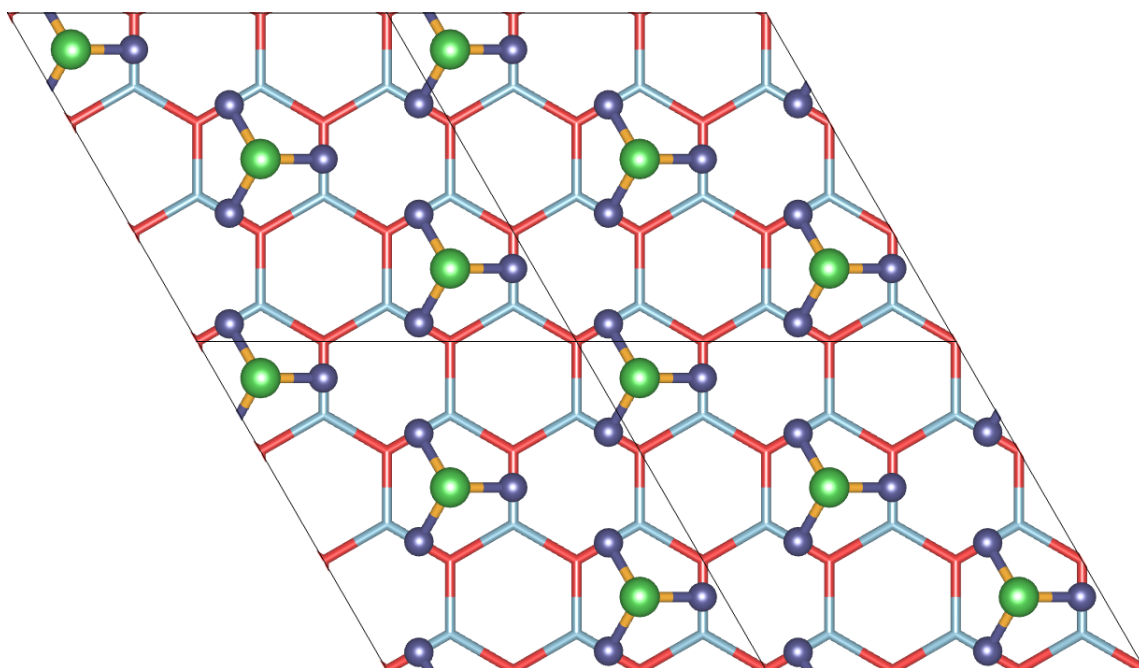


Figure 3.6: Sample supercells of coverage $(\sqrt{3} \times \sqrt{3})$, with orientation HS (C atom in hollow, with staggered F atoms). Shown are $2 \times 2 = 4$ instances of a $(\sqrt{3} \times \sqrt{3})$ supercell, where a $(\sqrt{3} \times \sqrt{3})$ supercell contains 3 CF_3Cl molecules.

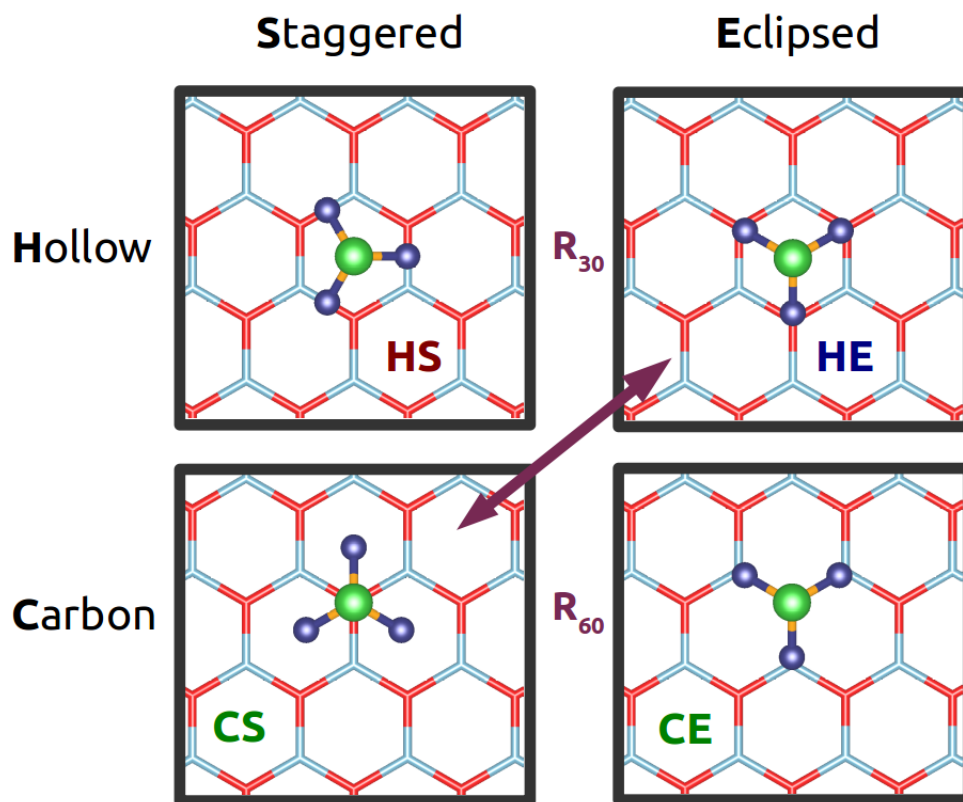


Figure 3.7: All four possible orientations of CF_3Cl molecules in the C phase. The graphene sublattices S_1 and S_2 are stylized as line bonds (red and blue). In H^* orientations the CF_3Cl molecule sits on a honeycomb hollow, while in C^* orientations it sits on an occupied graphene sublattice. For the F atoms, the eclipsed orientations ($^*\text{E}$) refer to F atoms eclipsing an occupied sublattice, while the staggered orientations ($^*\text{S}$) do otherwise.

	HS	HE	CS	CE
HS	\sim	-30°	$(0, -1), 30^\circ$	$(0, -1), -30^\circ$
HE	30°	\sim	$-60^\circ, (1, 0)$	$(0, -1)$
CS	$-30^\circ, (0, 1)$	$(-1, 0), 60^\circ$	\sim	60°
CE	$30^\circ, (0, 1)$	$(0, 1)$	-60°	\sim

Table 3.1: The transformations required to convert an orientation in the first column into an orientation in the first row for CF_3Cl molecules in the C phase. For the transformations, positive numbers, e.g. 30° , refer to a clockwise rotation by an amount in degrees (and a negative number to a counter-clockwise rotation); while, ordered pairs, e.g. $(1, 0)$, refer to translations by the lattice vectors \vec{a}_1 , and \vec{a}_2 (as defined in Eqn. 3.1). If two transformations are present, then the left-to-right order indicates the order of application.

DFT Considerations

Calculations were performed with VASP 5.3.3, using grid resources at the Texas Advanced Computing Center at the University of Texas at Austin (TACC) [66], and a similar prescription as for other systems with sensitive substrates [67]. A large energy cutoff for the wave functions (of 600eV) is necessary to account for surface effects. Most importantly, supercells are constructed with a large vacuum of 18Å, along with (up to) electric quadrupole corrections, to capture sensitive effects in the band structure of graphene. A technique to bypass dipole corrections is to add a second adsorbate layer on an additional substrate slab [68]. However, for SLG and BLG there would be strong interactions between adsorbates in the opposite side of the vacuum, so we opt not to take this bypassing approach.

As we explore differently sized supercells, it is of great concern to make the k -point meshes between supercells commensurate. As seen in similar systems [67], when dealing with a large supercell, a *folding* mechanism occurs for the reciprocal space: namely, k -meshes become denser by the same factor that the lattice vectors are augmented. Though reciprocal vectors in (2×2) and $(\sqrt{3}\times\sqrt{3})$ have to be carefully analyzed to account for *folding*, the silver lining is an overall denser effective k -point mesh. We employ k -point meshes of $17\times 17\times 1$ and $13\times 13\times 1$, for (2×2) and $(\sqrt{3}\times\sqrt{3})$, which lead to effective k -point meshes of $34\times 34\times 1$ and $39\times 39\times 1$, respectively. The large k -point density and similar sizes, justifies energy comparisons between both supercells, even though they do not present similar physical sizes. Lastly, k -point convergence is achieved when iterations between steps differs by less

than 0.01 meV; which sets our least significant energy in the study.

Finally, we consider the inclusion of van der Waals potentials in our DFT calculations. The accuracy [69], implementation in arbitrary geometries [70], and overall efficient implementation of the potentials [71] has been extensively studied. Without such potentials, we could not find a stable, i.e. hardly any binding, *C-phase* supercell, which suggests the symmetry-breaking effect could depend on the implementation of the approximation. To that effect, we perform our calculations with four different van der Waals implementations, in order to confirm that any observed results are physical, and not just DFT artifacts. We employ several potentials: optB86b-vdW1 as it targets large-gradient behavior (of note is its modeling of Cl and F) [70], the exchange optimized optPBE and optB88 potentials [72] aimed at improving on the original revPBE, and having better chemical accuracy with the S22 data set (mostly biological dimers, of which C-C is of particular importance to us), and the enhanced rPW86 potential [73], which through a finer semilocal exchange functional and the use of asymptotic gradient corrections better predicts binding energy, equilibrium separation, and potential-energy on the S22 data set. These potentials are useful when describing most relevant features, though they are not without problems (notably they do not capture hybridization properly and some of the earlier ones have problems with asymptotic effects) [74].

Listing all these implementations of vdW potentials can obscure their ultimate goal: by employing a combination of semi-local and non-local correlation functionals, along with the classic revPBE exchange functional, vdW-DF1 (and correlation-energy-corrected vdW-dF2) are a good starting point for the description of general

matter [75]. Though the formalism is not without shortcomings (e.g. overestimating binding separations), the accounting of weakly covalent systems is crucial to our description of adsorbates on a carbon-based substrate such as graphene. There have been efforts to improve the potentials: some attempts take the view of adding empirical corrections by fitting to real systems (such as rev-vdW-DF2 or vdW-DF2-B86R) [76–78], while others focus on a first principles description by improving (or replacing) revPBE with another exchange functional (such as vdW-DF-cx0 and vdW-DF2-0) [79, 80].

Symmetry-Breaking Effects

Having obtained converged DFT calculations on all orientations (and potentials), we compute the *adsorption energy*, E_{ads} , of the CF_3Cl adsorbate:

$$E_{\text{ads}} = E_{\text{Freon}}^{\text{bulk}} + E_{\text{Graphene}}^{\text{bulk}} - E_{\text{total}}^{\text{bulk}} \quad (3.13)$$

where E_{ads} is in units of energy per CF_3Cl molecule, $E_{\text{Freon}}^{\text{bulk}}$ is the free energy of the *frozen* (i.e. not relaxed) CF_3Cl overlayer, $E_{\text{Graphene}}^{\text{bulk}}$ is the free energy of the *frozen* graphene substrate, and $E_{\text{total}}^{\text{bulk}}$ is the total free energy of the converged system. Inspection of the adsorption energy for all vdW1 potentials reveals that optB86b, optB88 and optPBE predict an adsorption energy per molecule of approximately 280meV. Notably, coverage and orientation seem to have no meaningful effect on the adsorption energy of the CF_3Cl adsorbate (see Figs. 3.8 - 3.10). Similarly, the rPW86-vdW2 potential predicts an adsorption energy of around 220meV with the same insensitivity to coverage and orientation (see Fig. 3.11). The system can be regarded as physisorbed (adsorption energy of 200meV per molecule), with little sensitivity to coverage and orientation.

We also consider whether potentials exhibit different physics for different orientations. When the *adsorption energies* of every orientation are plotted against coverage, a consistent energetic hierarchy of vdW potentials arises (see Figs. 3.12 - 3.15). Based on the consistency of the adsorption results, we regard optB86b to be representative for the physics in the system. For every orientation, the gap (if any)

should open at the *folded* Dirac point, and the effective $V_{pp\pi}$ can be obtained from band structure results at $\vec{k} = 0$ for (2×2) and $\vec{k} = M = \frac{1}{2}\vec{k}_1$ for $(\sqrt{3}\times\sqrt{3})$ (as these points are invariant under *folding*). Contrary to SLG, where $V_{pp\pi}$ is interpreted as the interaction energy between *nearest neighbors*, in these folded systems it should be regarded as an *effective nearest neighbor* interaction. To illustrate, in (1×1) SLG there is a single instance of S_1 and S_2 atoms, so $V_{pp\pi}$ is truly the *nearest neighbor* interaction. However, in (2×2) SLG there are four instances of S_1 and S_2 atoms, so a (1×1) interpretation of the (2×2) supercell aggregates these effects into an *effective* $V_{pp\pi}$. Despite this new physical interpretation, $V_{pp\pi}$ results allow us to compute the shearing and *effective potential* contributions to the band gap according to our tight-binding model.

We also obtain gaps for *pristine graphene* lattices, which correspond to band structures of the SLG substrate when the CF_3Cl adsorbate is removed (though leaving the deformations). These systems are mechanically deformed into an excited state, so the interpretation of any gaps is qualitative at best. However, these *pristine graphene* lattices do provide insight into the magnitude of the deformations, where similar *pristine graphene* gaps imply similar deformation effects.

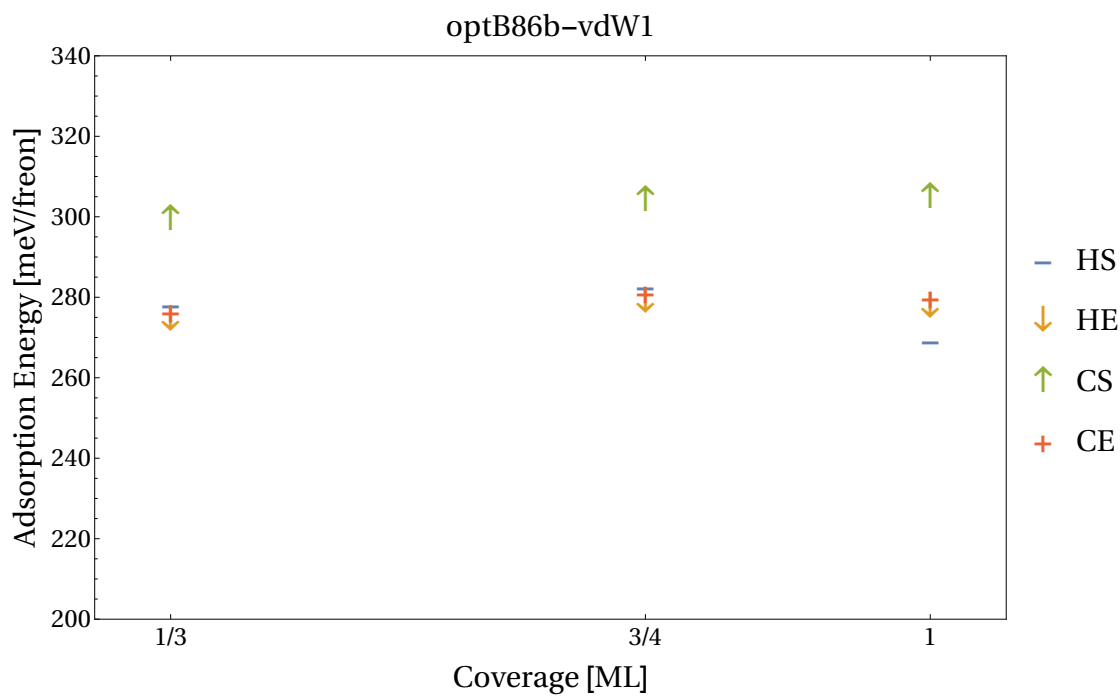


Figure 3.8: Adsorption energy for CF_3Cl adsorbates on graphene in units of energy per CF_3Cl molecule, as computed via DFT calculations using the optB86b-vdW1 implementation of van der Waals interactions. For every possible orientation, adsorption energy is plotted against coverage: notably, though adsorption energy changes depending on orientation, it remains insensitive to coverage.

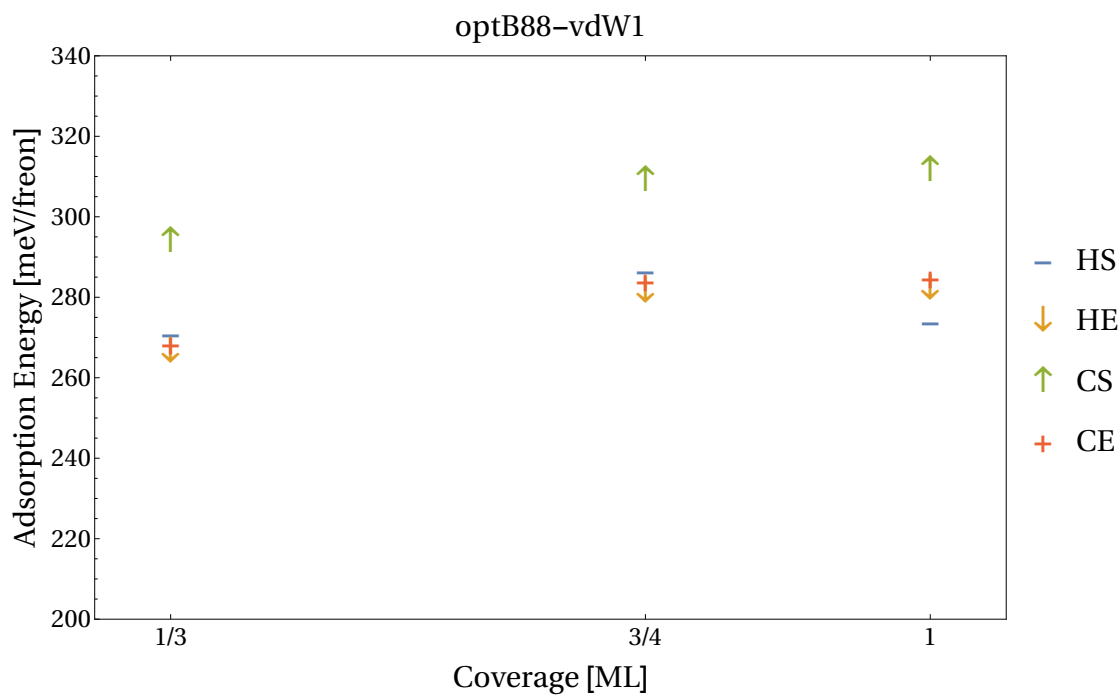


Figure 3.9: Adsorption energy for CF_3Cl adsorbates on graphene in units of energy per CF_3Cl molecule, as computed via DFT calculations using the optB88-vdW1 implementation of van der Waals interactions. For every possible orientation, adsorption energy is plotted against coverage: notably, though adsorption energy changes depending on orientation, it remains insensitive to coverage.

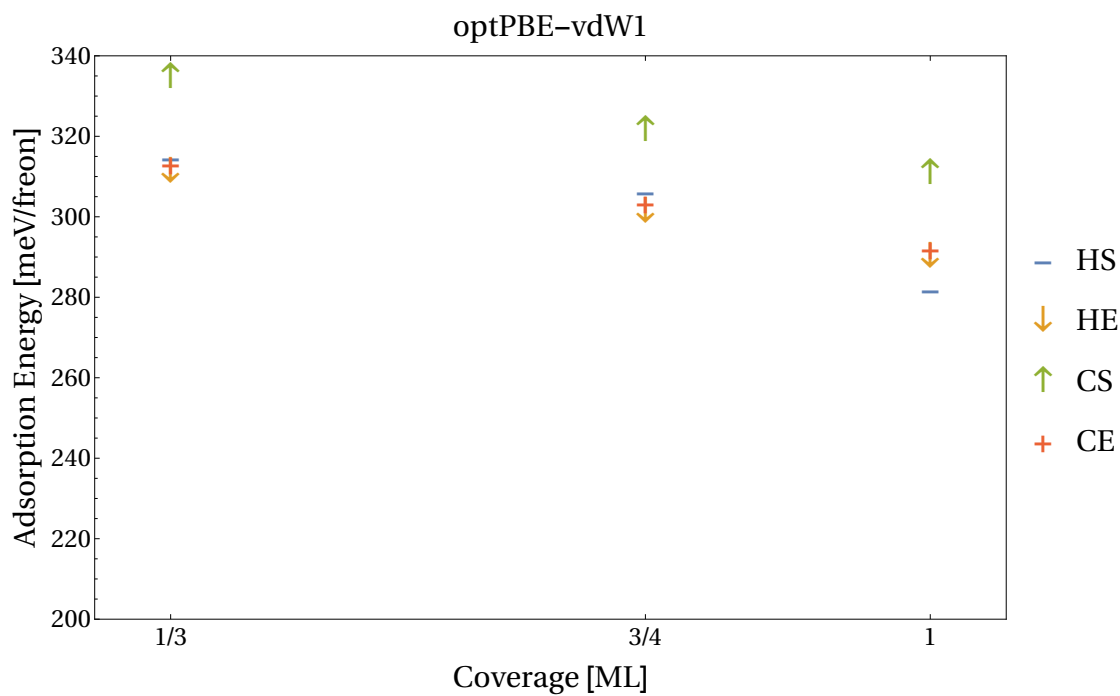


Figure 3.10: Adsorption energy for CF_3Cl adsorbates on graphene in units of energy per CF_3Cl molecule, as computed via DFT calculations using the optPBE-vdW1 implementation of van der Waals interactions. For every possible orientation, adsorption energy is plotted against coverage: notably, though adsorption energy changes depending on orientation, it remains insensitive to coverage.

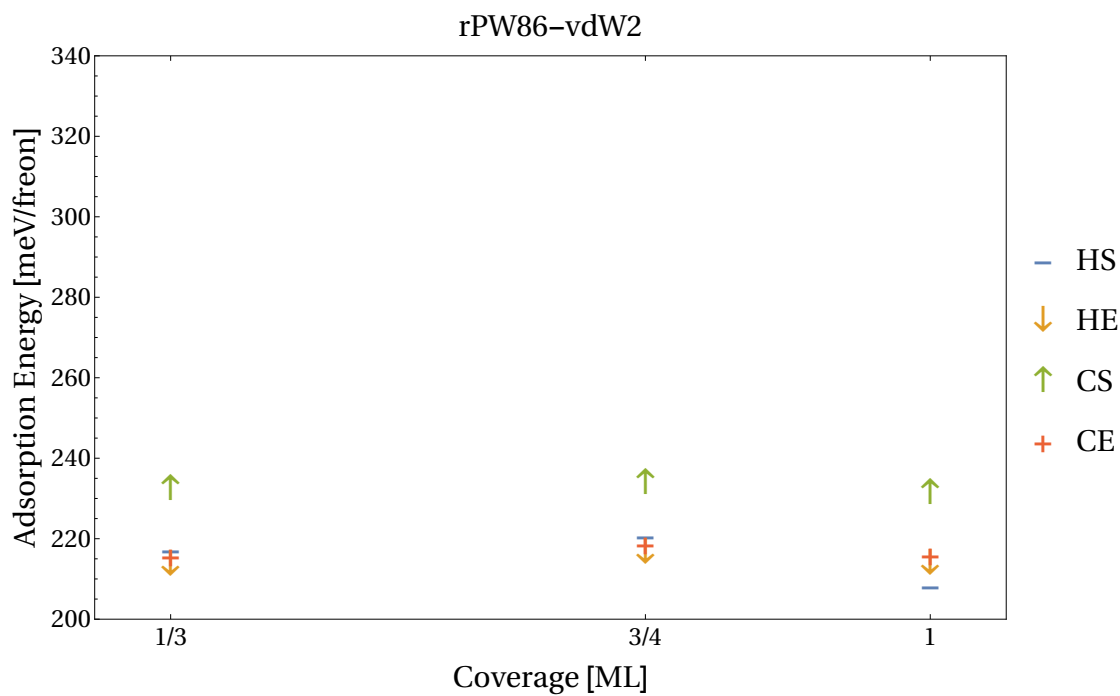


Figure 3.11: Adsorption energy for CF_3Cl adsorbates on graphene in units of energy per CF_3Cl molecule, as computed via DFT calculations using the rPW86-vdW2 implementation of van der Waals interactions. For every possible orientation, adsorption energy is plotted against coverage: notably, though adsorption energy changes depending on orientation, it remains insensitive to coverage.

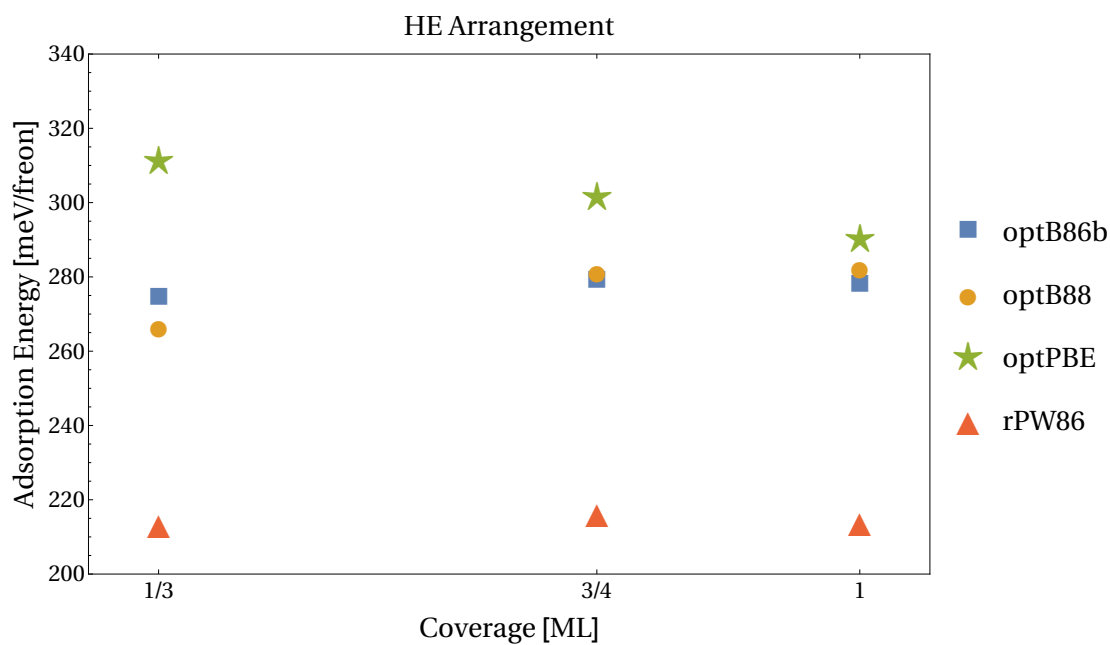


Figure 3.12: Adsorption energy for CF_3Cl adsorbates on graphene in units of energy per CF_3Cl molecule vs. coverage, as computed via DFT calculations for the HE orientation. Note that the hierarchy in the estimation of adsorption energy for every potential is not unique to the HE orientation.

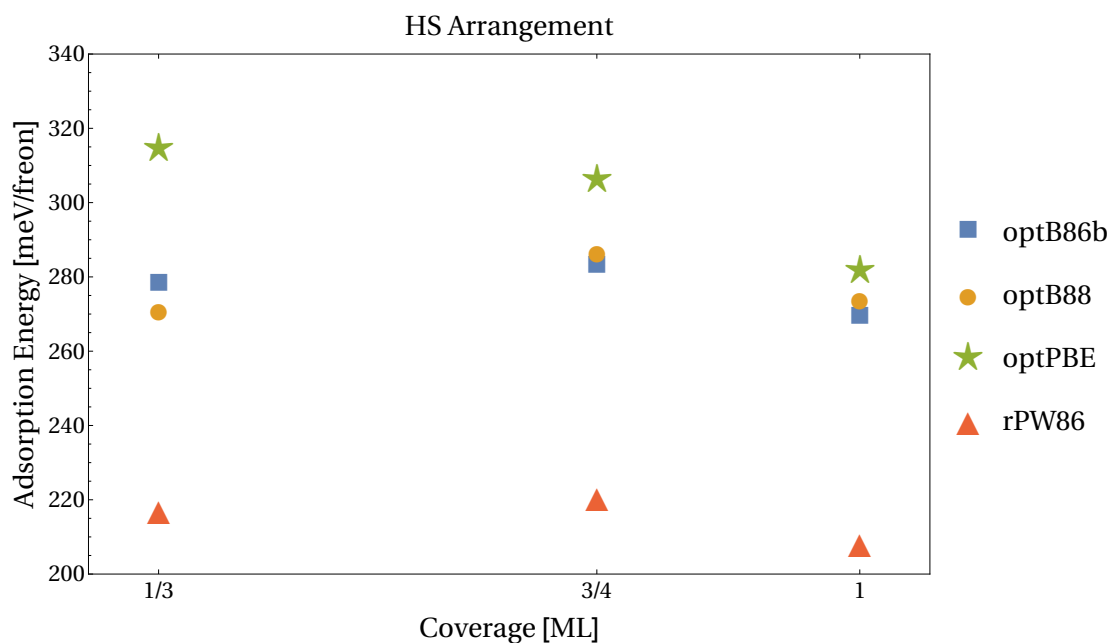


Figure 3.13: Adsorption energy for CF_3Cl adsorbates on graphene in units of energy per CF_3Cl molecule vs. coverage, as computed via DFT calculations for the HS orientation. Note that the hierarchy in the estimation of adsorption energy for every potential is not unique to the HS orientation.

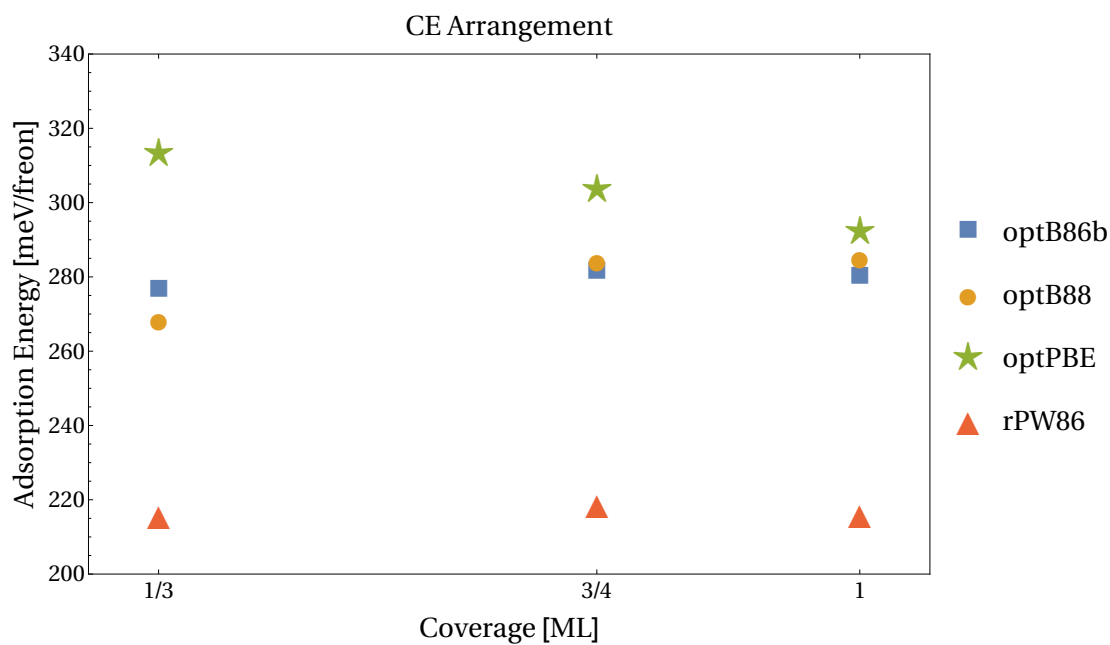


Figure 3.14: Adsorption energy for CF_3Cl adsorbates on graphene in units of energy per CF_3Cl molecule vs. coverage, as computed via DFT calculations for the CE orientation. Note that the hierarchy in the estimation of adsorption energy for every potential is not unique to the CE orientation.

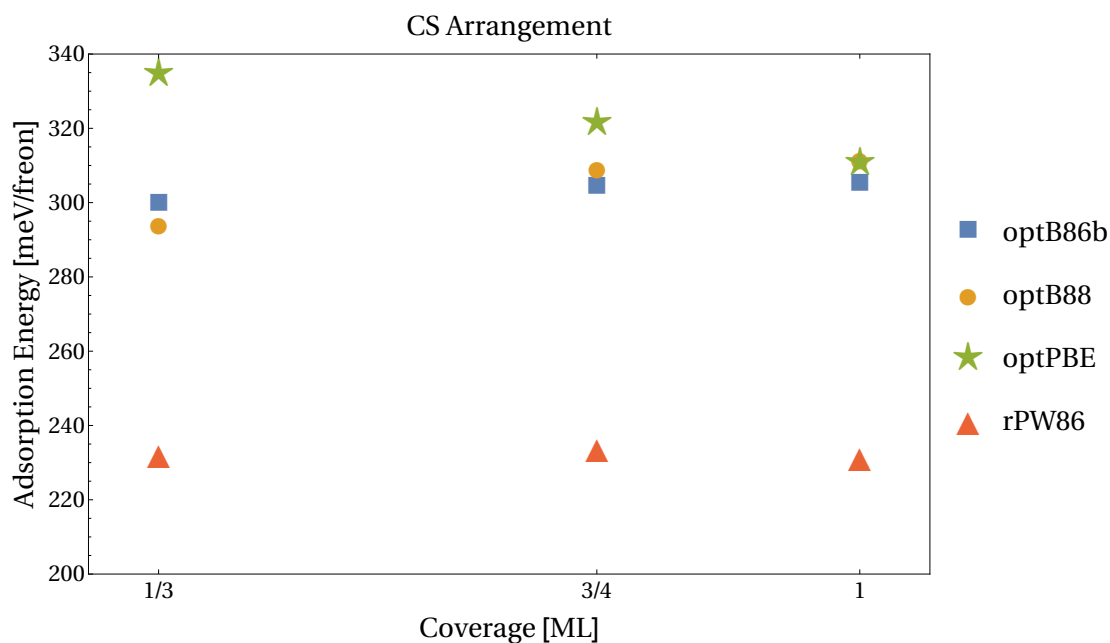


Figure 3.15: Adsorption energy for CF_3Cl adsorbates on graphene in units of energy per CF_3Cl molecule vs. coverage, as computed via DFT calculations for the CS orientation. Note that the hierarchy in the estimation of adsorption energy for every potential is not unique to the CS orientation.

For calculations at low coverage, (2×2) supercells reveal changes in the band structure of graphene (results are presented in Table 3.2, and visualized in Fig. 3.16). In general, symmetry-breaking effects are responsible for gap openings (when present), while shearing effects present negligible contributions to the gap (smaller than our least significant energy). Moreover, $V_{pp\pi}$ has a consistent value regardless of orientation, consistent with *effective nearest neighbor* interactions not being the cause of gap formation. Finally, the *pristine* systems present gaps of around 3.6 meV for the gapped states, suggesting similarly sized deformations in the graphene substrate.

The HS orientation does not produce a gap at the Dirac point, with even the *pristine* system not exhibiting a gap opening. Moreover, when considering the adsorption energy curves (Figs. 3.12 - 3.15), HS is consistently the weakest binding orientation. The C atom in CF_3Cl is located at a honeycomb hollow, with the F atoms slotted in between lattice sites; thus, HS can be visualized as roughly fitting into the substrate, which correlates with weaker binding. Additionally, this mechanical wedging does not single out either graphene sublattice, consistent with a gapless orientation (see Fig. 3.17), but also causes minimal stress of the substrate as its *pristine* variant is notably gapless.

For both HE and CE, deformations of the SLG substrate did cause gap-opening in the band structure. In both instances, the symmetry-breaking effect did not come from the location of the C–Cl bond, but rather from the eclipsing of a graphene sublattice by the F atoms. Note that both the gaps in the band structure (4.14 meV and 4.34 meV) and the gaps in the *pristine* systems (3.65 meV and 3.63 meV) are

of comparable size for HE and CE, reinforcing the idea that sublattice identification is the source of the effect (see Figs. 3.18 and 3.20).

In the CS orientation, symmetry-breaking effects are still present, and open a smaller gap. CS has consistently the largest adsorption energy in terms of the other orientations, which explains the smaller gap in its *pristine* counterpart (small deformations). In this orientation, CF_3Cl molecules are localized around a sublattice, so the symmetry-breaking contribution comes from a small depleted region in between the CF_3Cl molecules (see Fig. 3.19). The result is a weak symmetry-breaking orientation, which is consistent with a gap of 1.50 meV.

Orientation	E_{gap} (meV)	V_{eff}	V_{shear}	$V_{\text{pp}\pi}$	E_{pristine}
HS	0.00	0.00	0.00	666	0.00
HE	4.14	4.14	0.00	666	3.65
CS	1.50	1.50	0.00	667	3.57
CE	4.34	4.34	0.00	664	3.63

Table 3.2: Gaps and energies (in meV) in the band structure of SLG graphene for *low coverage* (2×2) in the *C phase*. E_{gap} is the gap in the band structure at the Dirac point, V_{eff} is the magnitude of the effective potential inducing symmetry-breaking and V_{shear} the shearing potential due to stress on the graphene substrate. E_{pristine} represents the gap in *pristine* (frozen and without the CF_3Cl adsorbate) graphene due to deformations. $V_{\text{pp}\pi}$ represents the *effective nearest neighbor* interactions for the *folded* (2×2) supercell.

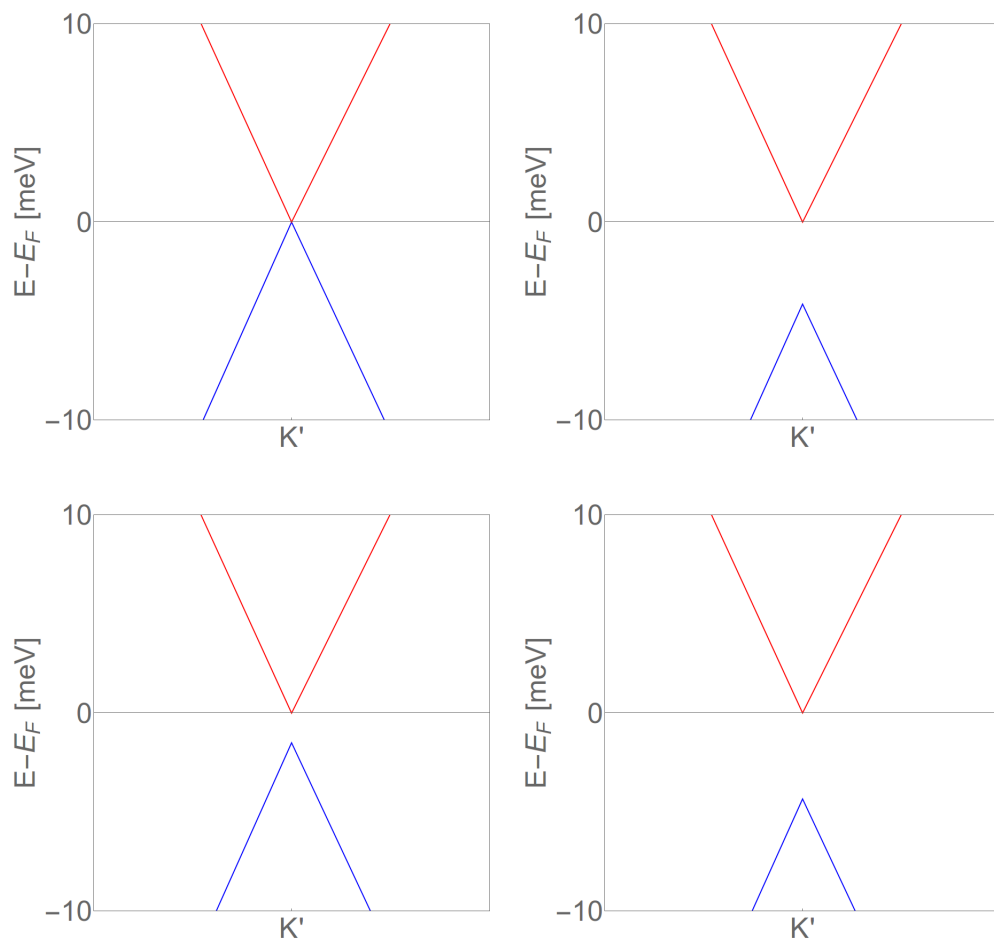


Figure 3.16: Gaps (meV) in the band structure of SLG graphene for *low coverage* (2×2) at the *C phase*. Note that due to folding, the K point in (1×1) is mapped to K' in (2×2). Gaps (when present) open the valence band (blue) from the conduction band (red) below the Fermi level (n-type). The band structure about K' is presented for all orientations: **Top, Left**) HS, **Top, Right**) HE, **Bottom, Left**) CS, and **Bottom, Right**) CE.

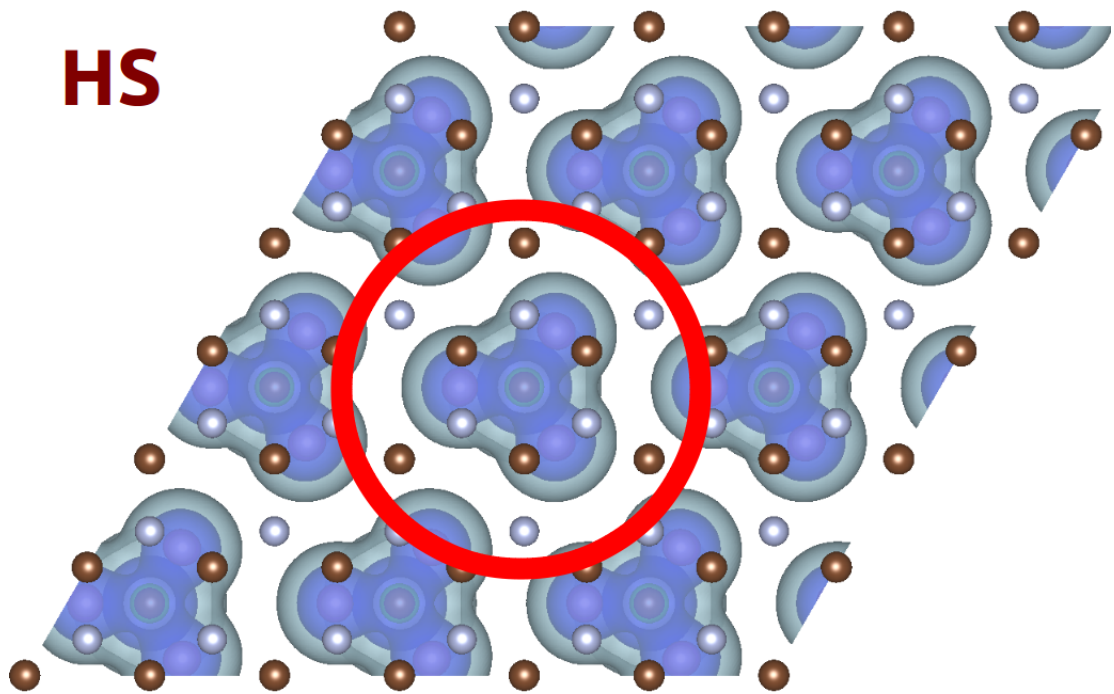


Figure 3.17: LDOS for HS orientation with LDOS localization about the CF_3Cl overlayer in the *C-phase* at low coverage (2×2). Graphene sublattices are colored brown and cyan, respectively. Note the complete lack of symmetry-breaking effects in this orientation, as all sublattices are affected by the CF_3Cl molecules equally (emphasis in red).

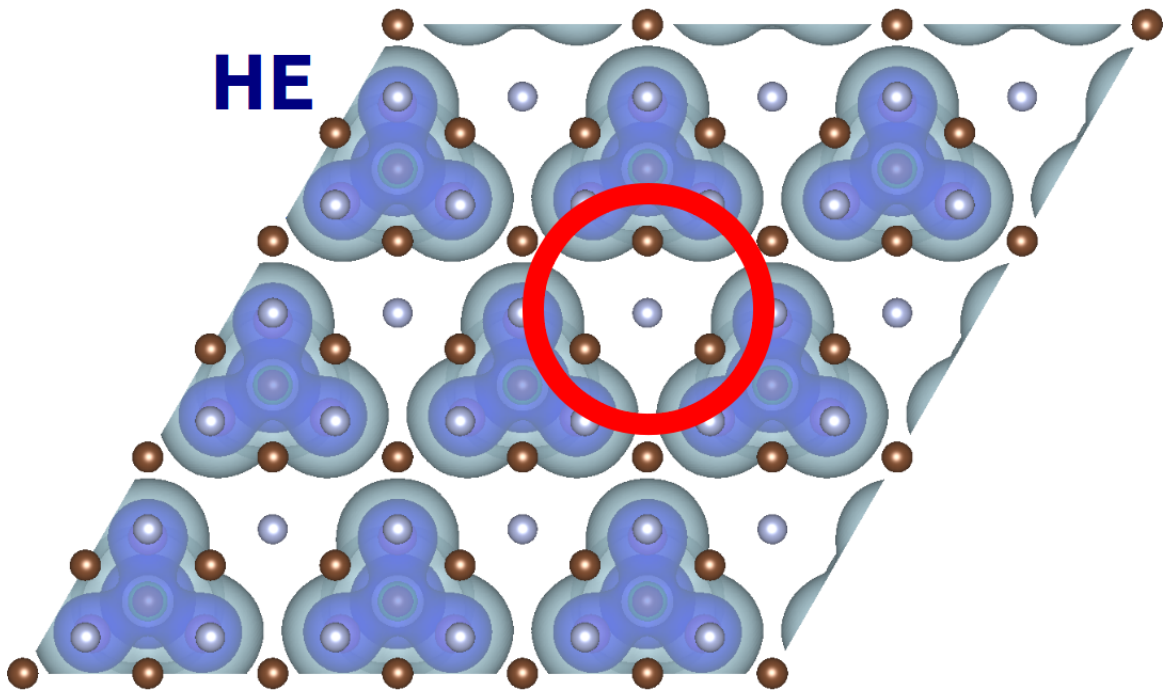


Figure 3.18: LDOS for HE orientation with LDOS localization about the CF_3Cl overlayer in the *C-phase* at low coverage (2×2). Graphene sublattices are colored brown and cyan, respectively. Note symmetry-breaking effects in this orientation, as one sublattice is largely unaffected by the CF_3Cl molecules (emphasis in red).

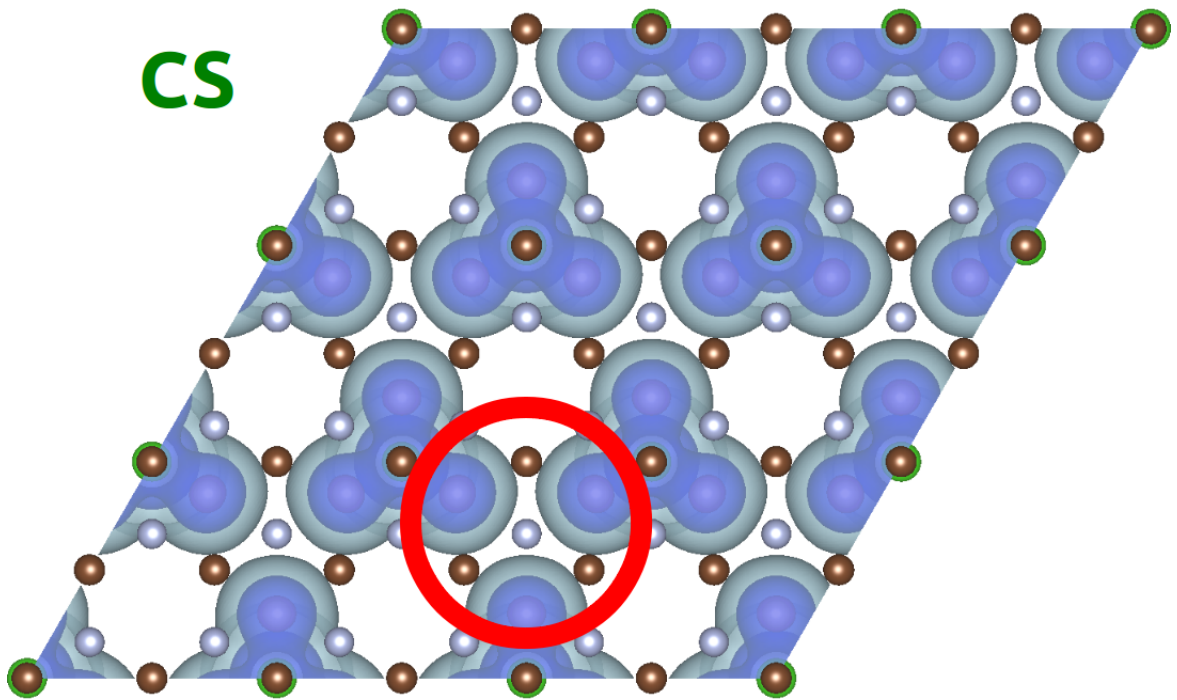


Figure 3.19: LDOS for CS orientation with LDOS localization about the CF_3Cl overlayer in the C -phase at low coverage (2×2). Graphene sublattices are colored brown and cyan, respectively. Note weaker symmetry-breaking effects in this orientation, as one sublattice is *slightly* less affected by the CF_3Cl molecules (emphasis in red).

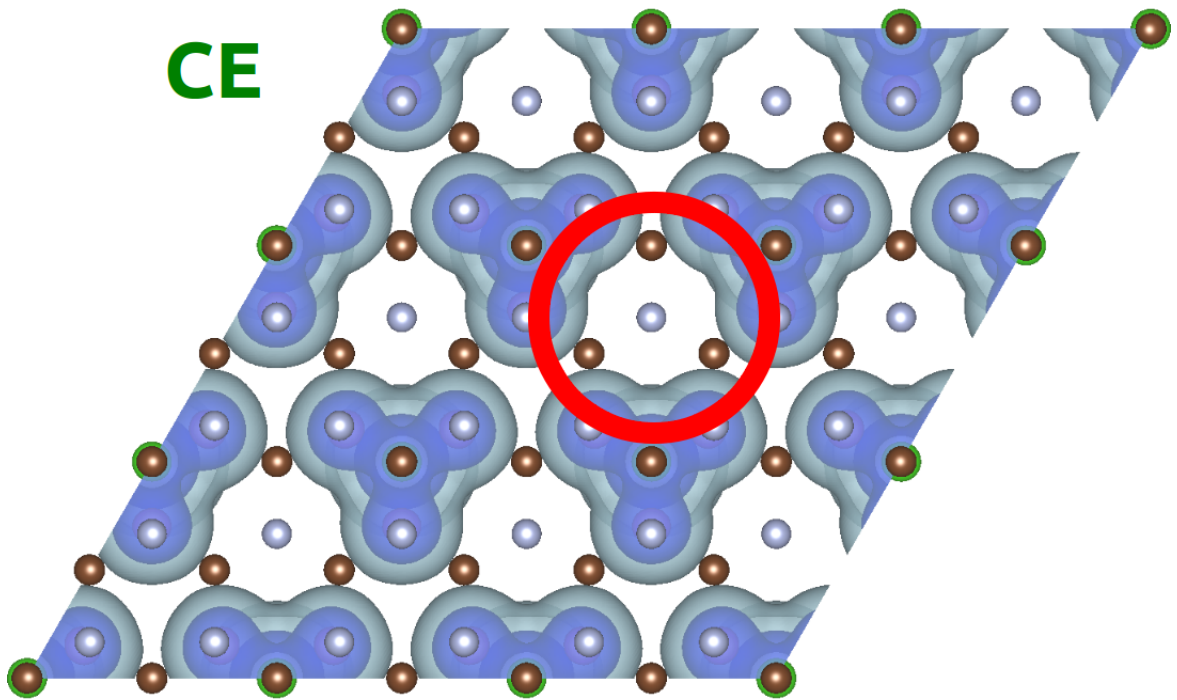


Figure 3.20: LDOS for CE orientation with LDOS localization about the CF_3Cl overlayer in the *C-phase* at low coverage (2×2). Graphene sublattices are colored brown and cyan, respectively. Note symmetry-breaking effects in this orientation, as one sublattice is largely unaffected by the CF_3Cl molecules (emphasis in red).

In the case of high coverage, i.e. $(\sqrt{3} \times \sqrt{3})$ supercells, deformations on the graphene substrate increase with CF_3Cl density (results are presented in Table 3.3, and visualized in Fig. 3.21). In general, symmetry-breaking effects are responsible for gap openings (when present), while shearing effects present negligible contributions to the gap (smaller than our least significant energy). While, $V_{\text{pp}\pi}$ has a consistent value regardless of orientation, the *effective nearest neighbor* interactions have increased to 1.2 eV, so that they are also accounting for electrical effects due to the CF_3Cl adsorbate. Since the graphene substrate is saturated with as much CF_3Cl as possible in a monolayer, symmetry-breaking does not come through sublattice identification, but rather from the way orientations create larger *meta sublattices*.

Two orientations, HS and HE, have enhanced gaps at the Dirac point. For HS the result is most dramatic, as the largest gap for this coverage (18.0 meV) arises from a gapless orientation at low coverage; results for HE also present an enhanced gap of 8.51 meV. If we visualize the localized CF_3Cl molecules as sites in a triangular *meta overlayer* (of effective bond length $\sqrt{3}a$), the gaps can be explained as symmetry-breaking effects in these *meta sublattices*. For HE, the *meta overlayer* is formed by small depletion zones that act as *meta graphene sublattices* (see Fig. 3.23). Though there is no differentiation between the *meta graphene sublattices*, the discrepancy in lattice constant from the *meta overlayer* with that of graphene, breaks the underlying sublattice symmetry. A similar effect occurs for HS, with the additional consideration that the *meta graphene sublattices* are not depletion zones, but rather CF_3Cl molecules themselves and sparse LDOS regions. Hence, in addition to the lattice constant mismatch, there is a *meta graphene sublattice*

differentiation, which accounts for the large gap (see Fig. 3.22).

Contrastingly, for CS and CE, the S_1 and S_2 sublattices are not significantly differentiated (see Figs. 3.24 - 3.25). More importantly, in both orientations the *meta overlayer* does not present a graphene-like structure, but rather a triangular one that does not conflict with the underlying graphene substrate. Therefore, the only symmetry-breaking effects are those coming from weak sublattice differentiation, and not *meta overlayer* formation; hence, the small gaps.

Finally, as the substrate is maximally dense, the *pristine* gaps can be explained mechanically. In increasing order, CE, CS, HE, and HS present *pristine* gaps from 1.73 meV up to 9.29 meV, and are consistent with CF_3Cl molecules increasingly wedging into the substrate at the ground state. Nevertheless, given maximal coverage, these deformations are more akin to packing effects, rather than symmetry-breaking ones

Orientation	E_{gap} (meV)	V_{eff}	V_{shear}	$V_{\text{pp}\pi}$	E_{pristine}
HS	18.0	18.0	0.00	1999	9.29
HE	8.51	8.51	0.00	1999	7.30
CS	1.55	1.55	0.00	2012	7.01
CE	3.68	3.68	0.00	2001	1.73

Table 3.3: Gaps and energies (in meV) in the band structure of SLG graphene for *high coverage* ($\sqrt{3} \times \sqrt{3}$) in the *C phase*. E_{gap} is the gap in the band structure at the Dirac point, V_{eff} is the magnitude of the effective potential inducing symmetry-breaking and V_{shear} the shearing potential due to stress on the graphene substrate. E_{pristine} represents the gap in *pristine* (frozen and without the CF_3Cl adsorbate) graphene due to deformations. $V_{\text{pp}\pi}$ represents the *effective nearest neighbor* interactions for the *folded* ($\sqrt{3} \times \sqrt{3}$) supercell.

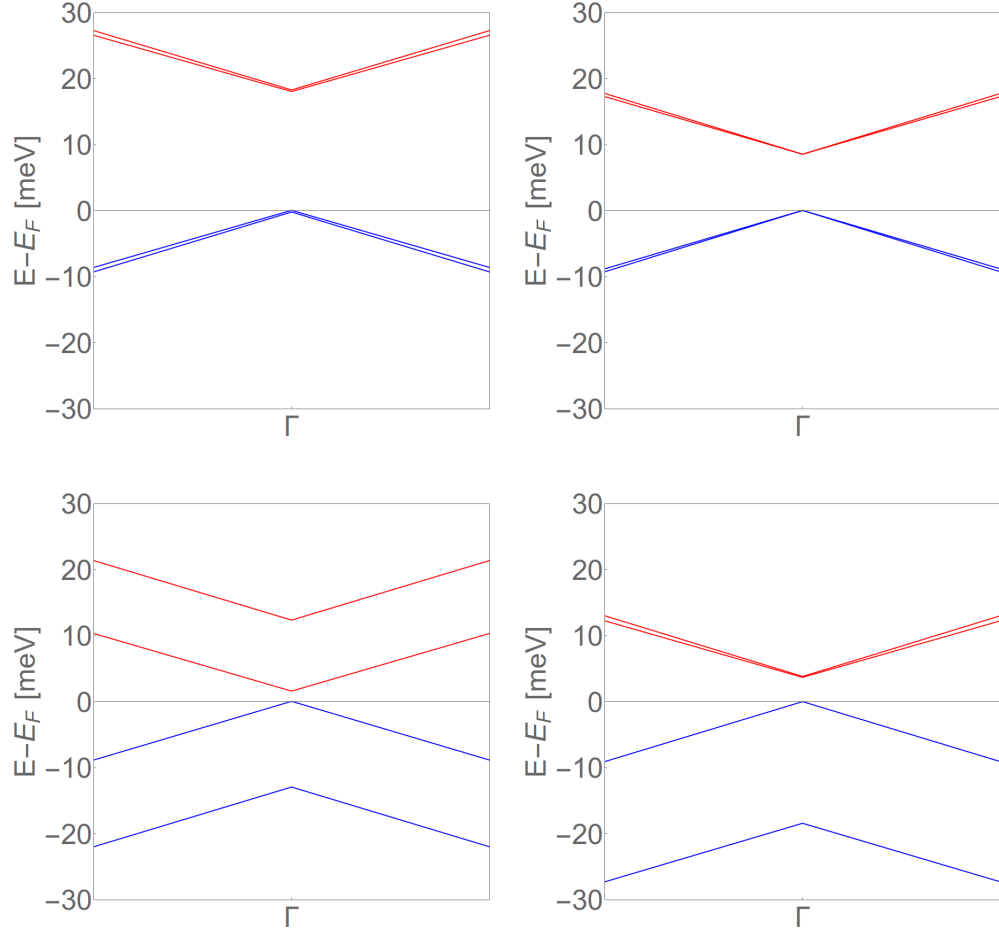


Figure 3.21: Gaps (meV) in the band structure of SLG graphene for *high coverage* ($\sqrt{3} \times \sqrt{3}$) at the *C phase*. Note that due to folding, the *K* point in (1×1) is mapped to Γ in $(\sqrt{3} \times \sqrt{3})$. Gaps (when present) open the valence band (blue) from the conduction band (red) above the Fermi level (p-type). The band structure about Γ is presented for all orientations: **Top, Left**) HS, **Top, Right**) HE, **Bottom, Left**) CS, and **Bottom, Right**) CE.

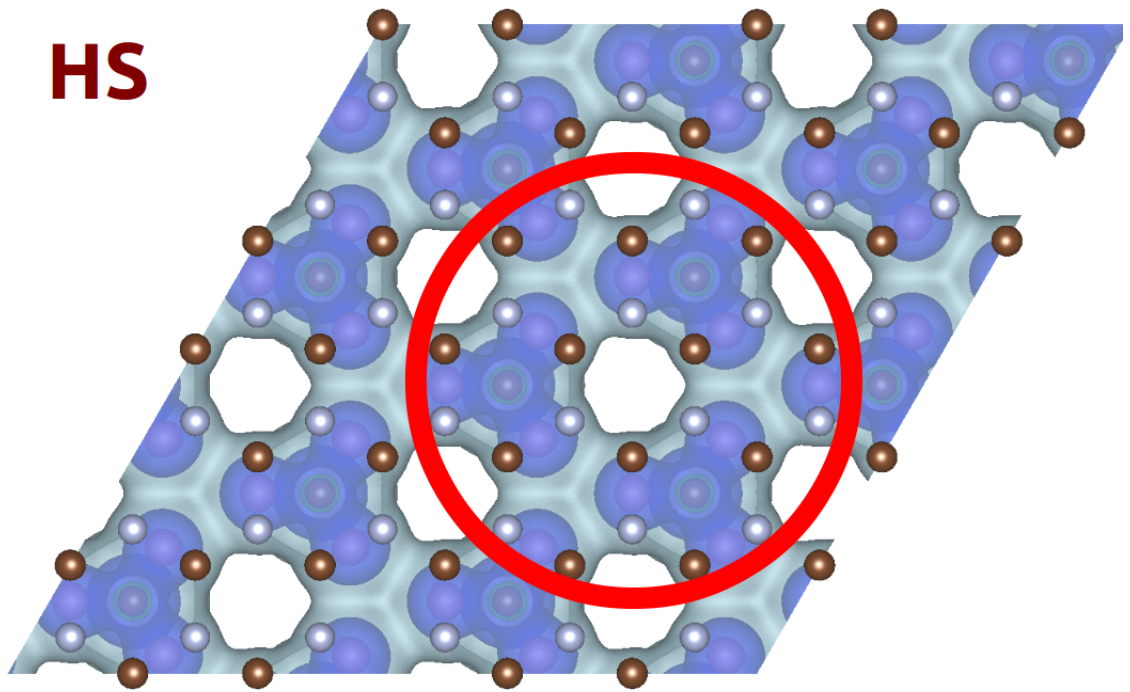


Figure 3.22: LDOS for HS orientation with LDOS localization about the CF_3Cl overlayer in the *C-phase* at high coverage ($\sqrt{3} \times \sqrt{3}$). Graphene sublattices are colored brown and cyan, respectively. Note symmetry-breaking effects in this orientation are due to the formation of a graphene-like *meta overlayer* (lattice constant $\sqrt{3}a$), with differentiated *meta sublattices* (emphasis in red).

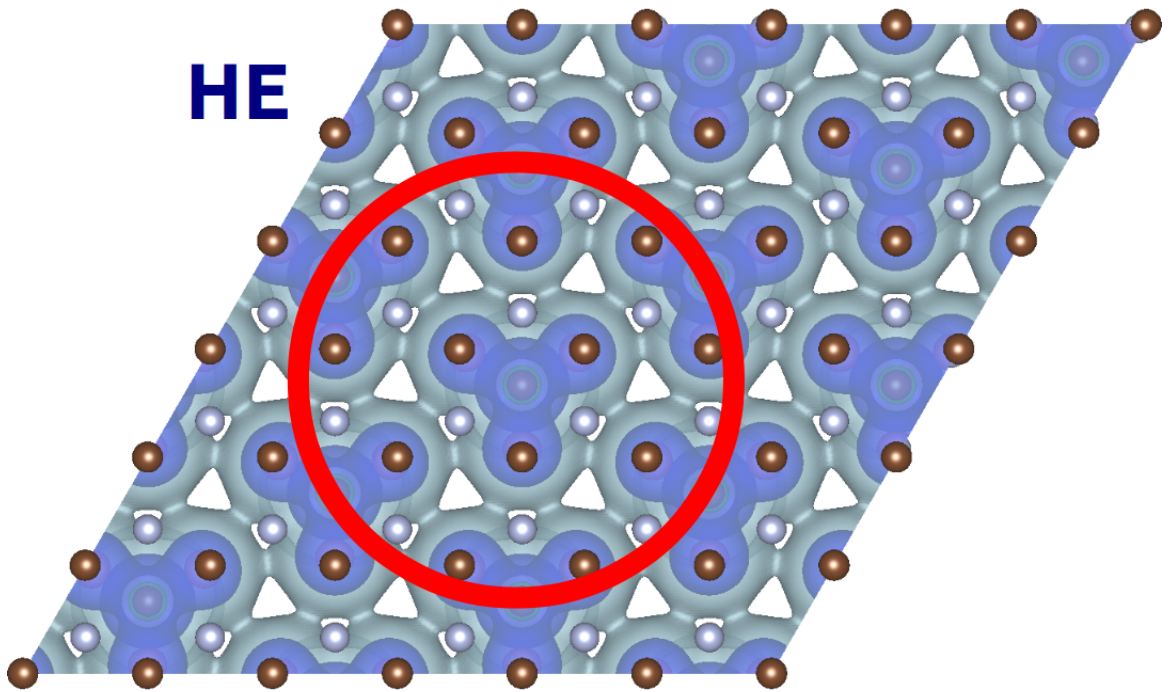


Figure 3.23: LDOS for HE orientation with LDOS localization about the CF_3Cl overlayer in the *C-phase* at high coverage ($\sqrt{3} \times \sqrt{3}$). Graphene sublattices are colored brown and cyan, respectively. Note symmetry-breaking effects in this orientation are due to the formation of a graphene-like *meta overlayer* (lattice constant $\sqrt{3}a$), with mismatching lattice constant with respect to the underlying graphene substrate (emphasis in red).

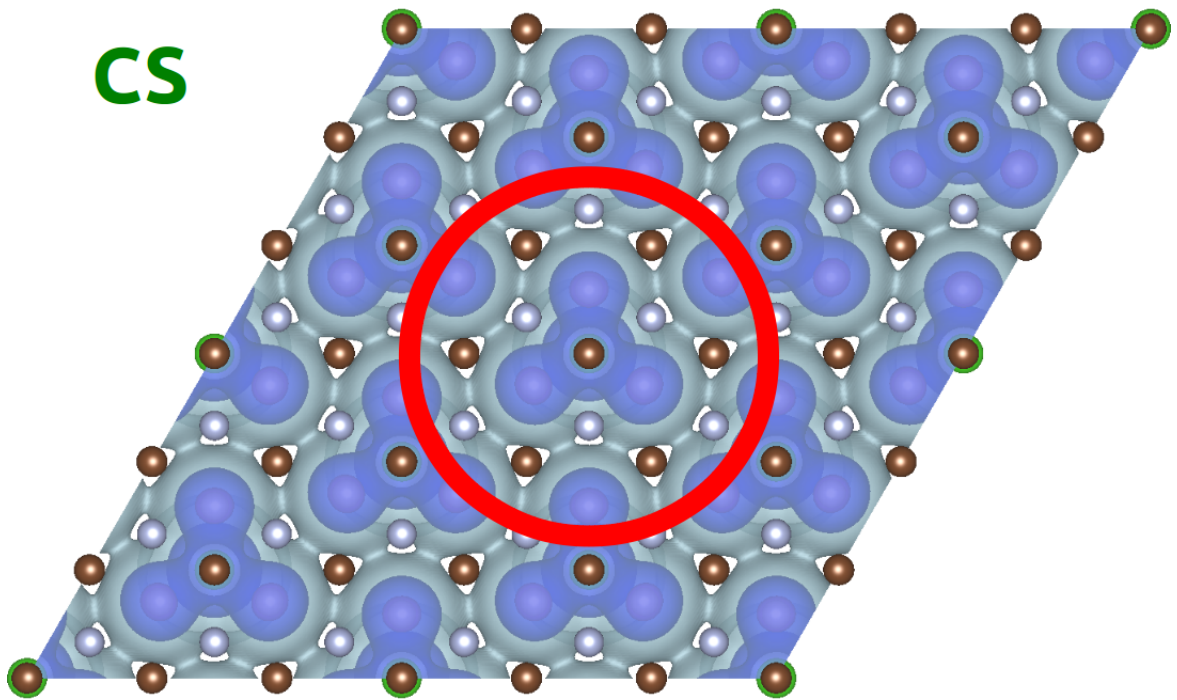


Figure 3.24: LDOS for CS orientation with LDOS localization about the CF₃Cl overlayer in the *C-phase* at high coverage ($\sqrt{3} \times \sqrt{3}$). Graphene sublattices are colored brown and cyan, respectively. Note symmetry-breaking effects in this orientation are due to weak sublattice differentiation, as the formation of a triangular *meta overlayer* does not conflict with the underlying graphene substrate (emphasis in red).

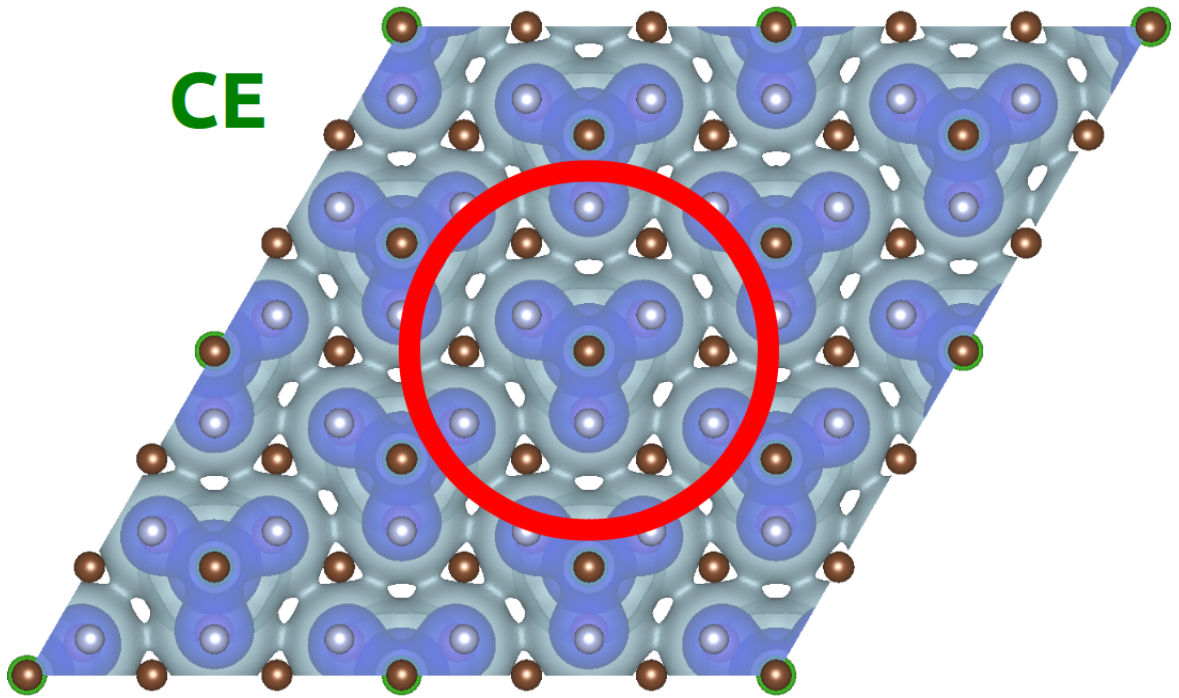


Figure 3.25: LDOS for CE orientation with LDOS localization about the CF_3Cl overlayer in the *C-phase* at high coverage ($\sqrt{3} \times \sqrt{3}$). Graphene sublattices are colored brown and cyan, respectively. Note symmetry-breaking effects in this orientation are due to weak sublattice differentiation, as the formation of a triangular *meta overlayer* does not conflict with the underlying graphene substrate (emphasis in red).

We consider symmetry-breaking effects on BLG at low coverage, $(2 \times 2)_2$ (see Table 3.4), to avoid the formation of *meta overlayers* that may complicate symmetry-breaking effects due to sublattice differentiation. Without loss of generality, consider the *top* SLG stack to be the one closest to the adsorbate with sublattices S_1 and S_2 ; there are two possible arrangements for the *bottom* SLG stack, one with sublattices S_1 and S_3 , and the other with sublattices S_2 and S_3 (see Fig. 3.26). As evidenced in tight-binding calculations for BLG [81], adsorbates can open a gap $E_{\text{gap}} \approx |\delta_3 - \delta_{\text{off}}|$, where δ_x is the effective potential on sublattice S_x , and δ_{off} is the potential on the top SLG sublattice not shared with the bottom SLG stack (labeled S_{off}). Note that deformation effects, graphene-graphene stack interactions, and the effective potential on the *shared* sublattice are remarkably absent from the energy gap.

Two orientations are chosen, HS and HE, both with CF_3Cl molecules at the hollow S_3 site. For orientations HS_1 and HS_2 (where the subscript denotes the sublattice shared by both SLG stacks), the lack of symmetry-breaking effects for HS in SLG renders HS_1 and HS_2 as chiral copies of one another, with an F atom acting directly on S_{off} . Hence, we observe large gaps of about 25 meV in both instances. For orientations HE_1 and HE_2 , CF_3Cl is placed such that F atoms act on the S_1 sublattice for the top SLG stack. Therefore, S_{off} is S_2 , so HE_2 should exhibit a larger gap than HE_1 , which is confirmed through gaps of 8.9 meV and 7.1 meV, respectively.

The last consideration should be the difference in gap size between HS_x and HE_x orientations. Notably, HS_x orientations have CF_3Cl localized much more di-

rectly above S_3 when compared to HE_x , making E_{gap} considerably stronger in the former. Finally, the *pristine* gaps confirm that deformations play an even smaller role in gap opening for BLG, since *pristine* gaps are at most 2 meV.

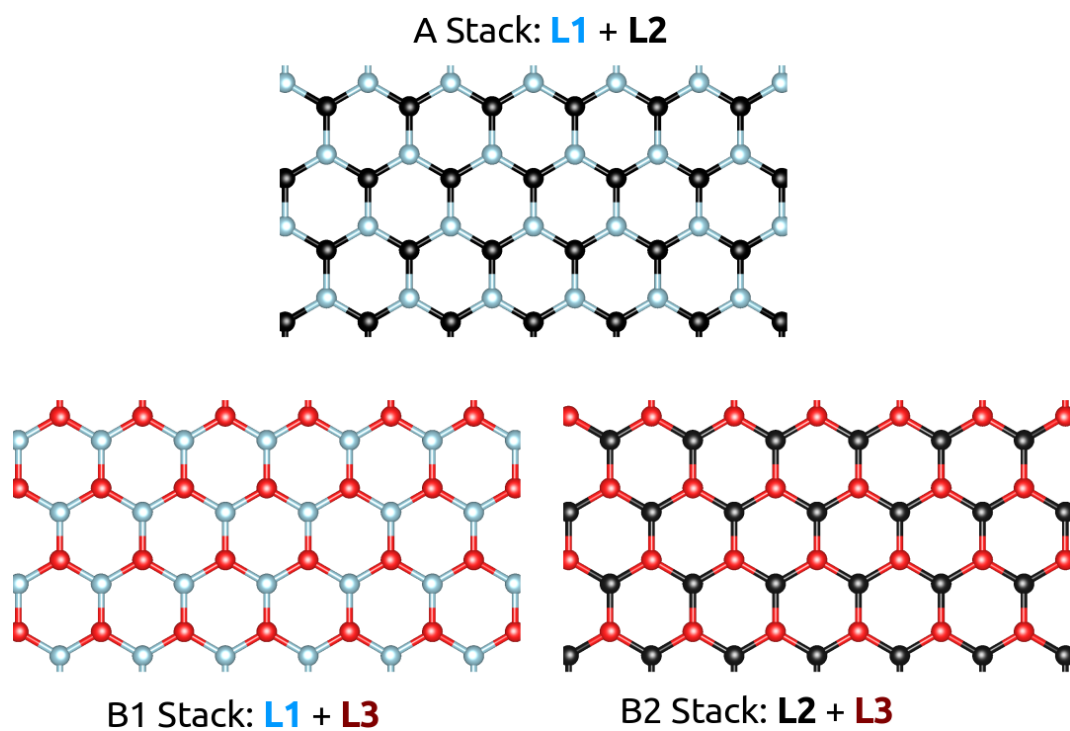


Figure 3.26: Schematic of the two possible configurations for BLG. In the top stack, sublattices are identified as S_1 (blue sites) and S_2 (black sites). The bottom SLG stack can consist of S_1 and S_3 (red sites) sublattices (subscript $_1$), or S_2 and S_3 sublattices (subscript $_2$).

Orientation	E_{gap} (meV)	E_{pristine} (meV)
HS ₁	23.8	0.1
HS ₂	24.5	0.1
HE ₁	7.1	1.9
HE ₂	8.9	0.2

Table 3.4: Gaps (in meV) in the band structure of BLG for *low coverage* (2×2) in the *C phase*. E_{gap} is the gap in the band structure at the Dirac point, and E_{pristine} represents the gap in *pristine* (frozen and without the CF_3Cl adsorbate) BLG due to deformations. The subscript in the orientations denotes the sublattice in the bottom SLG stack shared with the top SLG stack, as the CF_3Cl molecule is localized about S_3 in both cases.

Summary and Conclusion

We performed DFT calculations of CF_3Cl adsorbed onto SLG and BLG, motivated by previous DFT results of adsorbates on graphene [60] and by experiments that measured interesting electrical properties of CF_3Cl on BLG [63]. The supercells were devised to minimize self-interaction effects of the adsorbate with itself and to maximize the k -point density to observe the likely weak effects on the electrical structure of graphene. High energy cutoffs (600eV) for the wave functions and dense k -point meshes (denser than $30 \times 30 \times 1$ due to supercell folding) were employed along with different types of van der Waals interactions in VASP 5.3.3.

Calculation of the adsorption energy reveals that the system is physisorbed with sample adsorption energy of 220meV per CF_3Cl molecule, which suggests any changes to the electrical properties of graphene are the result of symmetry-breaking effects, as we have used tight-binding analysis to show that shearing effects on gap opening are negligible.

For low CF_3Cl coverage, molecules are sparse enough to make sublattice differentiation the definitive mechanism for symmetry-breaking. For CE and HE with F atoms from CF_3Cl acting on a given SLG sublattice, sublattice differentiation is directly related to symmetry-breaking effects and the opening of small gaps (4 meV) in the band structure. Analogous, but weaker effects are observed in CS, which opens a gap of 1.5 meV. The most striking result, however, is HS, in which CF_3Cl molecules are located in a graphene honeycomb with F atoms affecting sublattices equally, thus not opening gaps.

For maximal coverage, shearing considerations cannot be relied upon, as all possible orientations deform the SLG substrate similarly. Explicitly, the deformation is uniform across orientations, and the ~ 7 meV gaps of the *pristine* systems reveal that shearing at high coverage does not induce symmetry-breaking by itself. Additionally, dense packing makes it difficult to argue for sublattice differentiation, since the molecules are no longer meaningfully localized about any given SLG sublattice. Symmetry-breaking effects come from the creation of a graphene-like *meta overlayer*, in which the CF_3Cl molecules (or depleted zones) represent *meta sublattices*. In CS and CE orientations (with the C–Cl bond above a SLG sublattice), the *meta overlayer* is a triangular one, with no identification between any of the *meta sublattices*, thus, not breaking SLG symmetry. Contrastingly, the HE and HS orientations (with C–Cl bonds in the honeycomb hollows) induce a graphene-like *meta overlayer* in which the CF_3Cl molecules act as *meta sublattices*. These *meta overlayers* have bond length $\sqrt{3}a$, which creates an effective potential on SLG due to bond size mismatch. Thus, we observe gaps for HE and HS at high coverage, of 8.51 meV and 18.0 meV, where the enhanced HS gap comes not only from the graphene-like *meta overlayers*, but from *meta sublattice* differentiation, further breaking symmetry.

Additional calculations were performed on BLG, where symmetry-breaking effects come from the application of an effective potential to the sublattice in the top SLG stack that is not shared with the bottom SLG stack, S_{off} . At low coverage, HS and HE configurations were employed to apply different effective potentials to S_{off} , as CF_3Cl molecules sit at the hollow S_3 site. Overall, gap openings were

enhanced, with the most dramatic effect that of the HS configuration (gapless in SLG): in BLG, the localization of CF_3Cl about S_3 and the strong potential on S_1 and S_2 was enough to break sublattice symmetry between the top and bottom SLG stacks, producing a gap of 25 meV (the largest in our study).

Chapter 4: Conclusion and Future Work

Transient Mobility Effects

Of our many assumptions, modeling binding energy as a constant E_b was reasonably effective. This assumption allowed us to compare thermal and athermal effects for the lifetime of the sub-critical clusters, without considering the size of the clusters themselves. An exploration of the underlying substrate, and how it impacts the binding energy can probe the limits of this assumption. For example, in a triangular or hexagonal substrate, for sub-critical islands larger than $s = 2$ but smaller than the critical nucleus size i , one can access unstable islands of size s with different binding energies. These energies are connected both to the geometry of the substrate, and to the accessible configurations for the specific monomer under study. Specifically, in a triangular substrate, N_3 can be linear (with one nearest neighbor) or triangular (with two nearest neighbors), and should exhibit two different binding energies and decay rates. Thus, we propose a new *thermal* component of the island lifetime:

$$\left(\tilde{\tau}_s^{\text{th}}\right)^{-1} = \sum_j w_{j,s} \exp(-\beta E_{b,s}) \quad (4.1)$$

where $w_{j,s}$ are proportionality constants that depend on the geometry of the substrate, and $E_{b,s}$ are the associated binding energies. Notice that this new β dependence would introduce finer energetic regimes in the transitional terms, much like \mathcal{R}_n and \mathcal{R}_B do at the limiting regimes, so we are likely to access a new *lattice channel*. However, as these effects would present on the *left* side of Eqn. 2.24, it is likely that only a richer effective activation energy space could be accessed, while the growth exponents would remain unchanged.

A second possible extension to the model would focus not on the lifetime of unstable islands, but on the formation of multiple levels in subcritical (and critical) islands. In this case, the modifications occur earlier in the development of the solution, so our intuition is more limited. One of the most obvious consequences is that the density of thermalized monomers would have independent rate equations per *level* (much like Eqn. 2.18), but would introduce a new lifetime $\tau_{N_i \rightarrow N_{i+1}}$ with an associated energy E_{hop} describing the likelihood that these thermalized monomers *step down* (*step up*) from a particular level. An even more insidious matter would be modeling the hot-monomers: should they be considered truly athermal and act like so for all levels, and under what conditions is this approximation justifiable?

Finally, a more straightforward extension would be applying to model to other growth-like experiments with interesting transitional regimes. Any experimental space with a large sampling of temperature runs would be welcome, as a broad β space is crucial to constraining the energies in the model: growth scaling data is also important, but energy scaling remains a harder problem to tackle than finding the critical nucleus size in a system.

CF₃Cl Overlayers and Symmetry-Breaking

Though we performed exhaustive work on CF₃Cl SLG adsorbates, BLG results were not explored for all possible configurations. A good confirmation test would be exploration of CE₁ and CE₂ configurations for CF₃Cl on the S_1 sublattice: as δ_{off} is either S_1 (acted on by CF₃Cl) or S_2 (acted on by F atoms), there should be two distinct band gaps.

Though van der Waals potentials were essential to binding the CF₃Cl adsorbate to SLG and BLG, the requirement of a large supercell vacuum to minimize self-interaction effects (of adsorbate repetitions across the vacuum), was certainly taxing in a computational sense (due to the non-localities present in the implementation). Therefore, in the case of studying different adsorbates on SLG, special care must be given to justifying a smaller supercell vacuum, hopefully diminishing the computational cost of including these non-local effects. Additionally, our understanding of symmetry-breaking systems should account for the newest developments in vdW potentials, which further improve on weakly covalent systems.

In this work we exploited the folding of the reciprocal space due to the increased dimension of the supercell, and treated the weak symmetry-breaking effects as effectively acting on a representative SLG substrate. However, a more complete examination of the system would put aside the folding approximation, and construct the full tight-binding Hamiltonian for the (2×2) and $(\sqrt{3} \times \sqrt{3})$ supercells. With the full Hamiltonian, symmetry-breaking effects could be specifically accounted for on a sublattice-by-sublattice basis, and provide a quantitative correlation between

effective potential and gap opening. However, this non-trivial analysis does not provide analytic solutions for the gaps, as the tight-binding calculations would necessitate solving characteristic polynomials of degree 8 and 18, respectively. Though we would lose the well-behaved results constructed in this work, we would gain more accurate insight into the particular sublattices being differentiated.

Finally, we suggest an examination of TLG (trilayer graphene), in which the most common experimental form (namely ABA graphene) can be visualized as AB_2A using the notation from Fig. 3.26. For this system, CF_3Cl adsorbates acting on the shared sublattice should not open a gap, as they do not break sublattice symmetry. Instead, CF_3Cl adsorbates acting on non-shared sublattices are expected to open gaps. Extending our BLG results into TLG could certainly confirm that sublattice differentiation across SLG stacks is in fact a symmetry-breaking mechanism.

Appendices

Appendix A: Code for Hot-Monomer Analysis

All *Mathematica* code employed to compute and fit the kernel, asymptotic solution, and full solution is presented here.

Header Code

To be loaded in all notebooks used in hot-monomer analysis.

```
1  (*****)  
2  (** PRE-PROCESSOR CODE FOR ALL NOTEBOOKS **)  
3  (*****)  
4  Needs["NumericalCalculus"];  
5  Off[NIntegrate::inumr];  
6  Off[FindRoot::nlnum];  
7  Off[ReplaceAll::reps];  
8  
9  (*****)  
10 (** SIMPLIFICATION RULES **)  
11 (*****)  
12 (** Logarithmic rule **)  
13 revlogrule = {Log[x_ y_] :=> Log[x] + Log[y], Log[x_^n_] :=> n Log[x] };  
14
```

```

15  (***** )
16  (** BASIC FORMS **)
17  (***** )
18  (** f Kernel **)
19  f[ε-, i-, Rn-,
20     Rb-] = εi +
21           1)*(1 + ε(1/2))(i + 1)/(1 + Rn*ε)/(1 +
22           Rb*ε)(i);
23
24  (***** )
25  (** APPROXIMATIONS **)
26  (***** )
27  (** Approximate ln F: ln N, β, i, ED=ΔD2, Eph=
28  Δp2+ED, offsets **)
29  sFA0[sN-, β-, β1-, β2-, β3-, β4-,
30     i-, ΔD-, Δp-, γN-, λn-, \
31  λB-, λ1-, λ2-, λ3-, λ4-] = \
32  (Log[
33     Simplify[
34     ε*
35     f[ε, i, Exp[γn - β*(ED + Eph)],
36     Exp[γB - β*Eph]]*
37     Exp[-(2 + i) (γN +
38     2 β (ΔD2 + \
39  Δp2))] /. {ε ->
40     Exp[sN + γN +
41     2 β*Eph]} /. {Eph -> Δp2 + ED,

```

```

42      Eb -> Δb^2 +
43      ED} /. {ED -> ΔD^2}
44      ,
45      Assumptions -> {Im[sN] == 0, Im[γN] == 0,
46      Im[β] == 0, Im[ΔD] == 0,
47      Im[Δp] == 0, Im[γb] == 0}]
48      ] /. {γB -> λB - γN, γn -> \
49      λn - γN} // revlogrule)/(i) +
50      KroneckerDelta[β - β1]*λ1 +
51      KroneckerDelta[β - β2]*λ2 +
52      KroneckerDelta[β - β3]*λ3 +
53      KroneckerDelta[β - β4]*λ4;
54
55      (** Approximate ln F: ln N, β, i, ED=ΔD^2, Eph=\
56      Δp^2+ED, Eb=Δb^2+ED **)
57      sFA[sN_, β_,
58      i_, ΔD_, Δp_, Δb_, \
59      γN_, λn_, γB_, λθ_] = Simplify[
60      Log[
61      Simplify[
62      ε*
63      f[ε, i, Exp[γn - β*(ED + Eph)],
64      Exp[γB - β*Eph]]*(1 +
65      Exp[γB - β*Eb])^(i - 1)/
66
67      Exp[β*(2*Eph*i + 4*Eph +
68      ED) + γθ] /. {ε ->

```

```

69      Exp[sN +  $\gamma$ N +
70      2  $\beta$ *Eph]} /. {Eph ->  $\Delta$ p^2 + ED,
71      Eb ->  $\Delta$ b^2 +
72      ED} /. {ED ->  $\Delta$ D^2} /. { $\gamma$  $\theta$  \
73 -> (2 + i)  $\gamma$ N -  $\lambda$  $\theta$ ,  $\gamma$ n ->  $\lambda$ n - \
74  $\gamma$ N}
75      , Assumptions -> {Im[sN] == 0, Im[ $\gamma$ N] == 0,
76      Im[ $\beta$ ] == 0, Im[ $\Delta$ D] == 0,
77      Im[ $\Delta$ p] == 0, Im[ $\gamma$ b] == 0}
78      ] // revlogrule
79      ]/i;
80
81      (**  $\lambda$  vs  $\beta$ : Used to find an approximation for Eb **)
82      sFB[ $\beta$ _,
83      i_,  $\Delta$ D_,  $\Delta$ b_,  $\gamma$ N_,  $\lambda$ B_, \
84       $\lambda$  $\theta$ _] =
85      Simplify[Simplify[
86      Simplify[
87      sFA[sN,  $\beta$ ,
88      i,  $\Delta$ D,  $\Delta$ p,  $\Delta$ b, \
89       $\gamma$ N,  $\lambda$ n,  $\lambda$ B -  $\gamma$ N,  $\lambda$  $\theta$ ] -
90      sFA0[sN,  $\beta$ ,  $\beta$ 1,  $\beta$ 2,  $\beta$ 3,  $\beta$ 4,
91      i,  $\Delta$ D,  $\Delta$ p,  $\gamma$ N, \
92       $\lambda$ n,  $\lambda$ B, 0, 0, 0,
93      0]] /. { $\lambda$ B ->  $\lambda$ X +  $\gamma$ N +  $\beta$ *(\
94       $\Delta$ b^2 +  $\Delta$ D^2)}} // revlogrule] /. { $\lambda$ X ->  $\lambda$ B - ( $\gamma$ N + \

```

```

96   $\beta*(\Delta b^2 + \Delta D^2))$ };
97
98  (*****
99  (** FULL SOLUTION **)
100 (*****
101 (** Full ln F: ln N,  $\beta$ ,  $i$ , ED= $\Delta D^2$ , Eph=\
102  $\Delta p^2+ED$ , Eb= $\Delta b^2+ED$  **)
103 sFF[sN_,  $\beta$ _,
104   i_,  $\Delta D$ _,  $\Delta p$ _,  $\Delta b$ _, \
105  $\gamma N$ _,  $\gamma n$ _,  $\gamma B$ _,  $\gamma \theta$ _] :=
106   Log[NIntegrate[
107     Exp[z $\epsilon$  (2 + i)]*(1 +
108       Exp[z $\epsilon$  +  $\gamma B$  -  $\beta*(\Delta D^2 + \Delta p^2)$ ]](-i)*(1 + Exp[z $\epsilon$ /2])(i + 1)/(1 +
109       Exp[z $\epsilon$  +  $\gamma n$  -  $\beta*(2 \Delta D^2 + \Delta p^2)$ ]]), {z $\epsilon$ , -Infinity,
110       sN +  $\gamma N$  +
111       2  $\beta*(\Delta D^2 + \Delta p^2)$ },
112     Method -> {Automatic, "SymbolicProcessing" -> 0}]/i + (i - 1)*
113     Log[1 +
114       Exp[ $\gamma B$  -  $\beta*(\Delta D^2 + \Delta b^2)$ ]]/i -  $\gamma \theta$ /
115       i -  $\beta*((2 i +$ 
116         4) ( $\Delta D^2 + \Delta p^2$ ) + \
117        $\Delta D^2$ )/i;
118
119
120
121
122 (** Full ln F: Realistic energies **)

```

```

123 sFFT0[sN_, β_, i_, ED_, Eph_,
124   Eb_, γN_, γn_, γB_, γθ_] :=
125   Log[NIntegrate[
126     Exp[zε (2 + i)]*(1 +
127       Exp[zε + γB - β*Eph])^(-i)*(1 +
128         Exp[zε/2])^(i + 1)/(1 +
129         Exp[zε + γn - β*(ED +
130           Eph))], {zε, -Infinity,
131     sN + γN + 2 β*Eph},
132     Method -> {Automatic, "SymbolicProcessing" -> 0}]]/i + (i - 1)*
133   Log[1 + Exp[γB - β*Eb]]/i - γθ/
134   i - β*((2 i + 4) Eph + ED)/i;
135
136 (** Full ln F: Realistic energies , realistic coefficients **)
137 sFFT1[sN_, β_, i_, ED_, Eph_,
138   Eb_, γN_, γn_, γB_, γ0_] :=
139   Log[NIntegrate[
140     Exp[zε (2 + i)]*(1 +
141
142       Exp[zε + γB - β*Eph])^(-i)*(1 +
143         Exp[zε/2])^(i + 1)/(1 +
144         Exp[zε + γn - β*(ED +
145           Eph))], {zε, -Infinity,
146     sN + γN + 2 β*Eph},
147     Method -> {Automatic, "SymbolicProcessing" -> 0}]]/i + (i - 1)*
148   Log[1 + Exp[γB - β*Eb]]/i
149   - β*((2 i + 4) Eph + ED)/i - ((i + 1)*γN

```

```

150     + (i - 1)*γB - γn + γ0)/i;
151
152 (** Full in N: Realistic energies **)
153 sNF[sF0_, β_, i_, ED_, Eph_,
154     Eb_, γN_, γn_, γB_, γ0_] := sN0 /. FindRoot[
155     Log[NIntegrate[
156         Exp[zε (2 + i)]*(1 +
157         Exp[zε + γB - β*Eph])^(-i)*(1 +
158         Exp[zε/2])^(i + 1)/(1 +
159         Exp[zε + γn - β*(ED +
160         Eph))], {zε, -Infinity,
161         sN0 + γN + 2 β*Eph}],
162     Method -> {Automatic, "SymbolicProcessing" -> 0}]]/
163     i + (i - 1)*
164     Log[1 + Exp[γB - β*Eb]]/i - β*((2 i + 4) Eph + ED)/i
165     - ((i + 1)*γN + (i - 1)*γB - γn + γ0)/i == sF0, {sN0, 0}]

```

Fit Analysis

Sample fitting routine with dataset `wrkW` and initial conditions `A1`.

```
1 A2 = Quiet [  
2   FindFit [  
3     wrkW  
4     ,  
5     sFA0[sN,  $\beta$ , wrkW[[1, 2]], wrkW[[9, 2]], wrkW[[16, 2]],  
6     wrkW[[24, 2]],  
7     Round[i],  $\Delta D$ ,  $\Delta p$ ,  $\gamma N$ , \  
8      $\lambda n$ ,  $\lambda B$ ,  $\lambda 1$ ,  $\lambda 2$ ,  $\lambda 3$ ,  $\lambda 4$ ]  
9     ,  
10    {{ $\Delta D$ ,  $\Delta D$  /.  
11     A1}, { $\Delta p$ ,  $\Delta p$  /.  
12     A1}, { $\gamma N$ ,  $\gamma N$  /. A1}, { $\lambda n$ ,  $\lambda n$  /.  
13     A1}, { $\lambda B$ ,  $\lambda B$  /.  
14     A1}, { $\lambda 1$ ,  $\lambda 1$  /.  
15     A1}, { $\lambda 2$ ,  $\lambda 2$  /.  
16     A1}, { $\lambda 3$ ,  $\lambda 3$  /.  
17     A1}, { $\lambda 4$ ,  $\lambda 4$  /. A1}}  
18    ,  
19    {sN,  $\beta$ }  
20    ,  
21    MaxIterations -> 10000  
22    ,  
23    Method -> {NMinimize,  
24    Method -> {"SimulatedAnnealing", "PerturbationScale" -> 4,
```

```
25     "LevelIterations" -> 1000}}
26   ]
27 ];
```

Appendix B: VASP Code

All molecule, supercell, and LDOS visualizations for Chapter 3 were rendered with VESTA [82]. Key auxiliary *VASP* files required for DFT calculations are presented here.

INCAR (Calculation Parameters)

In *VASP*, `INCAR` controls most parameters of the DFT calculation. Values should be tweaked as needed; an additional architecture-dependent batch script may be required for your particular implementation of *VASP*.

```
1 ISTART = 1          # Start job from past configuration
2 PREC   = High       # High precision
3 ENCUT  = 600.00     # Energy cutoff used in all calculations
4 LREAL  = .FALSE.    # Real space projection no
5 NELMIN = 6          # Minimum electronic steps
6 EDIFF  = 1e-4       # Allowed error in total energy
7 NPAR   = 4          # Number of cores (depends on local machine)
8 SYMPREC = 1E-8      # Similarity criterion
9 ADDGRID = .TRUE.    # Adds secondary grid for sensitive calculations
10 #### RELAXATION (uncomment code for relaxation run)
11 ISMEAR = -5         # Bloch smearing
```

```

12 #SIGMA    = 0.20          # Small sigma
13 #EDIFFG   = -1e-2        # Max allowed force
14 #NSW      = 10           # Ionic steps
15 #IBRION    = 1           # Relaxation method
16 #ISIF     = 2           # Relax ions , but no cell shape or size
17 #POTIM    = 0.2         # Step size
18 ##### OTHER PARAMETERS
19 IDIPOL    = 3           # Normal vector polarization (surface)
20 LDIPOL    = .TRUE.      # Dipole corrections
21 ##### KEEP DFT FILES
22 LCHARG    = .TRUE.      # Charge file
23 LWAVE     = .TRUE.      # Wave function file
24 ##### POTENTIAL optB86b (vdW potential dependent)
25 GGA       = MK
26 PARAM1    = 0.1234
27 PARAM2    = 1.0000
28 LUSEVDW   = .TRUE.
29 AGGAC     = 0.0000
30 # CENTER OF MASS      (required for dipole corrections)
31 DIPOL     = 0.333333333333 0.333333333333 0.899732919319

```

POSCAR (Atom Locations)

In *VASP*, POSCAR contains the initial positions of the system: this file is sensitive to line numbering. This sample POSCAR models a (2×2) cell without CF₃Cl molecules.

```
1 2v2 cell          # System name
2 2.47081554790000 # General lattice constant (lattice vectors)
3 1.732050807599999 1.0000000000000000 0.0000000000000000
4 1.732050807599999 -1.0000000000000000 0.0000000000000000
5 0.0000000000000000 0.0000000000000000 -8.4992180081999997
6 C      # Atomic species
7 8      # Number of atoms
8 Direct # Fractional position coordinates for atoms
9 0.0000000000000000 0.0000000000000000 0.9998741832348941
10 0.9999961792121184 0.5000144254076133 0.9999547779783455
11 0.4999893953802754 0.9999961792121184 0.9999547779783455
12 0.5000144254076133 0.4999893953802754 0.9999547779783455
13 0.1666772713197346 0.1666522412923896 0.9999547779783455
14 0.1666522412923896 0.6666704874878846 0.9999547779783455
15 0.6666704874878846 0.1666772713197346 0.9999547779783455
16 0.6666666667000030 0.6666666667000030 0.9998741832348941
```

KPOINTS (Grid Points)

In *VASP*, KPOINTS contains the k -point mesh for the calculation: this file is sensitive to line numbering. This sample KPOINTS automatically generates a $17 \times 17 \times 1$ k -point mesh at the reciprocal origin. While running, *VASP* may fine tune the mesh if necessary.

```
1 Automatic mesh
2 0           # Automatic generation scheme
3 G           # Generate a G (origin) centered grid
4 17 17 1     # k-Point Mesh
5 0. 0. 0.    # Offset (in reciprocal space) for mesh
```

Bibliography

- [1] A. Pimpinelli et al., Surf. Sci. **295**, 143-153 (1993).
- [2] J. Tersoff, A. W. Denier van der Gon, and R. M. Tromp, Phys. Rev. Lett. **72**, 266 (1994).
- [3] Z. Ni et al., ACS Nano **2**, 2301-2305 (2008).
- [4] B. Verberck, B. Partoens, F. M. Peeters, and B. Trauzettel, Phys. Rev. B **85**, 125403 (2012).
- [5] T. A. Witten and L. M. Sander, Phys. Rev. B **27**, 5686 (1983).
- [6] L. Sander, Contemporary Physics **41**, 203-218 (2000).
- [7] S. Stoyanov and D. Kaschiev, Curr. Top. Mat. Sci. **7**, 69 (1981).
- [8] J. A. Venables, G. D. Spiller, and M. Hanbücken, Rept. Prog. Phys. **47**, 399 (1984).
- [9] A. Pimpinelli, P. Jensen, H. Larralde, and P. Peyla, in *Morphological Organizations in Epitaxial Growth and Removal*, Z. Zhang and M. Lagally, eds. (World Scientific, Singapore, 1998) pp. 121ff.
- [10] A. Pimpinelli and J. Villain, *Physics of Crystal Growth* (Cambridge University Press, Cambridge, 1998).
- [11] B. Mutaftschiev, *The Atomistic Nature of Crystal Growth* (Springer, Berlin, 2001).
- [12] K. Oura, V. G. Lifshits, A. A. Saranin, A. V. Zotov, and M. Katayama, *Surface Science: An Introduction* (Springer: Berlin, 2003).
- [13] H. Brune, Surf. Sci. Rept. **31**, 121 (1998).
- [14] J. W. Evans, P. A. Thiel, and M. C. Bartelt, Surf. Sci. Rept. **61**, 1 (2006).

- [15] J. R. Morales-Cifuentes, T. L. Einstein, and A. Pimpinelli, *Phys. Rev. Lett.* **113**, 246101 (2014).
- [16] Angus I. Kingon, Jon-Paul Maria, and S. K. Streiffer, *Nature* **406**, 1032-1038 (2000).
- [17] R. W. Keyes, “Fundamental limits of silicon technology”, *Proceedings of the IEEE* **89**, 227-239 (2001).
- [18] S. E. Thompson and S. Parthasarathy, *Materials Today* **9**, 20-25 (2006).
- [19] John M. Shalf and Robert Leland, “Computing beyond Moore’s Law”, *Computer* **48** (12), 14-23 (2015).
- [20] S. Borkar, “Electronics Beyond Nano-scale CMOS”, *Design Automation Conference 2006*, July 24-28, San Francisco, California 2006.
- [21] K. S. Novoselov, A. K. Geim, S. V. Morozov, D. Jiang, Y. Zhang, S. V. Dubonos, I. V. Grigorieva, and A. A. Firsov, *Science* **306**, 666 (2004).
- [22] K. Kim et al., *Nature* **457**, 706-710 (2009).
- [23] C. Berger et al., *Science* **312**, 1191-1196, (2006).
- [24] F. Schwierz, *Nature Nanotechnology* **5**, 487-496 (2010).
- [25] M. Han, B. Özyilmaz, et al., *Phys. Rev. Lett.* **98**, 206805 (2007).
- [26] T. Ohta, A. Bostwick, T. Seyller, et al., *Science* **313**, 951-954 (2006).
- [27] Y. Zhang et al., *Nature* **459**, 820-823 (2009).
- [28] S. Y. Zhou et al., *Nature Materials* **6**, 770-775 (2007).
- [29] E. Rotenberg et al., *Nature Materials* **7**, 258-259 (2008).
- [30] P. Kisliuk, *J. Phys. Chem. Solids* **3**, 95 (1957).
- [31] J. Harris, and B. Kasemo, *Surf. Sci.* **105**, L281 (1981).
- [32] J. C. Tully, *Acc. Chem. Res.* **14**, 188 (1981).
- [33] J. V. Barth, T. Zambelli, J. Wintterlin, and G. Ertl, *Chem. Phys. Lett.* **270**, 152 (1997).
- [34] J. V. Barth, *Surf. Sci. Rept.* **40**, 75 (2000).
- [35] D. Z. Gao, M. B. Watkins, and A. L. Shluger, *J. Phys. Chem. C* **116**, 14471 (2012).
- [36] H. Brune, J. Wintterlin, J. Trost, G. Ertl, J. Wiechers, and R. J. Behm, *J. Chem. Phys.* **99**, 2128 (1993).

- [37] E. V. Albano and V. D. Pereyra, *J. Chem. Phys.* **98**, 10044 (1993).
- [38] V. D. Pereyra, E. V. Albano, and E. Duering, *Phys. Rev. E* **48**, 3229(R) (1993).
- [39] A. Pimpinelli, and T. L. Einstein, *Phys. Rev. Lett.* **99**, 226102, 1-5 (2007).
- [40] A. Winkler, in *Encyclopedia of Interfacial Chemistry: Surface Science and Electrochemistry*, K. Wandelt, ed. (Elsevier, 2018) pp. 195-215.
- [41] A. Winkler, *Surf. Sci.* **652**, 367-377 (2016).
- [42] A. Winkler and L. Tumbek, *J. Phys. Chem. Lett.* **4**, 4080 (2013).
- [43] D. Walton, *J. Chem. Phys.* **37**, 2182 (1962).
- [44] W. K. Burton, N. Cabrera, and F. C. Frank, *Phil. Trans. Roy. Soc. A* **243**, 299 (1951).
- [45] J. Villain, A. Pimpinelli, and D. E. Wolf, *Comments Cond. Mat. Phys.* **16**, 1 (1992).
- [46] M. Einax, W. Dieterich, and P. Maass, *Rev. Mod. Phys.* **85**, 921 (2013).
- [47] A. Pimpinelli, L. Tumbek, and A. Winkler, *J. Phys. Chem. Lett.* **5**, 995 (2014).
- [48] D. Kandel, *Phys. Rev. Lett.* **78**, 499 (1997).
- [49] J. A. Venables and H. Brune, *Phys. Rev. B* **66**, 195404, (2002).
- [50] J. M. Gottfried, Ph.D. Dissertation, Freie Universität, Berlin, 2004.
- [51] A. V. Matetskiy, L. V. Bondarenko, D. V. Gruznev, A. V. Zotov, A. A. Saranin, and M. C. Tringides, *J. Phys.: Condens. Matter* **25**, 395006 (2013).
- [52] P. H. Holloway and J. B. Hudson, *Surf. Sci.* **43**, 141 (1974).
- [53] M. A. Lazaga, D. T. Wickham, D. H. Parker, G. N. Kastanas, and B. E. Koel, *ACS Symp. Ser.* **523**, 90 (1993).
- [54] B. K. Min, A. R. Alemozafar, D. Pinnaduwege, X. Deng, and C. M. Friend, *J. Phys. Chem. B* **110**, 19833 (2006).
- [55] T. Potocar et al., *Phys. Rev. B* **83**, 075423 (2011).
- [56] J. Yang et al., *J. Phys. Chem. B* **112**, 7816-7820 (2008).
- [57] L. Tumbek and A. Winkler, *Surf. Sci.* **606**, L55 (2012).
- [58] P. R. Wallace, *Phys. Rev.* **71**, 622 (1947).
- [59] J. N. Fuchs, M. O. Goerbig, and M. Potemski, *Des électrons sans masse dans une feuille de carbone*, *Images de la Physique (CNRS)*, pages 50-56 (2007).

- [60] G. Giovannetti et al., Phys. Rev. B **76**, 073103 (2007).
- [61] Z. Liu, Nature Nanotechnology **8**, 119124 (2013).
- [62] J. R. Morales-Cifuentes and T.L. Einstein, A theoretical study of symmetry-breaking organic overlayers on single- and bi-layer graphene, Bull. Am. Phys. Soc. March 2013 Meeting
- [63] Y. Wang et al., Appl. Phys. Lett. **103**, 201606 (2013).
- [64] L. Cocco et al., Physical Review B **81**, 241412 R (2010).
- [65] S. Parker and S. Deledda, J. Phys. Chem. C **116**, 25206-25212 (2012).
- [66] Texas Advanced Computing Center, The University of Texas at Austin, www.tacc.utexas.edu/.
- [67] S. K. Saha et al., Phys. Rev. B **80**, 155414 (2009).
- [68] K. Berland, T. L. Einstein, and P. Hyldgaard, Phys. Rev. B **85**, 035427 (2012).
- [69] J. Klimeš, D. R. Bowler, and A. Michaelides, Phys. Rev. B **83**, 195131 (2011).
- [70] M. Dion, H. Rydberg, E. Schröder, D. C. Langreth, and B. I. Lundqvist, Phys. Rev. Lett. **92**, 246401 (2004).
- [71] G. Román-Pérez and J. M. Soler, Phys. Rev. Lett. **103**, 096102 (2009).
- [72] J. Klimeš, D. R. Bowler, and A. Michaelides, J. Phys.: Cond. Matt. **22**, 022201 (2010).
- [73] K. Lee, E. D. Murray, L. Kong, B. I. Lundqvist, and D. C. Langreth, Phys. Rev. B **82**, 081101 (2010).
- [74] J. Klimeš and A. Michaelides, J. Chem. Phys. **137**, 120901 (2012).
- [75] K. Berland et al., Rep. Prog. Phys. **78**, 066501 (2015).
- [76] Ikutaro Hamada and Minoru Otani, Phys. Rev. B **82**, 153412 (2010).
- [77] Ikutaro Hamada, Phys. Rev. B **89**, 121103(R) (2014).
- [78] Ikutaro Hamada, Phys. Rev. B **91**, 119902 (2015).
- [79] K. Berland et al., J. Chem. Phys. **146**, 234106 (2017).
- [80] Y. Jiao et al., J. Chem. Phys. **148**, 194115 (2018).
- [81] Few-layer and symmetry-breaking effects on the electrical properties of ordered CClF₃ phases on graphene. Josue R. Morales-Cifuentes, Yilin Wang, Janice Reutt-Robey, T.L. Einstein, Physical Electronics Conference 2014

- [82] K. Momma and F. Izumi, “VESTA 3 for three-dimensional visualization of crystal, volumetric and morphology data,” *J. Appl. Crystallogr.* **44**, 1272-1276 (2011).